Dissertation
zur Erlangung der Doktorwürde
an der

Gesamtfakultät für Mathematik,
Ingenieur- und Naturwissenschaften
der
Ruprecht-Karls-Universität Heidelberg

UNIVERSITÄT
HEIDELBERG
ZUKUNFT
SEIT 1386

MAX PLANCK INSTITUTE
FOR MEDICAL RESEARCH

Thema:

Biocompatible active microcarriers

vorgelegt von

Florian Ralf Peter

December 11, 2024

Gutachter:
Professor Dr. Peer Fischer
Professor Dr. Christine Selhuber-Unkel

Contents

Abstract

Modern medicine is on the verge of evolving from traditional methods based on the systemic administration of chemical drugs, radiation therapies, and invasive surgeries towards a new era of more sophisticated, targeted approaches. The emergence of new technologies and deeper comprehension of biological mechanisms allowed scientists to engineer more targeted treatment options that better address the fundamental causes of diseases. The potential of active micro- and nanomachines lies in their ability to perform tasks or deliver therapeutics at the same length scale as biological machinery. However, very few new treatment options have been approved and integrated into standard medical practices. A significant concern is that synthetic nano- and microstructures do not meet the necessary biosafety standards, primarily due to their frequent reliance on inorganic, toxic materials. A lack of long-term toxicology studies is even preventing the implementation of biocompatible designs, because there are no effective retrieval strategies available.

The first part of this thesis investigates how biological building blocks can be re-imagined to function outside of their typical purpose and environment, thereby attaining novel functionalities. DNA nanotechnology was employed to program unreactive DNA strands to self-assemble into a larger structure. The combination of a DNA scaffold with catalytically active platinum nanoparticles has enabled the successful fabrication of a unique active hybrid nanostructure. This combination of such fundamentally different materials was demonstrated to be stable and active in a high-energy fuel, which presents a multitude of potential applications, including the fabrication of chemical motors and larger functional machinery.

In the context of biological applications, the use of magnetic helical microswimmers for the transportation of medicines over longer distances within biological environments is regarded as the most promising approach. By replacing the conventional materials typically used to construct such structures, the author has fabricated an almost entirely biodegradable variant composed of magnesium and zinc. This directly addresses the biosafety concerns associated with the use of microcarriers in biomedical applications, thereby circumventing the need for a retrieval strategy. The demonstrated transport capabilities and adjustable degradation behaviour provide an actively guided transportation platform that can release therapeutics over time. The presented research represents a notable advancement over existing active microswimmers, particularly in the context of targeted drug or gene delivery.

The eye and its associated diseases were investigated as a potential target organ for the implementation of such active, degradable microcarriers. The current limitations of retinal therapy were surveyed and addressed using active microswimmers to identify solutions that are not available with conventional methods. The degradation of biological barriers with enzymes or the condensation of DNA into extremely small nanoparticles were demonstrated as promising research directions, both of which can potentially be combined with and benefit from targeted delivery through active microswimmers.

The work shown in this thesis therefor helps bridge the technological gap between the envisioned applications for active microcarriers and the state of the art.

Zusammenfassung

Die moderne Medizin steht kurz davor, sich von traditionellen Methoden, die auf der systemischen Verabreichung chemischer Medikamente, Strahlentherapien und invasiven Operationen basieren, zu einem neuen Zeitalter fortschrittlicherer, gezielterer Ansätze zu entwickeln. Das Aufkommen neuer Technologien und ein tieferes Verständnis biologischer Mechanismen ermöglichten es Wissenschaftlern, gezieltere Behandlungsmöglichkeiten zu entwickeln, die die grundlegenden Ursachen von Krankheiten besser angehen. Das Potenzial aktiver Mikro- und Nanomaschinen liegt in ihrer Fähigkeit in derselben Größenordnung wie biologische Maschinen zu agieren, Aufgaben auszuführen oder Therapeutika zu befördern. Allerdings wurden bisher nur sehr wenige neu Behandlungsoptionen zugelassen und in die medizinische Praxis integriert. Ein großes Problem besteht darin, dass synthetische Nano- und Mikrostrukturen nicht die erforderlichen biologischen Sicherheitsstandards erfüllen, was hauptsächlich auf die notwendige Verwendung von anorganischen, giftigen Materialien zurückzuführen ist. Das Fehlen langfristiger toxikologischer Studien verhindert sogar die Umsetzung biokompatibler Konzepte, da keine effektiven Rückgewinnungsstrategien verfügbar sind.

Im ersten Teil dieser Arbeit wird untersucht, wie biologische Bausteine neu konzipiert werden können, um außerhalb ihres typischen Zwecks und ihrer typischen Umgebung zu funktionieren und so neue Funktionalitäten zu erreichen. DNA-Nanotechnologie wurde verwendet, um unreaktive DNA-Stränge so zu programmieren, dass sie sich selbst zu einer größeren Struktur zusammensetzen. Die Kombination eines DNA-Gerüsts mit katalytisch aktiven Platin-Nanopartikeln ermöglichte die erfolgreiche Herstellung einer einzigartigen aktiven hybriden Nanostruktur. Diese Kombination von so grundlegend unterschiedlichen Materialien hat sich in einem energiereichen Brennstoff als stabil und aktiv erwiesen, was eine Vielzahl von potenziellen Anwendungen ermöglicht, darunter die Herstellung chemischer Motoren und größerer funktioneller Maschinen.

Im Zusammenhang mit biologischen Anwendungen gilt die Verwendung von magnetischen helikalen Mikroschwimmern für den Transport von Medikamenten über längere Strecken in biologischen Umgebungen als der vielversprechendste Ansatz. Durch den Er-

satz der herkömmlichen Materialien, die normalerweise für den Bau solcher Strukturen verwendet werden, hat der Autor eine fast vollständig biologisch abbaubare Variante aus Magnesium und Zink hergestellt. Dies geht direkt auf die Bedenken hinsichtlich der biologischen Sicherheit ein, die mit der Verwendung von Mikro-Trägerpartikeln in biomedizinischen Anwendungen verbunden sind, und umgeht so die Notwendigkeit einer Rückholstrategie. Die nachgewiesenen Transportfähigkeiten und das anpassbare Abbauverhalten bieten eine aktiv gesteuerte Transportplattform, die im Laufe der Zeit Therapeutika freisetzen kann. Die vorgestellte Forschung stellt einen bemerkenswerten Fortschritt gegenüber bestehenden aktiven Mikroschwimmern dar, insbesondere im Zusammenhang mit der gezielten Wirkstoff- oder Gentherapie.

Das Auge und die damit verbundenen Krankheiten wurden als potenzielles Zielorgan für die Umsetzung solcher aktiven, abbaubaren Mikro-Trägerpartikel untersucht. Die derzeitigen Einschränkungen der Netzhauttherapie wurden untersucht und mit aktiven Mikroschwimmern angegangen, um Lösungen zu finden, die mit herkömmlichen Methoden nicht verfügbar sind. Der Abbau biologischer Barrieren mit Enzymen oder die Kondensation von DNA zu extrem kleinen Nanopartikeln wurden als vielversprechende Forschungsrichtungen aufgezeigt, die beide potenziell mit der gezielten Abgabe durch aktive Mikroschwimmer kombiniert werden können und davon profitieren.

Die in dieser Dissertation gezeigten Arbeiten tragen daher dazu bei, die technologische Lücke zwischen den geplanten Anwendungen für aktive Mikro-Trägerpartikel und dem Stand der Technik zu schließen.

1 Introduction

Movement and locomotion are essential aspects of life, whether the motivation is the search for food, orientation towards light, reproduction or avoidance of danger.[1] While active movement used to be a privilege of living beings, it is not longer restricted to them. The invention of motors has enabled us to transfer the ability of directed motion to inanimate objects. The translation of motors to small length scales, however, remains a challenge. Due to engineering constraints the implementation of a motor is hard to realize at the nano- and micrometer scale, where active motion often takes place in fluids and deviates greatly from the macroscopic techniques that we know from fish and other sea life. Because the fluid imposes additional constraints that require special motion strategies, only some motor concepts are practical. Additionally, Brownian fluctuations make directed movement increasingly harder to achieve, the smaller the swimmers' dimensions become. The attempt to construct a tiny submarine is hence not straightforward. However, the ability to achieve and control precise movement on the micro- and nanoscale is desirable. It gives us the ability to navigate and influence the biological world through direct interactions with biological building blocks. The most promising aspect is their manipulation for biomedical applications, for example by achieving targeted delivery of therapeutics. Other applications, such as environmental remediation or chemical synthesis, by overcoming diffusion-limited reactions, are also of interest. Now this is not a new concept, and synthetic realizations of active micro- and nanoswimmers have been demonstrated. Compared to biological machines though - driven by motor proteins - synthetic counterparts are mostly made from inorganic materials, which are often not compatible with biological components or environments.

Chemical motors are typically used to convert chemical fuel into directed motion. In contrast to active swimmers, motors do not have inherent steering capabilities and their rotational diffusion results in a loss of directionality. Biological motors mitigate this by constraining the movement directions to specific paths, like kinesin along microtubules[2] or myosin motors along actin filaments.[3] Chemotaxis - the movement in response to a chemical stimulus - is a basic strategy of bacteria or cells, where motion towards or away from a concentration gradient of *e.g.* food or toxins increases survival chances. The ability of an entity to create its own local concentration gradients, called self-diffusiophoresis[4], can be utilized to achieve active motion without the need for externally applied gradients. This principle has been shown to achieve constant active motion in synthetic motors, where concentration gradients are produced by asymmetric chemical reactivity on the surface, as long as fuel is available.[5–7] For example, catalytically active metals can be coated on one side of an otherwise non-reactive particle to create asymmetry. Another method is the partial shielding of a uniformly catalytic (metal) particle. Biological materials and building blocks however, are typically not stable in high-energy chemical fuels. In chapter 3, DNA nanotechnology is used to engineer the stability of DNA in a harsh chemical environment, as well as self-assemble loose DNA strands into a three dimensional structure with a pre-determined shape. The combination with catalytically active nanoparticles results in hybrid nanostructures and forms a flexible platform, where the DNA framework can be used to strategically utilize chemical motors and potentially build larger functional assemblies.

In areas where chemical fuels are not desirable or available alternative propulsion concepts are required. Inspired by the locomotion mechanism of *Escherichia coli* bacteria symmetry breaking is found in chirality. The rotation of chiral shapes on the microscale leads to a non-reciprocal motion that can lead to propulsion. In the case of *E. coli* long, flexible flagella are rotated by molecular motors, which causes them to assume a helical shape.[8] This enables the bacterial cell to swim forward. To change the swimming direction the cell must stop its motion by switching to a tumbling state, before resuming swimming. The reorientation is no deliberate choice to turn into a specific direction, but rather a probing process to find a direction that offers advantageous conditions. Hence, precise control over the swimming direction goes beyond the capabilities of bacteria and chemical motors and can be achieved in synthetic swimmers through magnetic fields, which allows them to perform more complex tasks. However, precise fabrication of magnetic chiral structures on the nano- and microscale is a challenging task and is limited in the choice of suitable materials. Very few techniques are available to build such designs and even less can produce larger quantities of them. In chapter 4, the selection of materials for the fabrication of magnetic helical swimmers is revisited with the goal of finding not only biocompatible, but (bio)degradable alternatives. This is a crucial step that addresses existing biosafety concerns for the use of microswimmers in biological and medical context.[9]

A promising field for the application of microswimmers with the goal of transporting therapeutic agents is the treatment of retinal diseases. The retina is located safely in the back of the eye and responsible for enabling eye sight. Due to its protected location it is not easily accessible to conventional treatment options, and the current state of the art is not satisfactory, even though hundreds of millions of people worldwide are affected. Retinal diseases can stem from genetic mutations (estimation of 5.5 million people in 2020)[10], age-related degeneration (projected 196 million in 2020; 288 million in 2040)[11], or are related to diabetes ($\approx$ 159 million in 2010).[12] They are the most common cause of childhood blindness[13] and the general prevalence is higher in developing countries, because treatment options are expensive, medical equipment is not available and highly trained personnel are scarce.[14] Technological advancements and simplified procedures are needed in order to provide treatment options to the global population. The lack of safe and easy delivery routes prevents the prophylactic use of therapeutics. Genetic targets are already identified and treatment options are potentially available, but can not be utilized. The lack of an efficient delivery and transfection mechanism is the bottleneck for retinal therapy.[15] In chapter 5, I attempt to utilize the unique advantages of magnetic helical microswimmers to address the various challenges faced in the field of retinal drug or gene delivery.

Published work

The work presented in this thesis has in part been published in

- Alarcón-Correa[†], M.; Kilwing[†], L.; **Peter**[†], F.; Liedl, T.; Fischer, P.; Platinum-DNA Origami Hybrid Structures in Concentrated Hydrogen Peroxide, *ChemPhys Chem* **2023**, *24*, e202300294.
- **Peter**, F.; Kadiri, V. M.; Goyal, R.; Hurst, J.; Schnichels, S.; Avital, A.; Sela, M.; Mora-Raimundo, P.; Schroeder, A.; Alarcón-Correa, M.; Fischer, P.; Degradable and Biocompatible Magnesium Zinc Structures for Nanomedicine: Magnetically Actuated Liposome Microcarriers with Tunable Release, *Advanced Functional Materials* **2024**, *24*, 32.

In addition the author has contributed to the following publications

- Barad, H.-N.; Alarcón-Correa, M.; Salinas, G.; Oren, E.; **Peter**, F.; Kuhn, A.; Fischer, P. Combinatorial growth of multinary nanostructured thin functional films, *Materials Today* **2021**, *50*, 89.
- Kadiri, V. M.; Günther, J.-P.; Kottapalli, S. N.; Goyal, R.; **Peter**, F.; Alarcón-Correa, M.; Son, K.; Barad, H.-N.; Börsch, M.; Fischer, P. Light- and magnetically actuated FePt microswimmers, *Eur. Phys. J. E* **2021**, *44*, 74.
- **Peter**, F.; Kästner, J. and Meisner, J.; Strong Tunneling in the Reactions of Muonium Atoms with Unsaturated Hydrocarbons, *submitted* **2024**

[†] These authors contributed equally to the work.

2 Theoretical background

This chapter provides theoretical background information for the work presented in subsequent chapters.

2.1 DNA origami

Some of the first artificial DNA constructs based on complimentary Watson-Crick base pairing were proposed by Nadrian 'Ned' Seeman in 1982.[16] The creation of precise 2D or 3D objects built out of single stranded viral DNA (typically M13mp18 bacteriophage ssDNA with 7249 bp), termed DNA origami, was later shown by Rothemund[17] and Douglas *et. al.*[18], respectively. The principle is based on the programmed hybridization of DNA bases[19] (adenine-thymine and guanine-cytosine) through hydrogen bonding. Guanine and cytosine form three hydrogen bonds, compared to only two for adenine and thymine, which together with base stacking makes their pairing more stable. The idea is to design strategically placed, single stranded DNA oligonucleotides with a typical length of 21-45 bp (called staple strands), where each end hybridizes with two different positions on the ssDNA backbone, effectively 'stapling' it together through energetically favorable interactions. The length of the staple strands depends on the nucleotide content and has a minimum to ensure a stable double strand, whose melting temperature is high enough to not unfold at the desired working temperature.[16] A relatively high concentration of 16 mM Mg^{2+} ions is needed for charge neutrality, which allows the close packing of negatively charged DNA strands. If there are nucleotide mismatches the hybridization is incomplete and hence less thermally stable. By increasing the temperature above the oligonucleotides' melting point, the hybridization can be reversed and the double strand denatures. The energy needed to melt double stranded DNA depends on the number and type of hybridized nucleotide pairs. In order to form more complex structures, more staple strands are needed. As a result, when mixing a ssDNA backbone with its designed staple strands and applying a specific heating program, the predefined structure self-assembles through reversible hybridization, until the energetic minimum is found. The program starts by melting all hybridized double DNA strands, followed by a very long and slow cooling period. In order to help with the complex design process, the caDNAno software[20] provides a user interface, 3D visualization and automated staple design.

2.2 Brownian motion

In a fluid or gas every molecule is in constant motion, due to thermal energy. Collisions of these solvent molecules with themselves and larger particles in the medium result in a transfer of their kinetic energies. Due to the statistical nature of the collisions particles get pushed around in what is mathematically described as a random walk. The associated root-mean-square displacement (MSD) relates the statistically covered distance of the particle, as a function of time[21]

$$\langle \Delta x^2 \rangle = 2nDt \tag{2.1}$$

for and n-dimensional system. The (self-)diffusion coefficient D of a larger particle, surrounded by much smaller solvent molecules, can be estimated by the Einstein-Smoluchowski-Sutherland[21–23] equation[24]

$$D = \frac{\mathrm{k_B} T}{\xi} \tag{2.2}$$

with the Boltzmann constant $\mathrm{k_B}$ and the absolute temperature T. The drag coefficient is ξ. For a spherical particle in the low Reynolds number regime (explained in the next chapter) Stokes's law provides an estimate of

$$\xi = 6\pi\eta R_{\mathrm{H}} \tag{2.3}$$

with the viscosity η and the Stokes radius R_{H}. For translational diffusion of a sphere this leads to the Stokes-Einstein-Sutherland equation:

$$D_{\mathrm{trans}} = \frac{\mathrm{k_B} T}{6\pi\eta R_{\mathrm{H}}} \tag{2.4}$$

Using the drag coefficient of a sphere towards rotation leads to the rotational diffusion coefficient:[25]

$$D_{\mathrm{rot}} = \frac{\mathrm{k_B} T}{8\pi\eta R_{\mathrm{H}}^3} \tag{2.5}$$

The rotational diffusion coefficient is proportional to R_{H}^{-3} and is therefore of increasing relevance for smaller particles. The reorientation time is given by the Stokes-Einstein-

Debye expression:[26]

$$\tau = \frac{4\pi\eta R_{\mathrm{H}}^3}{\mathrm{k_B}T} \tag{2.6}$$

For small particles this leads to a loss of directionality due to the particles' fast reorientation. Actively propelled particles therefore are quickly re-oriented due to their rotational diffusion, which makes it significantly harder to achieve directed motion for smaller and smaller swimmer dimensions.

2.3 Motion at low Reynolds numbers

In order to understand the differences and consequences of locomotion at small length scales we need to consider the fluid flows around objects in an incompressible Newtonian fluid, such as water. The simplified Navier-Stokes equation under conservation of momentum and mass describes this flow as:

$$\rho\frac{\partial\vec{u}}{\partial t} + \rho(\vec{u}\cdot\nabla)\vec{u} = -\nabla p + \eta\nabla^2\vec{u} + \vec{F} \tag{2.7}$$

with the density of the fluid ρ (constant), its mass flow velocity $\vec{u}$, time t, pressure p and dynamic viscosity η.[27] It contains from left to right, inertial forces, pressure forces, viscous forces and externally applied forces, such as gravity. The interplay of inertial and viscous forces acting on a fluid particle define its behaviour and are described by the Reynolds number Re:

$$\mathrm{Re} = \frac{\rho u L}{\eta} = \frac{\text{inertial forces}}{\text{viscous forces}} \tag{2.8}$$

where L is the characteristic length of the object.[28] For objects that typically swim at speeds of 1-10 body lengths per second the Reynolds number decreases drastically with size to the very low regime $\mathrm{Re} << 1$. As a consequence the inertial terms of equation 2.7 become so small that they can be neglected, yielding the Stokes equation in the absence of any external forces

$$-\nabla p + \eta\nabla^2\vec{u} = 0, \qquad \nabla\cdot\vec{u} = 0 \tag{2.9}$$

Stokes flows or low-Reynolds number flows are therefore only dependent on viscous forces and pressure forces. The independence of inertial forces leads to a time independence of the equation. In practical term this means that reciprocal motion (symmetrical forwards and backwards deformation) is independent of the movement speed and can thus not lead to net motion. This is know as the scallop theorem.

2.3.1 Self-diffusiophoretic motors

Chemical motors posses asymmetrical chemical reactivity on their surface, which can lead to active motion. They do not have a natural analogue. So called Janus-particles have two 'faces', named after the Roman god. A simple design is a sphere with two halves: an inert side and a catalytically active side. By providing the Janus-sphere with fuel it starts converting that fuel into product(s) on the active side. If the reaction rate is higher than the diffusion of the individual molecules away from the particle, this induces a local concentration change in products and fuel molecules.[29] The attractive or repulsive interactions of the molecules surrounding the particles' surface at the interface change as a result of the reaction. This can lead to a net flow of fluid from one side to the opposite side.[30] Since the fluid is incompressible the particle moves in the opposite direction, leading to its propulsion. Janus particles have been studied extensively by coating a polystyrene or SiO_2 bead on one side with Pt.[5–7,31] Pt is a known catalyst for the disproportionation reaction of hydrogen peroxide, which can be used as fuel for the Janus swimmer. Experimentally one can observe this self-diffusiophoretic behaviour for SiO_2/Pt Janus particles, which move towards the SiO_2 side, when exposed to hydrogen peroxide.

2.3.2 Magnetic propulsion

Some bacteria, like *E. coli* achieve propulsion at the microscale through rotating, flexible filaments, called flagella.[32] Constant rotation of the flagellum in one direction results in a helical shape, rendering its movement non-reciprocal. This has been the inspiration for the design and fabrication of helical microswimmers, which are explored in chapter 4. In the case of micropropellers that to some extent mimic the motion of bacteria, magnetic fields are used to induce the rotation. Typically a ferromagnetic part is therefore incorporated into the body of the swimmer to allow for magnetic manipulation. If the swimmer is placed inside an uniform, external magnetic field, its magnetic moment $\vec{m}$ gives rise to a torque

$$\vec{T} = \vec{m} \times \vec{B} = V\vec{M} \times \vec{B} \tag{2.10}$$

with the volume V and remnant magnetization $\vec{M}$ of the magnetic material.[33] If $\vec{B}$ rotates, then the swimmer starts to rotate until its $\vec{M}$ and the external $\vec{B}$ are parallel to each other and the torque becomes zero. In this way no linear force (pulling) is applied the swimmer. Spherical magnetic particles can be pulled using a magnetic field gradient, but the effect is short ranged and one dimensional. In contrast, a more elegant approach that allows for three dimensional propulsion is achieved for helical bodies and rotating magnetic fields, created for example by three orthogonally placed coil pairs. These can create a homogeneous, rotating magnetic field in a precisely controlled fashion by modulating the currents through the individual coil pairs. The swimmers' magnetic moment tries to follow the rotation of the external magnetic field. When the shape of the swimmer is asymmetric towards the rotation axis, its rotation will lead to translational movement and *vice versa*.[33] Typically a helical shape is used, which behaves like a corkscrew. In this way a helical shaped particle, magnetized orthogonal to its long axis, can be propelled and steered precisely in 3D.[34]

2.4 Glancing angle deposition

The fabrication of corkscrew shaped magnetic micro-and nanostructures can be achieved by specialized physical vapor deposition. A method, in which materials are evaporated from a source in a vacuum chamber. The evaporated material flux is reasonably parallel when it is incident on the substrate, due to the long distance (0.5 m) between source and substrate. The vapor flux is created by thermal evaporation. In this thesis electron beam (e-beam) evaporation from a tungsten filament gun was used. After exiting the anode the electrons are controlled by a sweep controller and directed onto the crucible holding the source material. The operating voltage applied to the gun was 8 kV. The vapor pressure of each deposition material is different and temperature dependent. In order to individually control the deposition rates the beam current is controlled to achieve the desired heating.

Upon contact with the substrate the adhered atoms, called adatoms, condense, start nucleation points and diffuse on the surface with a material- and temperature-dependent mobility. If the substrate is perpendicular to the direction of the vapor flux then over time a continuous thin film is deposited. However, if the substrate is tilted by and angle α the deposition geometry changes and the angle of incidence becomes oblique. For $\approx 85°$ nanostructuring is observed due to the shadow effect, which prevents uniform growth and results in distinct column formation. If in addition the substrate is rotated around its normal, by an angle φ, this specialized process is called glancing angle deposition (GLAD).[35] A typical GLAD system and its specialized deposition scheme is depicted in figure 2.1.

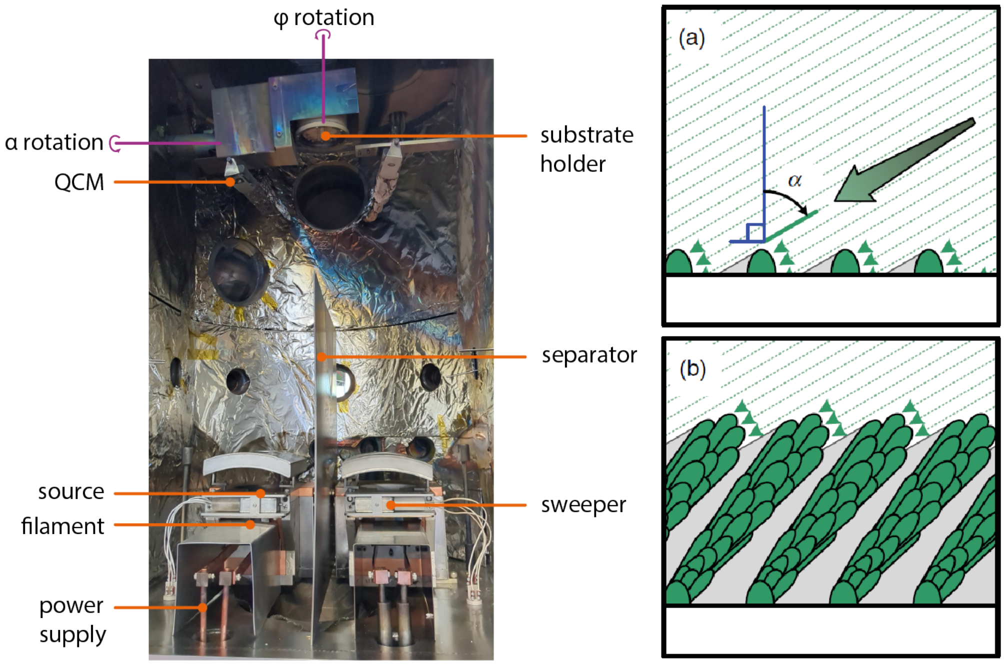

Figure 2.1: **Left**: GLAD system with a substrate holder mounted on a rotatable stage capable of both α and φ rotation in a vacuum chamber. The incoming vapor flux from a source material is measured via a quartz crystal microbalance (QCM), which is then used for feedback loop control over the substrate holder motion. **Right**: **(a)** By tilting the substrate to an incident angle α, patterned substrates create shadowed areas (grey). **(b)** No growth occurs in the shadowed areas, resulting in the creation of distinct columns that grow towards the vapour source. The figure on the right is adapted from[35].

This process produces columns that grow towards the vapour source. In order to create different shapes the substrate's tilt and rotation angles can be changed. A sudden change in φ results in the formation of zig-zag structures, while the slow and constant rotation in one direction creates helical columns.

Many materials, including metals, oxides, salts, semiconductors and polymers can in principle be deposited with physical vapor deposition. The implementation of multiple vapour sources allows for the co-deposition at specific atom ratios to create composite materials. There are several patterning methods used to create defined substrates prior to GLAD. Through the use of Langmuir-Blodgett deposition, monolayers of close-packed spherical nano- and microparticles can be created that allow for the growth of individual structures on top of each seed particle.

2.4.1 Quartz crystal microbalance

A quartz crystal microbalance close to the substrate holder measures the deposited material mass, which is used to control the deposition thickness. The deposition rate is monitored in real time via individual quartz crystal microbalances (QCMs) for each material source. The measurement of deposited material thickness is based on the piezoelectric properties of quartz crystals. This use of QCMs was pioneered by Günter Sauerbrey[36]. By applying an alternating voltage the crystal starts oscillating. Its resonance frequency depends on the cut of the crystal, temperature, mechanical influences and inversely on its thickness. Keeping the other parameters constant gives the resonance frequency f as a function of crystal thickness d[36]

$$f = \frac{v}{2d} \tag{2.11}$$

with the propagation velocity of the transversal wave v. As an approximation for adequately thin, rigid films the deposition of any material on the crystal can be treated as a thicker crystal of the same mass. This can be used to measure the thickness of films, deposited on the QCM:

$$d = \frac{m}{A \cdot \rho} \tag{2.12}$$

if the area A and density ρ of the deposited material are known.[36]

For practical purposes this means that the entire area A of the QCM must be exposed to the vapor flux and the density of the deposited material must be known to achieve accurate deposition rates. Furthermore, the gathered deposition rate information is part of a feedback loop that controls substrate motion in real time. In reality the correlation of rate constants to actual growth thickness is more complex. Due to geometric restrictions and the shape of the emitted vapor plume[37] the QCM and substrate holder do not experience the same vapor flux, which has to be corrected using the experimentally determined tooling factor F_0 for each deposition system. By tilting the substrate to an angle α, the mass influx on the substrate is reduced by a factor $\cos(\alpha)$, which reduces the deposited film thickness accordingly. Additionally the density of the deposited material film decreases with increasing α by a factor of $\rho_\mathrm{n}(\alpha)$, which is the normalized density compared to the bulk material density ρ_b, assumed by the QCM. A simple model used to estimate the angle dependence of the deposited film density for deposition on hemispherical features is[35,38,39]

$$\rho_\mathrm{n}(\alpha) = \frac{2\cos\alpha}{1 + \cos\alpha} \tag{2.13}$$

The deposition ratio R_0 combines all these effects and is defined as the ratio between real deposition thickness t_s and nominal deposition thickness t_QCM.[35]

$$D_0 = \frac{t_\mathrm{s}}{t_\mathrm{QCM}} = \frac{F_0 \cos\alpha}{\rho_\mathrm{n}(\alpha)} \tag{2.14}$$

R_0 is shown in figure 2.2 for SiO_2 of an exemplary system. F_0 can be determined experimentally by performing several depositions at $\alpha = 0$ and fitting the measured thicknesses to equation 2.14.

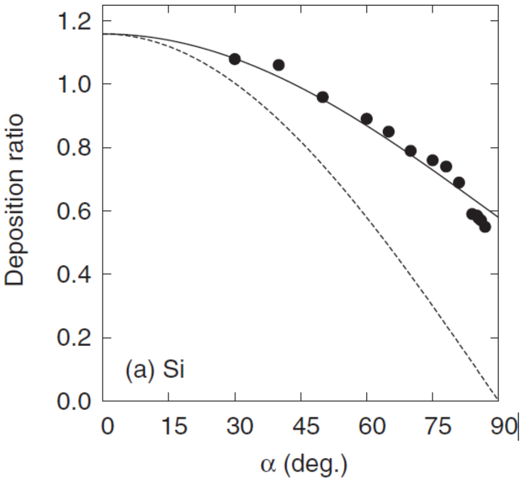

Figure 2.2: Deposition ratio dependence on the tilt angle α for SiO_2 with (solid line) and without (dashed line) incorporation of a basic density model to account for density reduction. The data points represent experimental values. Figure taken from[35].

2.5 Eye anatomy

Chapter 5 in this thesis concerns the use of magnetic micropropellers to move in the eye and retina. The eye is one of the most important and complex sensory organs of the human body. Directly connected to the brain it allows interaction with the outside world by collecting light and enabling sight. It is therefore called a window to the brain.[40] It possesses unique properties, such as easy accessibility, transparency and low immune activity, providing a somewhat isolated 'container', ideal for studying diseases and their potential therapies. In order to understand the challenges in treating eye diseases, a brief overview over the anatomy and natural barriers is provided. The most common eye diseases are related to damage to the retina (retinopathy). The most severe forms affect the central, high-resolution, color vision, achieved in the macula, such as (age-related) macular degeneration or (diabetic) macular edema (fluid deposits). Other forms lead to retina detachment, like in proliferative vitreoretinopathy, or are genetic, such as retinopathia pigmentosa. Other diseases are caused by an infection that leads to inflammation of the retina (retinitis), such as cytomegalovirus retinitis and endophthalmitis.[41] Diseases of the retina are potential targets for active drug delivery. However, several biological barriers complicate the transport.

The eye can be divided into two segments, the anterior and the posterior segment, as shown in figure 2.3. The anterior segment consists of the light capturing and focusing elements: cornea, conjunctiva, lens, iris and the aqueous humour. The cornea is the outermost, transparent tissue of the eye and consists of cell layers with tight junctions to protect the eye. Below is a thick layer of regularly arranged collagen fibers. The specific orientation ensures optical transparency. Together with the conjunctiva it forms a mechanical permeability barrier. However, when attempting a topical drug application, *e.g.* eye drops, tear drainage is responsible for removing up to 90 % of the applied dose, before the drug reaches deeper layers of the cornea.[42]

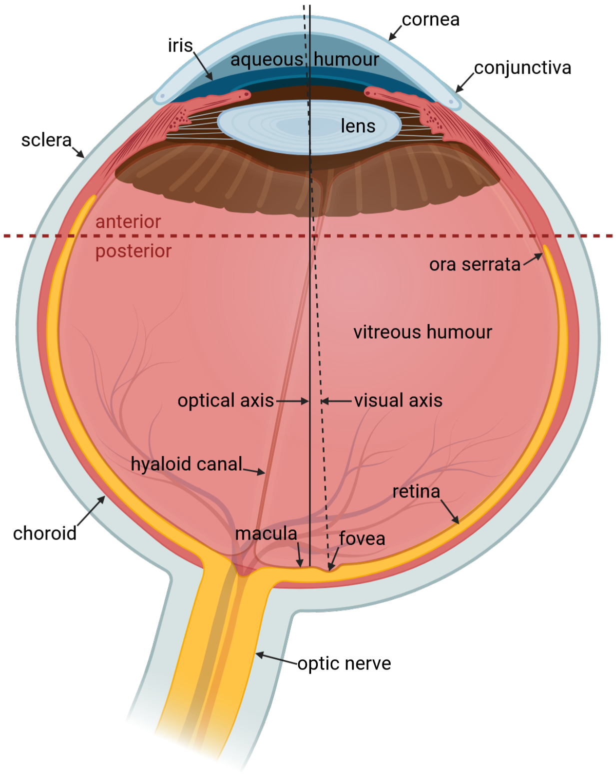

Figure 2.3: Schematic representation of the human eye. Created with BioRender.com

The posterior segment of the eye contains from the outside to inside: the sclera, choroid, retinal pigment epithelium, neural retina, and vitreous humour. The sclera is a sieve-like elastic tissue that wraps around the eye and fuses with the cornea. The sclera also consists of collagen fibers, but in an overlapping, disorderly fashion, which makes it appear white. It effectively shields the inside of the eye from stray light. It is thick, tough, highly lipophilic and impermeable to the diffusion of most drug molecules.[42–44] Only a combination of the right surface charge, size, hydrophilicity and physicochemical properties grants entry. Below the sclera lies the choroid, which contains the blood vessels responsible for supplying the neural retina with oxygen and nutrients.

The neural retina is multilayered and contains the sensory part of the eye. It coats the inside of the eye up until the *ora serrata*. The individual layers are shown in figure 2.4. Here the photons are captured by the photoreceptor cells and converted into an electrical signal. The signal is then transmitted inwards via bipolar cells and ganglion cells to the central nervous system. The nerve fiber layer makes up the innermost layer of the human neural retina.[42] The nerve fibers are collected and bundled together to form the optic nerve. The neural retina contains the most crucial parts of the eye and is the most interesting target for drug delivery. This sensitive part of the eye is well protected.

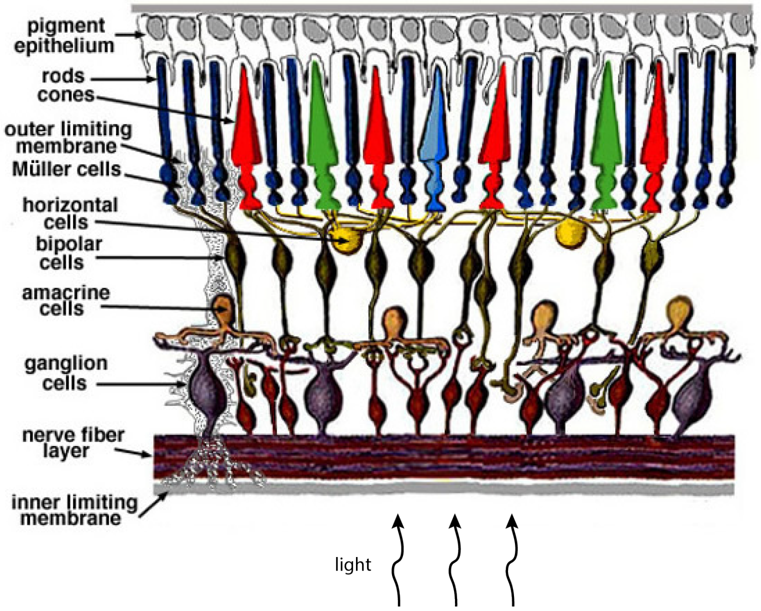

Figure 2.4: Schematic representation of the anatomy of the human neural retina. Adapted from[41].

Outwards the retina is closed off to the choroid by the retinal pigment epithelium (RPE) - a densely packed, smooth, single cell layer held together by tight junctions. Apart from its barrier function its pigments absorb scattered light to prevent radiation damage. Inwards the inner limiting membrane (ILM) forms a significant barrier to the vitreous humour. It forms the basement membrane of the Müller cells[45], made of a three-dimensional collagen IV fiber network, proteoglycans and laminins.[46,47] The thickness of the membrane increases with age from 70 nm in human fetuses to up to 4 µm in adults.[48]

The centre of the eye is filled up by the vitreous humour, a thick, gel-like fluid made of water, collagen, hyaluronic acid, and glycosans, which maintains the structure of the eye. The vitreous humour is attached to the anterior retinal layers, optic nerve disc, and the macula.

The most common drug delivery strategies rely on injecting the therapeutic either subretinally (between photoreceptor cells and retinal pigment epithelium) or intravitreally (into the vitreous).

2.5.1 Anatomical differences in human and pig eyes

While the closest anatomical relatives of humans are primates, the ethical burden of animal studies demand an alternative. For this reason *ex vivo* pig retinas have been investigated as a potential model system. Porcine eyes are a waste product of the meat industry and readily available. The pig eye anatomy has been studied and found to be very similar to human anatomy, making it an excellent intermediate step, before attempting clinical studies. A summary of the differences between human and the pig eye anatomy is given below.

Developmental studies found that pigs are matured at an age of 6 months and their retinas show very similar features found in adult humans.[49] Investigations into the eye size[50,51], aqueous humour outflow system[52], sclera thickness[53], ganglion cells[54,55] and photoreceptors[56] come to the same conclusion. Topographically the density of human photoreceptor cells varies significantly, with the highest concentration in the circular macula. A similar yet band-like feature is found in pigs.[51,57] More differences can be found in the location and organisation of blood vessels within the retinal layers.[58] The pigs eye' vasculature is located superficially in the nerve fiber layer, while human blood vessels lie deeper.[59] The thickness of the pig's retina was measured to 160-220 µm in adult pigs[51,60], while the human retina ranges in thickness from 80 µm to 300 µm, depending on the location.[41]

Overall, the anatomy of the pig's eye is very close to human eyes, potentially better even than most primates[61], and serves as an excellent model system for targeted drug delivery.[50] Existing differences are not crucial for scope of this study.

After this overview of theoretical concepts, the following chapters discuss the experimental work.

3 Chemical DNA nanohybrid structures

In this chapter it is examined how one can realize catalytically active hybrid structures that may be of use in the context of chemical motors.

3.1 Introduction

The precise fabrication of nanoobjects is a challenging engineering task. A variety of fabrication techniques have been developed to achieve precise control over shape and chemical functionality. For chemical motors, symmetry breaking is essential to achieve active motion, as discussed in the theoretical section on low Reynolds numbers. Physical and chemical methods like vapor deposition, photochemistry, masking and lithography are capable of introducing a structural or functional asymmetry, but usually require clean, vacuum conditions and highly ordered substrates to work. Self assembly approaches work in bulk, produce large numbers and can be used to introduce asymmetry in solution, but the design of nanosized building blocks is often limited by the available fabrication technologies. An advantage is that the asymmetry can be designed beforehand and the fabrication then follows a predetermined assembly process.

The DNA origami technique is an example of utilizing biological molecules to build well-defined, three-dimensional, nanosized objects with specifically addressable anchor points.[16–18] The shape can be designed flexibly within the natural constraints of the DNA double helix and the DNA origami folding requirements. Since DNA is inert and relatively unreactive, a second, active component is needed to build a catalytically-active machine. The active part can for instance be provided by a nanoparticle.

3.2 Motivation

Actively performed tasks always require an energy source. In chemical synthesis, catalysis or propulsion applications, high energy fuels are desirable to drive a certain functionality. Chemical motors in the form of Janus-type swimmers utilize Pt due to its high reactivity to achieve self-phoretic motion via the disproportionation of hydrogen peroxide.[5] The creation of local concentration gradients can lead to fluid flows and particle movement due to the Janus shape.[30] Here, the combination of the inorganic Pt nanoparticles (PtNP) with DNA origami structures is investigated to explore possible ways to transfer catalytic functionality to an otherwise inert biological system.

3.3 Results

The results of this project have been largely published in:
Alarcón-Correa[†], M.; Kilwing[†], L.; **Peter**[†], F.; Liedl, T.; Fischer, P. *ChemPhysChem* **2023**, *24*
[†] These authors contributed equally to the published work.

MAC, LK, TL, and PF conceptualized this work. 6HB stability analysis was performed by LK. 6HB to Pt coupling protocol development was performed by FP and MAC. Pt-6HB activity and stability studies were performed by FP under supervision of MAC. In addition, unpublished results are presented on active propulsion tracking experiments, which were performed by FP.

3.3.1 DNA origami design and folding

In the first part of this project, DNA has been folded into an exemplary and well-known origami design, called the 6-helix bundle (6HB).[62] The base design was provided by Prof. Dr. Kerstin Göpfrich and is based on the M13 bacteriophage derived p8064 DNA scaffold with 8064 nucleotides.
The scaffold DNA was folded by the use of staple strands into six, honeycomb structured, roughly 400 nm long DNA double helix tubes in alternating orientation, shown in figure 3.1. The diameter measured by TEM was 8 nm. Staples were used at 10x excess (100 nM final concentration) towards the scaffold in origami buffer (1x TE buffer with 14 mM $MgCl_2$). The high concentration of Mg^{2+} ions is needed to neutralise the negative charges of the DNA backbone. Initial heating to 70 °C and incubation for 3 min dissolved any possibly entangled conformations of the DNA strands. The solution was cooled to 20 °C in steps of 0.1 °C per 90 s. From 50 °C the program directly shifted to 20 °C. This was followed by a 30 min incubation at 20 °C. Subsequently, the mixture was heated to 40 °C and incubated there for 4 h before it was cooled to 20 °C again where it incubated for another 2 h. The folding ramp ended after cooling the solution to 4 °C.

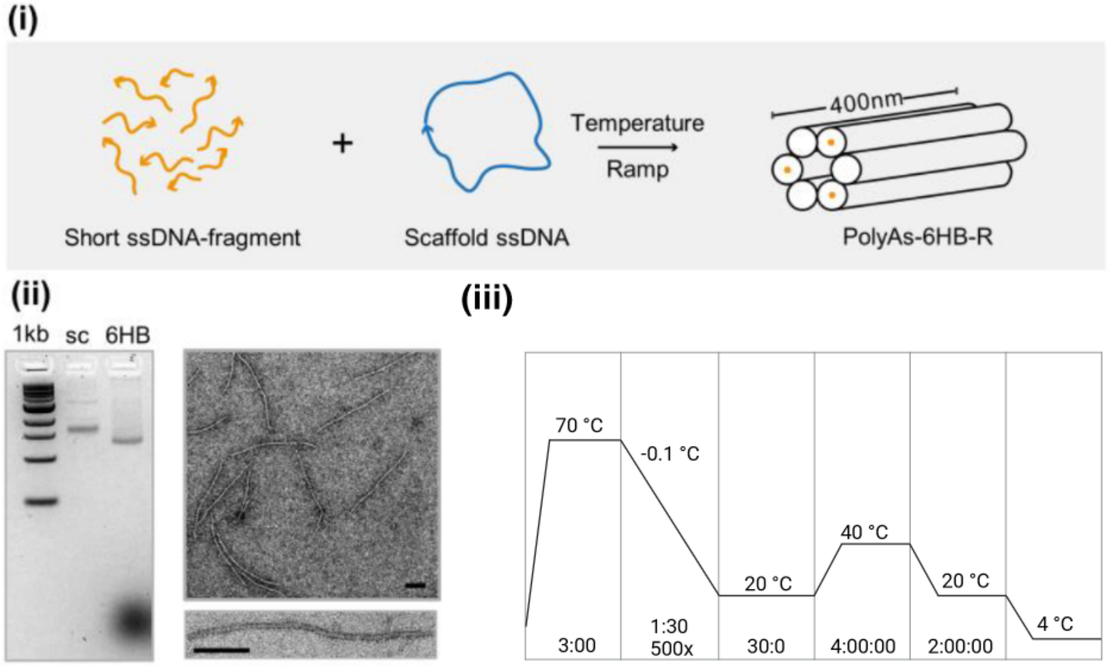

Figure 3.1: **(i)** Schematic overview of the folding process from DNA staple strands and scaffold DNA to a 6HB with two handles (PolyA and R). **(ii)** 2 % native agarose gel to verify the proper folding of the 6HB. TEM images of 6HB show the expected shape and size. Scale bars are 100 nm. **(iii)**Thermocycler program for the folding process. Figure adapted from[63].

The end of each helix was adapted to hold three overhanging staple strands, resulting in three attachment points on each end of the 6HB. A schematic of the handle design is shown in figure 3.2, the entire sequence of the 6HB can be found in the publication.[63] Each side of the 6HB has three of the same overhangs to allow site specific anchoring. On the O1-end the overhangs carry a sequence of A_{15} (polyA) used for easy coupling to a second component carrying a T_{15} (polyT) sequence in the next section. On the O2-end a deliberately non-self-compatible sequence AATATCTGTATGTCTA (R) was implemented to avoid unspecific binding or allow specific attachment of a potential third binding partner. From now on the PolyA-6HB-R construct is abbreviated as 6HB. The use of multiple handles per side should increase binding efficiency and strength.

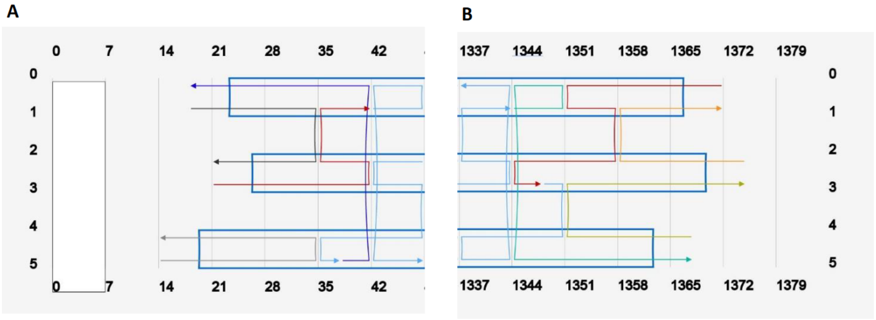

Figure 3.2: Excerpt from the cadnano viewer, showing the overhangs for each end of the 6HB. **A** O1-end of the 6HB, showing three handles at the 3' end with a polyA sequence. **B** O2-end of the 6HB with three overhangs with a random sequence at their 3' end. Full sequences are available in the publication. Figure taken from[63].

3.3.2 6HB stability in hydrogen peroxide

Potential hybrids of 6HB and Pt would require the DNA origami structure to survive in hydrogen peroxide solutions, a commonly used fuel for Pt in active systems. The literature offers no prior studies on the stability of DNA origami in this context. However, loose single- and double-stranded DNA is shown to be unstable in chemically reactive and harsh environments, like hydrogen peroxide. The oxidation of deoxyribose leads to base liberation, which eventually might lead to phosphate-backbone cleavage.[64–68] In order to test the stability of 6HBs we exposed the DNA origami (120 fmol) to hydrogen peroxide in concentrations of 1 and 5 %. The concentrations were chosen as they represent common working conditions for chemical Janus motors.[5,7] Samples were taken at different time intervals (30, 45, 60, 90 min, 2, 24, and 72 h) over a duration of three days and subsequently diluted to effectively stop further degradation effects of the hydrogen peroxide. Control samples are incubated in ultrapure water for 72 h. All collected samples were then subjected to 2 % native agarose gel electrophoresis, stained with SYBR Gold intercalating DNA dye. A damaged construct will deviate in its mobility, while an intact structure would be represented by a single, clean band in the gel. The process and results are shown in figure 3.3. The lanes for 6HB, exposed to the same concentration of hydrogen peroxide, are color coded and loaded from left to right by decreasing exposure time. The first three lanes are for reference: DNA ladder (1 kb), single-stranded scaffold DNA (sc), and untreated 6HB (raw). As we can see from the gel images the electrophoretic behaviour of 6HB is unaffected in all concentrations and exposure times, compared to the control sample (C^-). The low molecular weight of the different short staple strands provides higher mobility in the gel and results in a diffuse 'band' at the bottom of the gel.

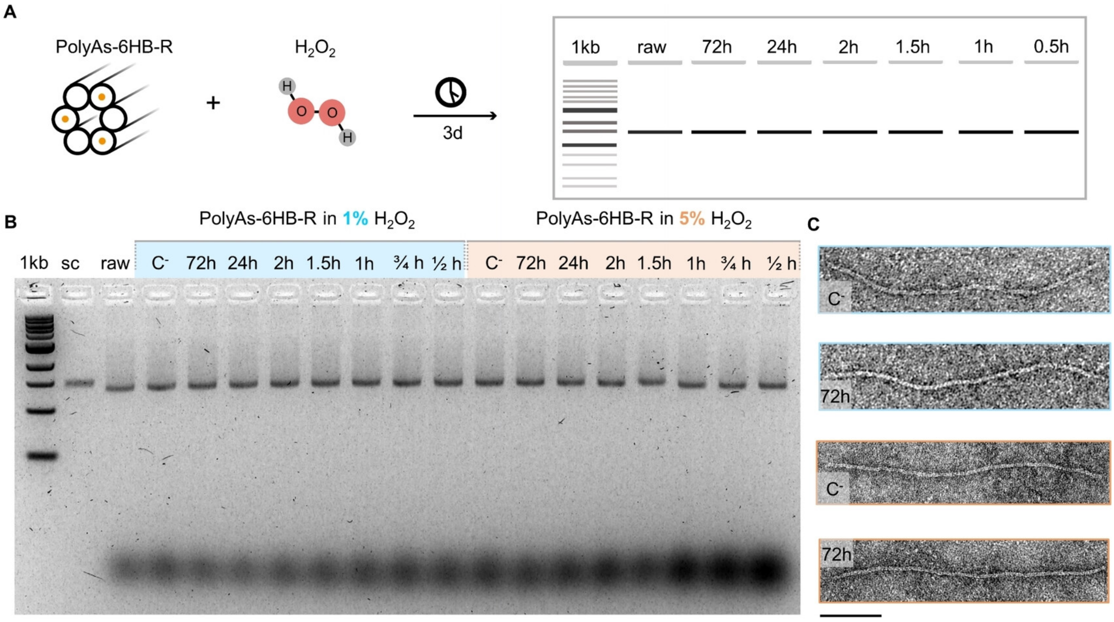

Figure 3.3: **A** The effect of 1 and 5 % of hydrogen peroxide on 6HB was investigated over the course of 3 days. Expected results are schematically shown. **B** Image of 2 % native agarose gel after staining with SYBR Gold. A control sample of single-stranded scaffold (sc) has a different mobility, while untreated (raw) 6HB show the same bands as 6HB treated with 1 and 5 % hydrogen peroxide over 3 days. **C** TEM images of 6HB before and after hydrogen peroxide treatment for 3 days. Concentrations are colour coded. Scale bars are 100 nm. Figure taken from[63].

Additionally, the structural integrity was investigated using TEM. For that, samples were applied in low concentration (10^7 particles per µl) to plasma charged, carbon-coated copper grids (positive, 45 s, 15 mA). After drying almost completely the remaining solution was removed with a filter paper to remove residual salts. The DNA was stained using 2 % uranyl formate as a contrast agent. Uranyl formate was preferred over uranyl acetate, as it provides smaller grain sizes and better contrast. The shorter shelf life was compensated for by storing frozen aliquots at -20 °C. TEM imaging was performed at reduced 80 kV acceleration voltage for this study to minimize e-beam damage, compromising on resolution. The micrographs showed no breaks, kinks or deformations.

The increased stability of DNA origami over loose DNA might be a results of the dense packing of DNA helices and counter-ions, achieved through the DNA origami folding process. The close packed conformation possibly even reduces free diffusion through the structures, limiting exposure of hydrogen peroxide to the outward facing areas. The liberation of single bases, as a result of deoxyribose oxidation, from scaffold DNA or staple strands reduce their respective melting temperature. It is likely that multiple base liberations would need to occur on the same strand to reverse the hybridization, eventually leading to the loss of a single staple strand. However, the stability of the DNA origami is unlikely to be affected severely by the loss of a single staple strand. The presence of multiple crossover staple strands in the design should retain overall structural stability. Similarly, the cleavage of the DNA backbone should have very little effect on the folded origami. Extensive staple strand loss and phosphate backbone cleavage will of course eventually lead to an unfolding process.

3.3.3 DNA origami to Pt coupling

After confirming the stability of DNA origami constructs in hydrogen peroxide the combination with catalytically active nanoparticles was pursued. The coupling of DNA to gold nanoparticles (AuNP) was known at the time and served as reference for initial coupling attempts. As discussed in the theory section, the formation of origami structures requires a high concentration of Mg^{2+} ions. This high ionic strength environment causes free Au or Pt nanoparticles to aggregate in solution, by reducing the electrostatic repulsion between similarly charged particles so that attractive Van-der-Waals interactions dominate and cause aggregation.[69] In order to improve colloidal stability particle surfaces can be decorated with ligands to keep them apart. We adapted a procedure from the literature[70], in which ssDNA strands with thiol functionalities were used to modify the particle surface. Thiols are shown to completely displace the originally attached citrate ligands through their high affinity for metals. While the nature of the bond is complex, X-ray photoelectron spectroscopy shows involvement of Au 4f and S 2p orbitals[71–73] Density functional theory calculations indicate that the binding energies are higher for Pt-S than those for Au-S bonds[74] through partial charge-transfer.[75] The functionalization of Pt with thiol ligands should therefore be possible. Dithiol-T_{19} (SH-PolyT) was purchased from Integrated DNA technologies. The use of dithiol-ssDNA linkers results in a more stable attachment through two Pt-S bonds.[76] Since thiols form disulfide bonds in solution they had to be reduced again by incubation with 2.6 mM Tris (2-carboxyethyl) phosphine (TCEP) for 30 min. Afterwards they were added to PtNP of 70 nm diameter in 2 mM sodium citrate buffer in $4 \cdot 10^5$-fold excess and incubated for 15 min, before freezing at -80 °C for 1 h. An internal protocol for the conjugation of AuNPs to thiol-ssDNA strands from the group of Prof. Dr. Tim Liedl was adopted. It was found that freezing the samples led to an at least 50 times faster functionalization compared to established literature procedures, where samples were shaken for a minimum of 2 days at 23 °C.[70] The idea was to slow down ssDNA motion to allow for longer contact time, which is shown to be crucial for Pt-S (or Au-S) bond formation and strength.[75] To remove the large excess of ssDNA the particles were washed ten times by centrifugation at 13000 rcf (relative centrifugal force) for 90 s and were transferred to the origami buffer during the last wash in preparation for the next step. The use of Protein LoBind tubes (Eppendorf) was crucial to avoid adherence to the tube walls during centrifugation. An overview of the procedure is given in figure 3.4A. The reference protocol for AuNP used 100 kDa centrifugal filters, which resulted in a complete loss of all PtNPs in the filter. If the coverage was successful the particles did not aggregate and precipitate. Storage at 4 °C ensured stability of the Pt-S bond for longer storage times.[77,78]

With the PtNPs stable under high salt conditions, which is needed for DNA origami stability, and decorated with PolyT strands, complementary to the 6HB-handle, the assembly of the Pt-6HB constructs followed. The literature protocol for AuNP adds 6HB and incubation in a rotary shaker for 24 h at 23 °C. Translation to PtNP-PolyT did not give the desired results, because the Pt particles adhered to the tube walls during the long shaking process. In order to optimize the hybridization process we transferred a mixture of 6HB and PtNP-PolyT to a PCR tube and used the thermocycler to ramp the temperature in five cycles between 25 and 28 °C, with a rate of 0.1 °C per second. The ceiling temperature was chosen specifically, as it is below the melting temperature for 19 T oligomers, but high enough to separate partially hybridized strands. By using this strategy the coupling of 6HB to PtNP was achieved in 5 minutes. Importantly, the handling from this point on has to be at temperatures below 28 °C.

The ratio of 6HB to PtNP had to be optimized to achieve a specific configuration. After some experimentation a ratio of 2:1 was found to be ideal to achieve the attachment of a single 6HB per PtNP in 60-70 % of cases. Analysis was performed using TEM on uranyl formate stained samples and 200 kV acceleration voltage for higher resolution, shown in figure 3.4B. Adding a higher excess of 6HB resulted in the attachment of multiple origami per PtNP. For example, a 12 times excess lead to the attachment of 5-8 6HB per PtNP, exemplary shown in figure 3.4C.

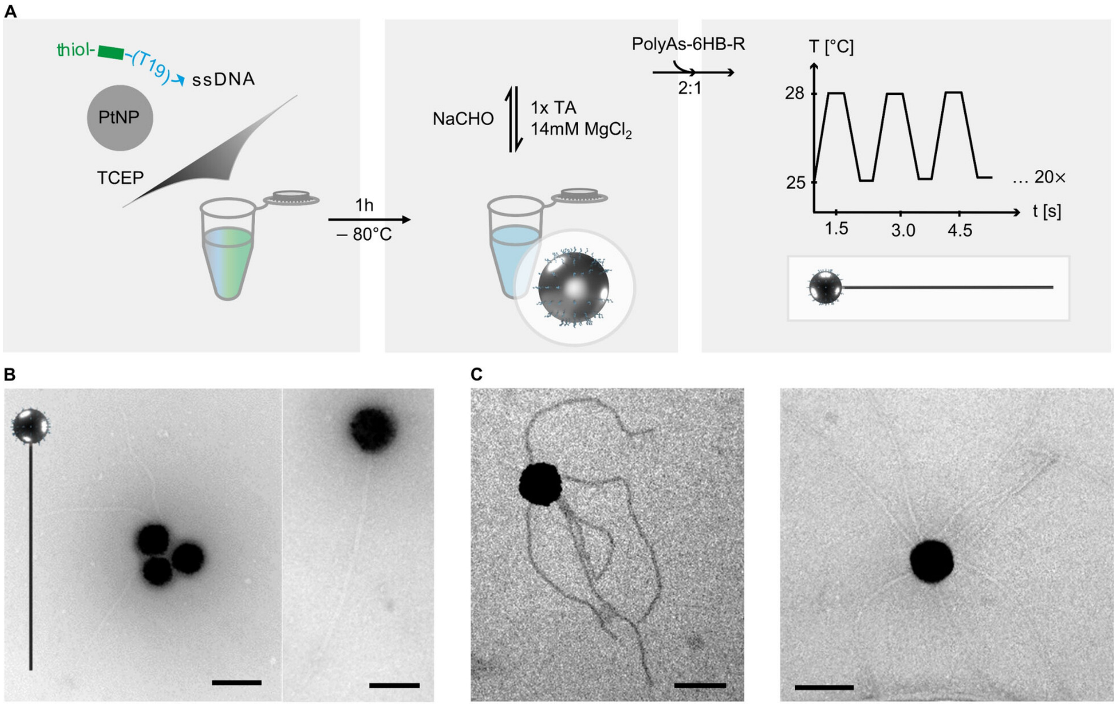

Figure 3.4: **A** Coupling protocol for the reliable binding of a single 6HB to 70 nm PtNPs. First the PtNPs were decorated with PolyT strands via (di)thiol linker. Incubation and freezing at -80 °C ensured sufficient surface coverage to achieve stability in origami buffer. Clean-up by centrifugation was followed by a 2:1 addition of 6HB to PtNP. Temperature ramping ensured optimal hybridization of PolyT to PolyA linkers. Finally, gentle centrifugation yielded 60-70 % of the desired 1:1 configuration. **B** TEM images of PtNPs with single 6HB attached. **C** TEM images of PtNPs with multiple 6HB attached. TEM samples were stained with uranyl formate and TEM was performed at 200 kV. Scale bars are 100 nm. Figure taken from[63].

To separate Au-6HB from the excess of free 6HB the literature performes native agarose gel electrophoresis. This purification method could not be translated to Pt-6HB in a proper way. PtNPs and Pt-6HB showed very little mobility in the gel and did not separate properly. Recovery of the sample by gel extraction through squeezing was unreliable and yielded only a low concentration of Pt-6HB, sometimes even contaminated with agarose. The samples were instead washed by gentle centrifugation at 3000 rcf for 3 min, which is technically simpler, but does not separate uncoupled PtNPs from the Pt-6HBs.

Au-6HB

To test if our adapted protocol also works for AuNP we repeated the procedure with 80 nm commercial AuNPs@citrate. As shown in figure 3.5 the coupling yields 1:1 Au-6HB constructs as well. Our protocol is therefore a valid alternative to the literature protocols with significantly shorter incubation times.

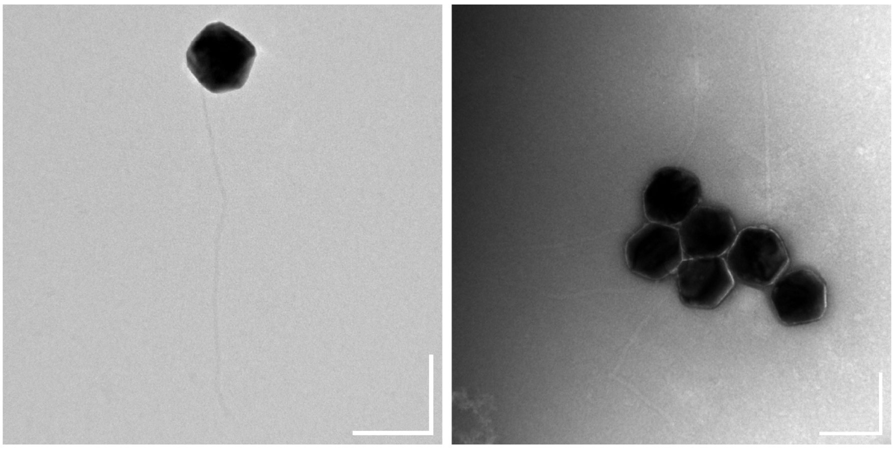

Figure 3.5: Exemplary TEM images of AuNPs with single 6HB attached. TEM samples were stained with uranyl formate and TEM was performed at 200 kV. Scale bars are 100 nm.

These Au-6HB particles are used later as control particles, as they are unreactive in H_2O_2.

3.3.4 Pt-6HB activity and stability in hydrogen peroxide

After successful coupling of PtNP to 6HB the catalytic activity of Pt towards hydrogen peroxide disproportionation was tested.

$$2\ \mathrm{H_2O_2} \xrightarrow{\mathrm{Pt}} 2\ \mathrm{H_2O} + \mathrm{O_2}$$

Qualitatively, the activity was observed by the formation of oxygen gas bubbles. For better visualization a sample of Pt-6HB was enclosed in a sandwich of cover glasses with and without the addition of 1 % H_2O_2, shown in figure 3.6B. Quantitatively, the disproportionation of H_2O_2 was observed via UV spectroscopy. To avoid refraction of the light beam by gas bubbles, experiments were performed at low H_2O_2 concentration of 0.05 %. AuNP, PtNP, PtNP-PolyT, and Pt-6HB were each diluted in 2 mM sodium citrate solution to a final concentration of $\approx 7.6 \cdot 10^8$ particles per mL. The absorption was measured for each solution individually and subtracted as background. Then, after addition of the appropriate amount of H_2O_2 and short mixing, the absorption of ultraviolet light (λ=240 nm) was tracked for each dispersion over 10 min. In that wavelength region the overwhelming contribution to light absorption comes from H_2O_2 molecules.[79] A decrease in absorption therefore indicates H_2O_2 disproportionation. The slope of the curves gives a reaction rate. The measurement of citrate buffer with H_2O_2 was used to normalize the obtained values, which are shown in figure 3.6A. AuNPs served as negative control and showed no change in absorption, as expected. The disproportionation rate for PtNP, Pt-PolyT, and Pt-6HB decreased in that order. This observation agrees with the assumption that the decoration of the particles surface leads to a decrease in exposed Pt area and therefore activity.

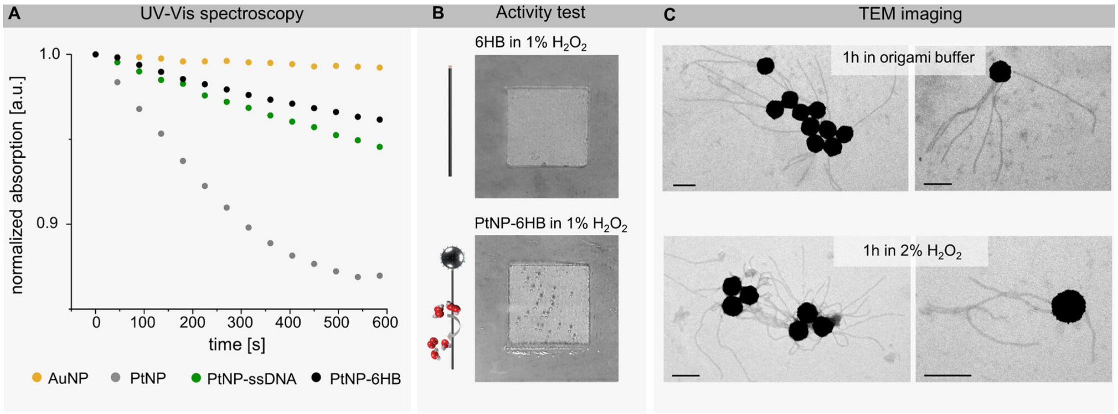

Figure 3.6: **A** Absorption of UV light (240 nm) observed over time as an indirect method to quantify H_2O_2 disproportionation activity. Normalized results are shown for AuNP, PtNP, Pt-PolyT, and Pt-6HB. **B** Sealed reaction chamber for the observation of oxygen gas, released as a result of H_2O_2 disproportionation. **C** Stability of Pt-6HB constructs in origami buffer and 2 % H_2O_2 over 1 h shown by TEM. TEM samples were stained with uranyl formate and TEM was performed at 200 kV. Scale bars are 100 nm. Figure taken from[63].

After proving the activity of Pt-6HB constructs, their stability in 2 % H_2O_2 at 20 °C was tested over the course of 1 h and analysed using TEM. Figure 3.6C shows Pt-6HB constructs with multiple 6HBs still attached, proving some stability in high H_2O_2 concentrations. Stability of Pt-6HB constructs in origami buffer was observed for at least 5 days at 20 °C, shown in figure 3.7A and B. Longer incubation times and higher H_2O_2

concentrations led to particle aggregation and detachment of 6HBs, shown in figure 3.7C and D. This is most likely due to Pt-thiol bond lability in oxidative environments.[80]

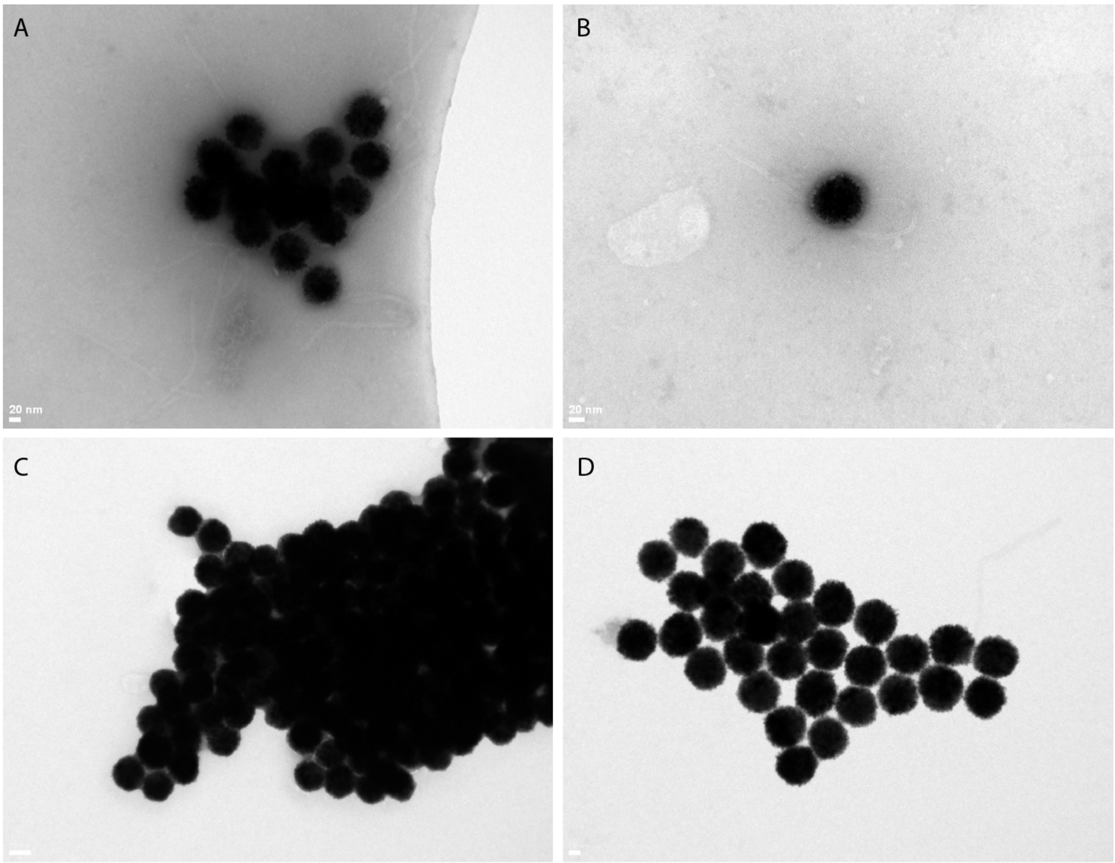

Figure 3.7: TEM images of Pt-6HB constructs **A**, **B** after 5 days in origami buffer and **C**, **D** after 1 day in 2 % H_2O_2 at 20 °C. C and D are adapted from[63].

3.3.5 Active Propulsion

The reaction rate difference observed for Pt-PolyT and Pt-6HB in figure 3.6A shows that 6HBs seem to have a shielding effect on PtNPs. To test if this break of symmetry is enough to produce active motion, Pt-6HB were tracked in hydrogen peroxide solution in a fluorescence microscope. At first the DNA origami were stained using SYBR Gold, then transferred to a bovine serum albumin coated cover slide sandwich with and without 1 % H_2O_2. The coating prevents the adhesion to the galss slides. To suppress oxygen bubble formation and to keep the H_2O_2 concentration constant, a final concentration of 5 µM glucose oxidase (GOx, from *Aspergillus niger*, type X-S) and 100 mM β-D-glucose (substrate) were added. The activity of GOx was tested qualitatively and semiquantitatively. GOx catalyzes the following reaction:

$$\text{Glucose} + O_2 \xrightarrow{\text{GOx}} \text{Gluconic acid} + H_2O_2$$

Active and passive particles were observed with a 63x objective (NA 0.75) and recorded in fluorescence mode, after illumination with a 470 nm LED (Zeiss Colibri) on 10 % intensity and a 504 nm beam splitter. Analysis was performed using the MOSAIC Suite plugin[81] for ImageJ (settings: radius=5, cut-off=0.001, Percentage=0.3-0.1, link range=3, displacement=7/10). Particles were tracked (passive: 76, active: 61) over 170-500 frames each. Examples are shown in figure 3.8. The derived diffusion coefficients were 0.61±0.12 µm·s^{-1} in buffer and 0.7±0.18 µm·s^{-1} in 1 % H_2O_2.

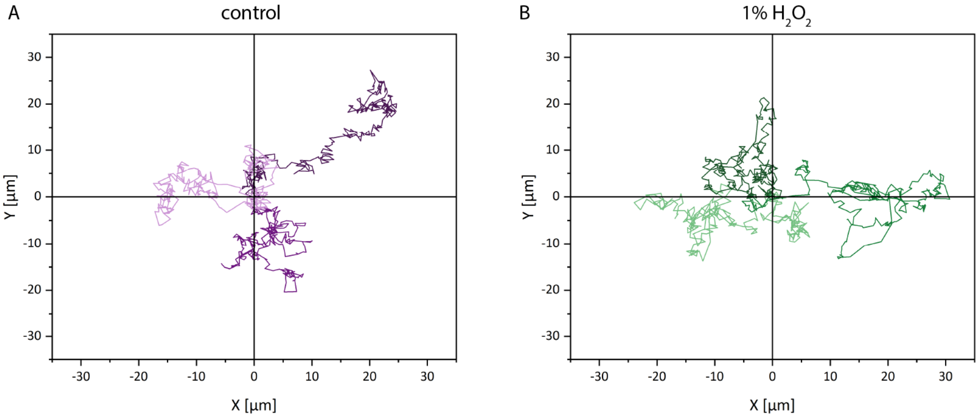

Figure 3.8: Exemplary tracks (300 frames) of Pt-6HB tracking analysis by fluorescence microscopy in **A** origami buffer as control (3 tracks, shades of purple) and **B** in 1 % H_2O_2 (3 tracks, shades of green).

Repetition of the same experiment with a new batch of Pt-6HB and identical analysis yielded 0.54 µm·s^{-1} for passive and 0.42 µm·s^{-1} for active constructs. Estimating the size of a spherical particle with these diffusion coefficients, using equation 2.4, yields around 900 nm in diameter, which means the diffusion coefficient is much smaller than expected.

The discrepancy may in part arise from surface effects, because the particles were observed in confinement, close to the glass surface. Since the tracking method only tracks fluorescent 6HBs, detachment of the 6HB from the PtNP goes unnoticed, thus creating an error in the calculated diffusion coefficients towards higher D values. Unfortunately the PtNPs were too small to be tracked directly using this method. There seems to be a significant error in the measured diffusion coefficients determined by this method. A different tracking method is needed to verify the acquired data or provide more realistic results.

Nanosight

In order to obtain more reliable data the experiment was repeated using an alternative method to tracking, provided by a Nanosight NS300 system (Malvern Panalytical). The working principle is based on a microfluidic chip, coupled to a laser (488 nm) that illuminates the sample. The scattered light is then recorded by a camera. This way short tracks of scatterers are recorded that are then subsequently analyzed. Alternatively the machine can operate in fluorescence mode, where the emitted light is filtered (500 nm long-pass filter) and then recorded by the camera. The sample can be imaged statically or dynamically by flowing it through the observation chamber with the help of a syringe pump. Free PtNPs are approximately symmetric and should not show any active propulsion in the presence of H_2O_2. Convective effects should also not arise in the used concentrations.[82] Additionally, their size is very small, resulting in much higher rotational diffusion. To reduce the impact of oxygen bubble formation and viscosity changes, H_2O_2 was used in low concentrations <1 %. For better tracking statistics the sample was pumped through the microfluidic chip to observe a large number of different particles, while making sure that the flow is slow enough (2-4 $\mu l \cdot s^{-1}$) to keep each particle ideally visible for at least 50 frames. The motion of the fluid flow is subtracted by the software. During the experiment the microfluidic tubes were covered in aluminum foil to prevent the formation of OH· radicals through UV radiation. The sample was diluted in 20 nm filtered buffer to achieve a concentration of $\approx 5 \cdot 10^8$ particles/ml. Each sample was tracked for at least 4 min (25 frames per second). For active diffusion, H_2O_2 was added in 0.5 % final concentration to the sample just before the measurement. The low concentration was necessary to avoid irregular fluid flows through gas bubble formation as much as possible. For the negative controls 20 µm filtered water was used instead of H_2O_2. The videos were analyzed using the NTA software (Malvern Panalytical) with manually adjusted detection settings and auto detected analysis settings, since each sample was different. The mean of the diffusion coefficients of all valid particle tracks within one sample were considered. All measurements are drift corrected in real-time by the software and shown in table 3.1.

Table 3.1: Tracking analysis of 6HB, Au-6HB and Pt-6HB, recorded using Nanosight NS300 and analyzed using the NTA software. Active samples contained 0.5 % H_2O_2, passive samples were substituted with filtered water. The mean values of diffusion coefficient are displayed in [µm·s^{-1}].

	6HB	Au-6HB	Pt-6HB	Pt-6HB (bc)
passive	5.17 ± 0.01	3.83 ± 0.15	3.80 ± 0.06	4.76 ± 0.08
active	5.17 ± 0.02	3.54 ± 0.36	4.15 ± 0.03	5.03 ± 0.09

As we can see from the results the diffusion coefficients of 6HB do not change with the addition of H_2O_2, as expected. Diffusion coefficients of the Au-6HB constructs are also expected to stay constant. The results however show a slight decrease in diffusion coefficient, potentially a results of Au-S bond breakage and subsequent partial AuNP aggregation. The same behaviour is to be expected for Pt-6HBs, which shows an overall increase in diffusion coefficient despite this counteracting effect. The increase for Pt-6HB is a first indication that the addition of 6HB might break the particles symmetry, resulting in self-phoretic motion when a fuel is added. Using equation 2.4 again, these diffusion coefficients for 6HB and Pt-6HB would correspond to calculated spherical particle of 87 nm and 120 nm diameter respectively, which is more reasonable. To be sure the enhancement is not a result of 6HB detachment, the experiment was repeated with a new batch of Pt-6HBs. The use of both operating modes during the measurement (bc, alternating) allowed observation of Pt-PolyT and Pt-6HB species in scattering mode (sc) and 6HB, Pt-PolyT, and Pt-6HB species in fluorescence mode (fl). Additionally GOx and its substrate were added to further suppress oxygen bubble formation. The mean results are shown in table 3.1. The individual diffusion coefficients for fluorescence and scattering mode were 5.11±0.056 µm·s^{-1} (fl) and 4.92±0.17 µm·s^{-1} (sc). Apparently some 6HB detach from the Pt-6HB constructs, resulting in an overall higher diffusion coefficient in fluorescence mode. What is surprising though, is the difference in absolute diffusion coefficients for Pt-6HB in separate batches and measurements, while the increase for the active samples remains. An explanation would be that a different amount of 6HB attach during the coupling procedure leading to different percentages of empty Pt-PolyTs in the sample. This variability in measured diffusion coefficients has been observed several times and could also be a result of the tracking analysis conditions. While the detection parameters have to be chosen according to the sample requirements, the minimum track length (in frames) can be varied. More restrictive settings of higher minimum track lengths lead to lower valid track numbers and poorer statistics, but represent particles that were visible for longer times in the focal plane. Depending on the particle brightness potentially only a sub-population would be observed. In table 3.2 are the results from Pt-6HB (bc), analysed with different minimum track lengths.

Table 3.2: Tracking analysis of Pt-6HB (bc), recorded using Nanosight NS300 and analyzed using the NTA software with different minimum track lengths of 7, 10, and 12 frames. Active samples contained 0.5 % H_2O_2, passive samples were substituted with filtered water. The mean values of diffusion coefficient are displayed in [µm·s^{-1}].

	7	10	12
passive	5.50± 0.13	4.38 ± 0.09	4.31 ± 0.05
active	5.44 ± 0.21	4.33 ± 0.14	4.25 ± 0.16

Analysis with different tracking settings significantly changed the results. Depending on the minimum track length, there was no observed diffusion enhancement and the total values for diffusion coefficients changed significantly. Both tracking attempts have led to ambiguous results. Future attempts should re-consider separating Pt-PolyT from Pt-6HBs. Additionally, the analysis parameters need to be optimized for each sample and consistently used throughout the analysis. A different tracking setup would need to be constructed which contains access to the software's algorithm. However, despite these difficulties an upper limit can be deduced, in that the enhancement in effective diffusion is $D_{\text{eff}}/D < 4$ %.

3.4 Summary

A first attempt at combining DNA origami as versatile scaffolding material with Pt-NPs as catalytically active components has been presented. A known DNA origami construct, the 6HB, was adapted to carry three overhangs on each side, to gain separately addressable anchor points. After successful folding the 6HB stability was tested in hydrogen peroxide solutions of up to 5 % concentration over the course of three days. Surprisingly, we found no evidence of structural damage, observed by electrophoretic mobility and TEM analysis. The concentrations represent common working conditions used with catalytically active Pt Janus motors. A coupling protocol for 70 nm PtNP to 6HB was delevoped, based on existing literature for AuNP to DNA origami binding procedures. By adjusting the ratio of 6HB to PtNP during the procedure the number of attached 6HB per PtNP can be directed. A ratio of 2:1 results reliably in a 1:1 configuration for 60-70 % of observed constructs. The use of higher amounts of 6HB leads to attachment of multiple 6HB simultaneously. The protocol was shown to also achieve coupling of AuNP to 6HB in a similar manner in a few hours, compared to at least 3 days in literature procedures. The Pt-6HB constructs and precursors were subjected to H_2O_2 solutions, where the catalytic activity towards the disproportionation of H_2O_2 was shown qualitatively and quantitatively. As expected the surface functionalization of PtNPs leads to a decrease in the reaction rate due to a decrease in exposed Pt surface area. The stability of Pt-6HB was shown by TEM for at least 5 days in buffer and 1 h in 2 % H_2O_2. The weakest link in the construct is likely the Pt-S bond, which is labile in oxidative environments, leading to disassembly and aggregation of Pt in solution. In order to provide higher resilience to oxidative stress an entirely different PtNP surface functionalization strategy would be required. Tracking of Pt-6HB motion in H_2O_2 using direct tracking proved to be unreliable. In any case the enhancement in diffusion is small. Observation using Nanosight provided a hint that any increase through active motion will be less than 4 %. The small diameter of the 6HB was likely not enough to create a significant concentration gradient. Future DNA origami constructs should increase the fore-aft asymmetry. The use of larger constructs should simplify the tracking conditions and exhibit larger effects. Thicker DNA constructs could also help maintain a larger concentration difference.

4 Degradable magnetic microcarriers

Magnetically propelled swimmers offer a fuel-free alternative to chemical motors. Active, tetherless steering can be implemented leading to a promising class of swimmers suitable for biological environments.

4.1 Introduction

Alternative propulsion strategies for micro- and nanoswimmers include magnetic, acoustic or light stimuli.[83] While light-driven propulsion methods can achieve fuel-free, directed propulsion via thermophoresis, most examples still involve a fuel and photocatalytic semiconductors, like TiO_2.[84] Furthermore they are limited by the penetration of light into (biological) samples, making them more suitable for environmental remediation, rather than biomedical applications.

A relatively new strategy utilizes acoustic waves for propulsion. The concept was first shown in 2012 by Wang *et al.*[85] and was initially limited to microrods and wires.[86] Ultrasound waves experience a high-density contrast, between a liquid and metals or entrapped gas bubbles and exert forces, but also move liquid via streaming. The motion profile is explosive and short lived, achieving remarkable speeds, yet without any steering capabilities. Sound waves have a high penetration depth, making them potentially suitable for biological samples.

Magnetically propelled swimmers however have the highest potential to be used in biomedical applications. Their most significant advantage is the remote controllability in three dimensions, independent of chemical fuels or gradients. Propulsion is instead achieved through weak external magnetic fields, produced by electromagnetic coils, that have no side effects when interacting with biological matter.[87] The magnetic coils can in principle be scaled to human anatomy, leading to unparalleled targeting capabilities. However, this is technically still challenging. The downsides are the more complex fabrication and material requirements to realize such a swimmer design and the large electromagnets and power supplies that are needed when the sample volume is large. Propulsion is realized by the swimmer shape, as discussed in the theory section. The materials required to fabricate magnetic micro- and nanoswimmers in specific and asymmetric shapes are mostly inorganic, especially when the required dimensions of the propellers are below 10 µm. The small size is needed to fit through biological barriers and interact with biological machinery on their length scales. Very few fabrication methods have achieved the required resolution and scaling capabilities to produce a large number of uniform micro- and nanoparticles so far. The first microswimmers with a helix diameter of around 500 nm were fabricated by our group in 2009[34] using GLAD. Later we showed the fabrication of helical swimmers as low as 120 nm diameter.[88] The small size was necessary to achieve propulsion in complex viscous media, often found in biological tissue and fluids. Modern 2-photon polymerisation based 3D printing techniques can fabricate soft helical microswimmers with diameters in the range of 10 µm,[89] but the huge drawback is the printing speed of around 10 s per structure.[90] Since every helix needs to be printed individually it takes very long to write a large number ($\approx 10^6$) of swimmers, making this technique more suitable for applications that require a few selected structures.

Commonly used magnetic materials are Fe and its oxides, as well as Ni, and Co. While Ni and Co possess desirable hard magnetic properties, they are toxic to cells (animal and human).[91,92] While iron based materials are considered biocompatible, the dosage is important.[93–96] Especially dissolved Fe^{2+} ions can cause oxidative stress through the Fenton reaction.[97] therefore, using the lowest amounts of magnetic material possible or shielding it from the environment should ensure sufficient biosafety. This requires materials with high remanent magnetization and a coercive field large enough to prevent re-magnetization, where FePt $L1_0$ nanomaterials show some of the highest magnetic strength recorded.[98] Additionally FePt is shown to be biocompatible[99], which makes it an excellent choice to fabricate magnetic micro- and nanoswimmers.

While micro- and nanoswimmers have shown potential to be used in targeted drug delivery, most are non-degradable and raise biosafety concerns.[100] Coatings of chemically inert materials, like gold, might prevent direct interaction with the biological environment. However, the coating causes the accumulation of micro- and nanoparticles in the human body, which may lead to chronic inflammation.[83,101–103] To avoid these biosafety concerns altogether the use of (bio-)degradable particles is the best strategy forward. In this context 'biodegradable' is used for decomposition mechanisms through biological activities, *e.g.* enzymatic, while 'degradable' systems refer to chemical corrosion processes through interaction with the surrounding medium. (Bio-)degradability however adds additional material constraints to an already challenging engineering task. The development of a fully degradable system capable of actively guided motion on this length scale could not be shown yet. However, recent research shows partially biodegradable magnetic microswimmers, made out of a degradable matrix that incorporates Fe_3O_4 NPs. In one case helical algae of 5 µm diameter have been dip-coated in Fe_3O_4 dispersion.[104] In other cases microparticles were fabricated by encapsulating Fe_3O_4 nanoparticles during the synthesis process. These particles rely on their random, asymmetrical shape and internal Fe_3O_4 NP distribution to achieve magnetic propulsion. The random shape however results in a different propulsion direction for every microparticle, making collectively guided motion impossible.[105,106]

4.2 Motivation

With the recent implementation of a biocompatible FePt layer of only 50 nm thickness into a helical microswimmer by our group[107] we have proven that very little magnetic material is needed to achieve excellent hard magnetic properties. While the helical body made of SiO_2 is also biocompatible, it still presents a micron-sized object, which would remain in the patients body with currently no means of retrieving it. This project concerned the development of a suitably sized magnetic microcarriers, which should show degradability under physiological conditions to eliminate long-term safety concerns.[108] This is a necessary step in the research effort to progress towards *in vivo* drug and gene delivery, which so far has not been addressed properly. Moreover, a degradable body opens up the possibilities for the gradual release of its cargo.

4.3 Results

The results of this project have in part been published in:
Peter, F.; Kadiri, V. M.; Goyal, R.; Hurst, J.; Schnichels, S.; Avital, A.; Sela, M.; Mora-Raimundo, P.; Schroeder, A.; Alarcón-Correa, M.; Fischer, P. *Advanced Functional Materials* **2024**, *34*, 2314265

Contributions
VMK and PF conceptualized this work. Preliminary fabrication and degradation experiments were performed by VMK. Fabrication optimization, systematic degradation studies, propulsion, cargo loading and release studies were performed by FP, supervised by MAC and PF. RG assisted in some propulsion experiments and maintained the magnetic coils. JH performed biocompatibility tests with supervision of SS. AA, MS, PMR and AS fabricated the used liposomes.

4.3.1 Fabrication

The magnetic microswimmers of this chapter have been made using glancing angle physical vapor deposition (GLAD). The working principle is explained in the respective theory section. The deposition thicknesses given in the text are corrected by the estimated deposition ratio R_0 that accounts for the deposition conditions, introduced in section 2.4.1, and should as such represent the estimated real thickness values. R_0 is provided for each deposition. GLAD allows the controlled deposition of materials on a substrate, covered with a monolayer of seed particles. By tilting the substrate to an extremely oblique angle the seed particles shadow each other, allowing the growth of distinct columns on each individual particle. Rotation of the substrate allows for column shaping to produce billions of three-dimensional structures on a 2 inch (5.08 cm) wafer.

Degradable material candidates have already been investigated at large scales. Alloys and glasses of Mg, Zn and Ca found application as degradable orthopedic implants and suture materials.[109–117] These implants underlie rigorous biocompatibility testing standards for medical devices (ISO 10 993).

Alloying is commonly used to tune and alter the characteristics of materials when individual elements alone do not possess the desired properties. For biomedical implants the degradation rate of pure Mg in physiological media was too high.[118–120] In order to influence the corrosion behaviour, slow corroding metals, like Zn and Ca, were mixed in. This approach has been adapted by us to the microscale for the fabrication of magnetically actuated microswimmers. The combination of different materials should retain a similar adjustability of the corrosion properties, which allows for flexibility. The translation to the nano- or microscale has not been achieved previously, since traditional metallurgical processes operate on larger scales. Furthermore, the low melting temperatures of Mg (650 °C) and Zn (420 °C) are not compatible with the higher annealing temperature for FePt (≈680 °C),[121] which causes additional problems. Important properties for GLAD deposition are deposition rate and handling. Additionally, each material's corrosion behaviour was considered theoretically. In a first study Mg, Zn, Ca and their respective oxides were evaluated. Ca was considered unsuitable, because it corrodes in contact with air and sublimates at 459 °C, which makes the deposition rate very hard to control. Calcium oxide is not suitable for e-beam deposition.[122] The Mg deposition quality is good, but the vapor pressure increases rapidly with temperature, leading to very high deposition rates and material overspray. Zn is an excellent deposition material and corrodes slowly. MgO and ZnO are practically insoluble in water[123], but they react with water. The corrosion rates are dependent on the solvent conditions. MgO is commonly used as a protective layer for pure Mg and its corrosion resistance can be improved by annealing,[124,125] but the deposition rate is very low, making long depositions impractical. ZnO reacts slowly with water[126], but is a poor deposition material. Mg and Zn have therefore been identified as highly promising degradable materials.

The deposition conditions have to be optimized to ensure optimal growth. Especially for co-depositions the proper calibration of the QCM feedback loop is essential to achieve the desired ratios of the deposited materials. Misalignment leads to systematic errors. The alignment quality of our system is evaluated later by the quantified degradation results that give insight into the actual deposition ratios of Mg to Zn, compared to the theoretical values. Preliminary design choices and the first helix co-depositions with Mg and Zn have been performed by my colleague Dr. Vincent Mauricio Kadiri and are published in his thesis.[127] Mg is a volatile deposition material that requires specific adaptations to existing deposition procedures. It is operated at extremely fast deposition rates of $2 - 5\ \text{nm} \cdot \text{s}^{-1}$, which results in substrate heating and in column broadening, which fuses individual structures together when the deposition length exceeds a few hundred nanometers. To mitigate this effect the seed particles were spaced further apart, to allow more room in between individual structures. For this purpose a Si(100) substrate was first patterned with 1 µm polystyrene beads in a hexagonal close-packed monolayer by Langmuir-Blodgett deposition. The beads were carefully placed on the water/air interface in a Langmuir-Blodgett trough, pushed together until they form a monolayer on the surface and transferred onto the silicon wafer.[128] Subsequent oxygen plasma etching for 8 min at 300 W reduced the bead diameters to ≈ 560 nm,[127] shown in figure 4.1. SEM imaging was performed using an InLens detector and 5 kV acceleration voltage.

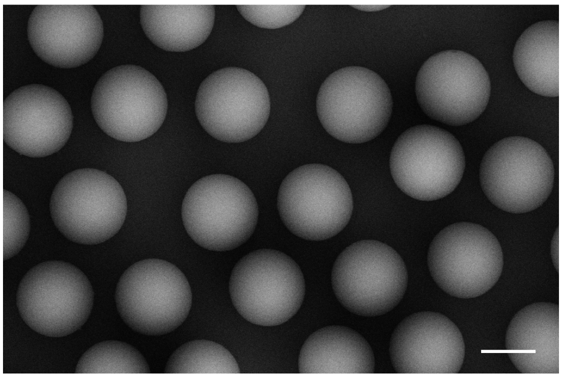

Figure 4.1: SEM image of hexagonally patterned PS beads after oxygen plasma etching. Scale bar is 500 nm. Figure taken from[129].

Additionally the substrate holder can be cooled to −90 K to reduce adatom diffusion during deposition. The seed particle spacing however increases the exposed area on the seed particles, resulting in a less defined helix with increased diameter. Exemplary structures by VMK are shown in figure 4.2.

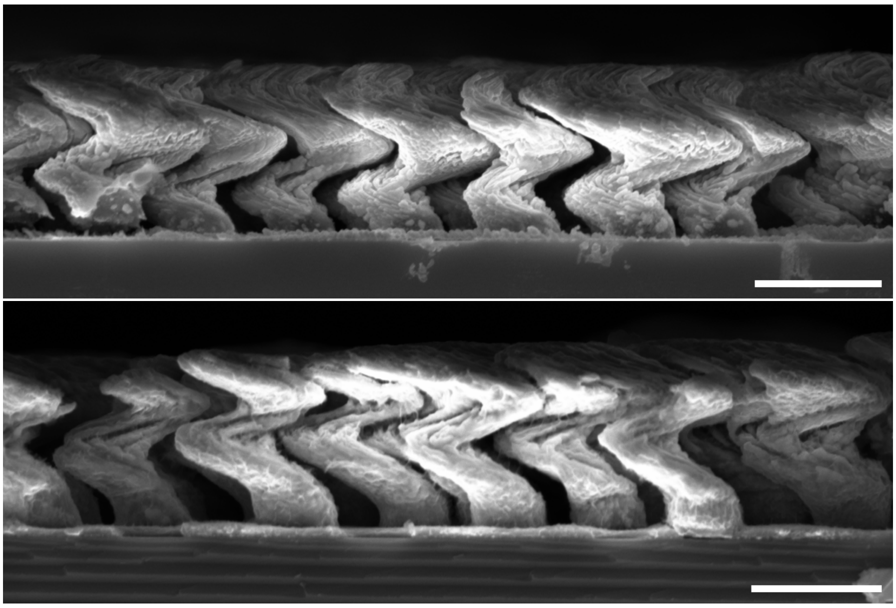

Figure 4.2: SEM images of MgZn 70:30 (upper) and 50:50 (lower) helices with 1.1 µm length and 1.5 turns. Fabrication performed by VMK, deposited at an incident angle of 85°. Scale bars are 1 µm.

To negate this side effect I increased the incident angle to 87°, which reduces the exposed area, effectively reducing the helix diameter. I also reduced the deposition length to reduce column broadening effects and increased the pitch to create less turns, which reduces the experienced drag and results in higher translation per turn, in accordance with previous findings from our lab.[130] R_0 is estimated as 0.6. The corrected deposition length is different from the measured helix height in that it represents the length of a straight rod that has been wound into a helix of the measured height. The final shapes obtained by this improved procedure can be seen in figure 4.5.

As discussed in the theory section, conventional magnetic materials possess sub-optimal magnetic properties and raise biosafety concerns. However, FePt in its $L1_0$ phase is biocompatible and has excellent magnetic properties on the nanoscale.[99] The vapor deposition growth of FePt microstructures has recently been realised by our group[121] and is therefore perfectly suited for the new design. Due to its extremely high magnetic remanence and coercivity in a thin film of 10 nm or less,[98,131] only a very small amount of material is needed. The annealing temperature to achieve the right crystal structure of FePt is around 700 °C,[121] and therefore higher than the melting points of Mg and Zn. Annealing attempts at slightly lower temperature of 650 °C after the helix growth still resulted in collapsed structures, shown in figure 4.3. The deposition order had to be inverted to permit for the annealing of FePt at 700 °C before depositing Mg and Zn.

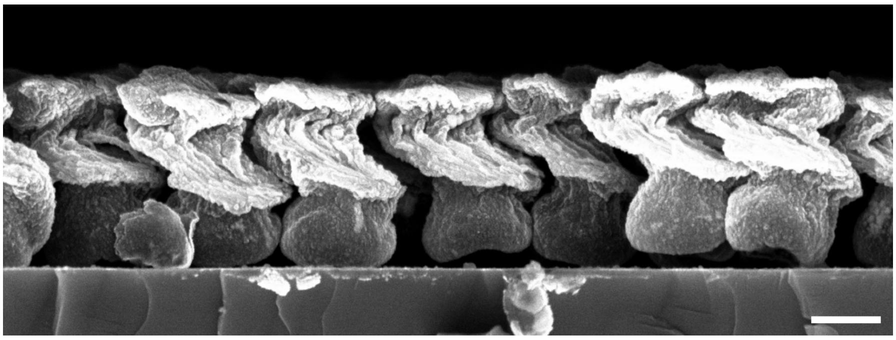

Figure 4.3: SEM image of MgZn 60:40 helix design after annealing at 650 °C. Scale bar is 1 µm.

The updated deposition procedure includes a thin layer of 4 nm MgO, deposited around the beads for better adhesion[131] at a deposition angle of 65 °C. The low deposition angle ensured exposure as far down to the side of the seed particles as possible.[127] Co-deposition of 16 nm FePt at an atomic ratio of 1:1 was followed by another 4 nm of MgO, all at 65° and from all sides. R_0 is estimated as 0.8. Given that at any given time only half of the bead is exposed to the vapor flux the real thickness is only half of the corrected thickness, which corresponds to $R_0 = 0.4$. The wafer was subsequently removed from the deposition chamber, cut into thin pieces, sealed in quartz ampules under vacuum (or Argon atmosphere) and annealed at 700 °C for 1 h with subsequent flash cooling in an ice bath. The annealing process favors the $L1_0$ phase and thermolyses the PS beads, which removes a non-degradable part of the swimmers. The FePt half-spheres remained mostly in their original hexagonal pattern, as shown in figure 4.4. The deposition at 65° was important, because the half-cups are now tall enough to still create the needed shadow effect for the next deposition.

The fabrication was then finished with the optimised Mg and Zn co-deposition in desired ratios of the two materials. Mg contents of 90, 80, 70, and 50 atomic % were grown, according to the integrated QCMs. A scheme of the final deposition procedure is given in figure 4.5a.

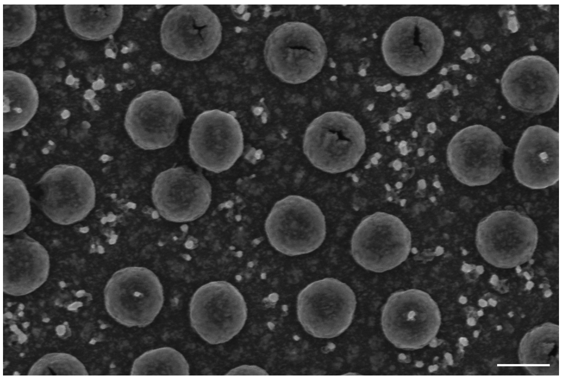

Figure 4.4: Patterned substrate after FePt co-deposition and annealing. Figure taken from[129].

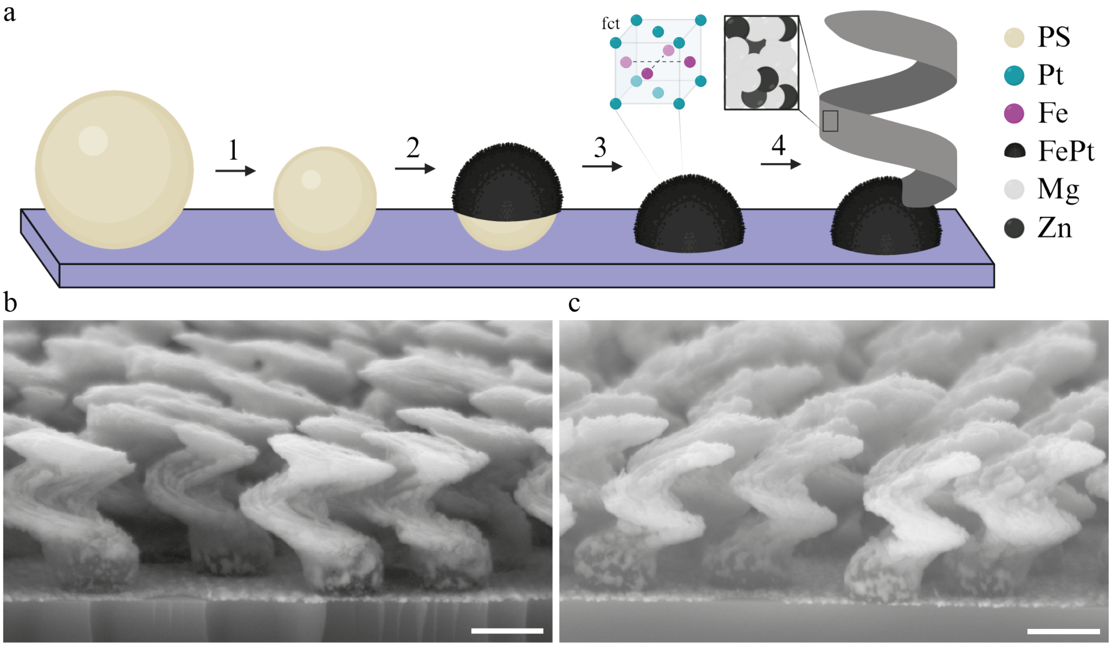

Figure 4.5: **a** MgZn propeller fabrication scheme. Step 1: O_2 plasma etching, step 2: FePt co-deposition, step 3: FePt annealing under vacuum, step 4: MgZn helix co-deposition. Created with BioRender.com. **b** SEM image of 70:30 and **c** 80:20 MgZn propellers on the wafer, tilted by 10°. Scale bars are 500 nm. Figure taken from[129].

The magnetic characteristics of the fabricated propellers were determined with a superconducting quantum interference device (SQUID). The hysteresis loops from -3 T to

+3 T are shown in figure 4.6, scaled for a single propeller and volume of FePt present in the sample. The scalings are given below.

The propellers were grown originally on a hexagonal close packed pattern of beads with a diameter of 1 µm. By projecting the beads onto the surface we can treat this as a packing of circles in a hexagonal orientation, which is the densest form of packing.[132] The achieved packing density is

$$\frac{\pi}{\sqrt{12}} \approx 0.9069.$$

Thus, we can calculate the number of beads N_p (and therefore propellers) per area of substrate A_sub as the packing density divided by the projected area of a single bead A_bead:

$$\frac{N_\mathrm{p}}{A_\mathrm{sub}} = \frac{1}{A_\mathrm{bead}} \cdot \frac{\pi}{\sqrt{12}}$$

For the 1 µm beads used in this thesis we find a propeller density of

$$\frac{N_\mathrm{p}}{A_\mathrm{sub}} = \frac{1}{\pi \cdot (0.5 \cdot 10^{-3}\ \mathrm{mm})^2} \cdot 0.9069 = 1.16 \cdot 10^6\ \frac{\mathrm{propellers}}{\mathrm{mm}^2}$$

or a total of $2 \cdot 10^9$ propellers on a 2 inch (5.08 cm) wafer. Dividing the measured magnetic moment (with SQUID) by the number of propellers on the measured substrate size, yielded the magnetic moment per propeller. The remanent in-plane magnetic moment was calculated to be $7.4 \cdot 10^{-12}$ emu per propeller. To calculate the material properties of FePt $\mathrm{L1_0}$ we need to estimate the volume of magnetic material, present on the measured substrate. This was estimated by assuming a FePt half-shell around a sphere of 550 nm. The thickness of the shell is 16 nm. The half-shell volume was then calculated as half the difference between two sphere volumes with diameters 550 nm and 564 nm. With this, the remanent magnetization of FePt $\mathrm{L1_0}$ is 886 $\mathrm{emu} \cdot \mathrm{cm}^{-3}$, which is even higher than previous measurements by our group.[121] To put this into context, the magnetization of superparamagnetic magnetite nanoparticles, which are commonly incorporated into different swimmer designs, achieved in a magnetic field of 10 mT is $\approx 10\ \mathrm{emu} \cdot \mathrm{cm}^{-3}$.[106] The coercivity was determined from the hysteresis curve to be 1.8 T.

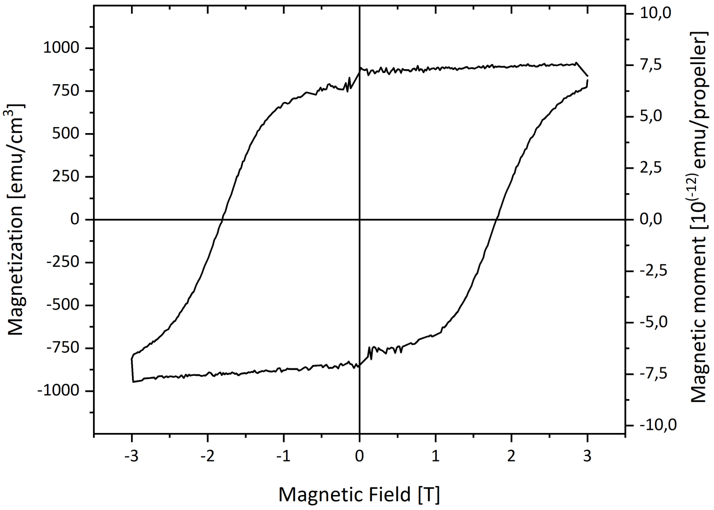

Figure 4.6: SQUID in-plane hysteresis loop of fabricated FePt half-spheres at 20 °C. Adapted from[129].

Exemplary SEM images of Mg to Zn ratios 80:20 and 70:30 are shown in figure 4.5b and c, taken with an SE2 detector and 5 kV acceleration voltage. The SE2 detector was used, because the high contrast between FePt and MgZn created imaging problems. The total length of the helix was measured from the SEM image as ≈ 800 nm with an outer helical diameter of ≈ 750 nm, a filament thickness of ≈ 350 nm and a pitch of ≈ 600 nm. The head of the swimmer adds roughly ≈ 300 nm in length. These dimensions are similar to previous designs[133], where these dimensions were shown to permit transport through the gel-like macromolecular network of the vitreous humour inside the eye.[133] Envisioning a similar application the specifications were kept, but the fabrication is flexible, so that diameter, length and pitch can be adjusted if the requirements change.

4.3.2 Degradation

After successful fabrication the corrosion rates of propellers of different ratios of Mg and Zn were investigated. The literature offers extensive studies on degradation behaviour and kinetics *in vitro*[111,112,134–139] and *in vivo*[113,116,140,141] on the macro scale. Generally, a higher Zn content should slow down corrosion.[142–145] Although, this is only an estimation, since corrosion processes are complex and depend on material purity, shape, composition, as well as pH, fluid flows, ion content and ion strength of the medium.

The degradation behavior was investigated primarily in water to achieve a basic understanding of the system. More complex environments require individual studies for the targeted environment. Firstly, wafers of MgZn propellers with different ratios were immersed in DI water (ion exchanged with a remaining resistivity of 18.2 MΩ·cm and filtered with 200 µm pore size) at 37 °C and sonicated to release all propellers. At regular time intervals a sample was dried, washed and imaged by SEM. To not artificially increase the degradation rate the sample containers were not shaken to avoid mechanical degradation.

From figure 4.7 we can see that a higher Mg content leads to comparatively faster degradation, which is in agreement with the macroscopic corrosion behaviour of MgZn structures.

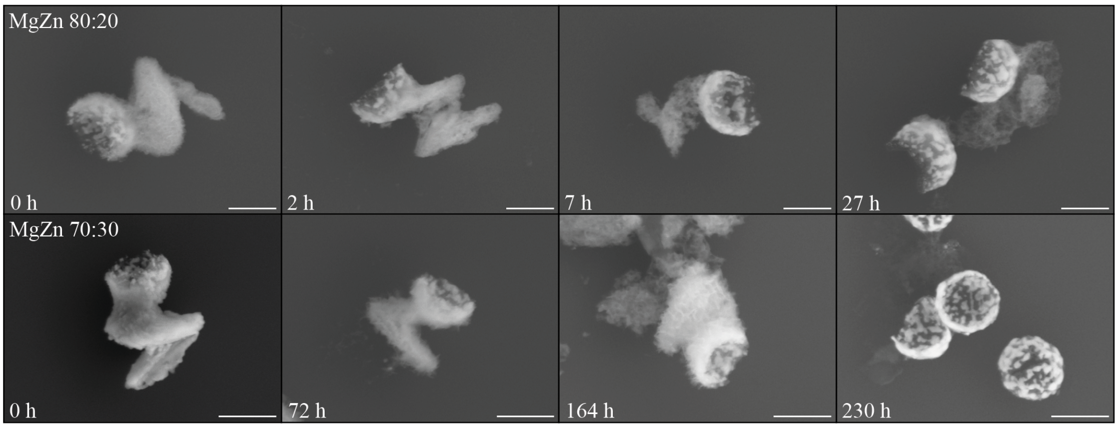

Figure 4.7: SEM images of MgZn 80:20 and 70:30 micropropellers imaged at different intervals during the degradation process in DI water at 37 °C after sonication. An aliquot was removed at the indicated times, washed and imaged. Scale bars are 500 nm. The images are shown at comparable levels of degradation. Figure taken from[129].

Propellers with a Mg content of 90 % degraded completely in under 6 h. For a typical biomedical workflow including cargo loading, administration, and propulsion, the micropropellers need to remain structurally and functionally intact for at least 24 h. Propellers with a high Mg content of more than 80 % were therefore excluded in the subsequent experiments.

Samples with only 50 % Mg took several weeks to display signs of corrosion and thus remain of interest for possible applications, but make experimental observations difficult in a reasonable amount of time. MgZn ratios of 80:20 and 70:30, as shown in figure 4.7, provide the optimal lifetimes in DI water. For instance, the first signs of degradation are observed after a few hours for the MgZn 80:20 structures, whereas a comparable state is reached only after three days for the 70:30 structures.

These relative observations in free suspensions are expected to differ from the corrosion behaviour observed on the wafer, due to the spacial restrictions. However, for technical reasons, and to avoid sonication steps, the quantification of corrosion rates had to be measured under those simplified conditions. MgZn ratios 80:20, 70:30, and 50:50 were investigated. A wafer piece of known size of each sample was immersed separately in 5 ml of DI water at 20 °C over 11 d. After each time point the wafer was carefully transferred to a fresh solution. At the end of the experiment the remaining wafer piece content was dissolved in 5 ml of 0.1 M HCl. The increase in ion concentration of all solutions were measured with the help of Samir Hammoud (MPI for Intelligent Systems, Stuttgart), using inductively coupled plasma - optical emission spectroscopy (ICP-OES). The ratio of Mg to Zn in the respective samples was determined to be 81 %, 66 %, and 48 % (all determined with an accuracy of ±2 %), which agrees well with QCM measurements during the fabrication. This confirms that the ratio of Mg and Zn can be precisely set during fabrication.

The cumulative amounts of metal ions detected in each sample, shown in figure 4.8a, charts the overall degradation progress over time. The values are normalized to the total amount of ions detected for each sample.

From this we can confirm that the corrosion rate correlates with the amount of Mg in the structure: the higher the Mg content, the faster the structure degrades. Unsurprisingly, the overall corrosion rate is slower than in free solution at slightly higher temperature and after sonication. If we separate the detected ions further into individual ion types, shown in figure 4.8b, we can see that Mg is dissolving much faster than Zn. After 11 days only $\approx$ 5–20 % of Zn content initially present in the structures could be found in solution. SEM images of the remaining samples after 11 d in DI water in figure 4.8c, d show that the remains were still recognizable helical structures, that appear to be porous, 'hollowed out'. This suggests that the MgZn helix corrodes not uniformly, but instead the Mg is dissolved out of the structure first, leaving a Zn mesh behind.

Looking at the corrosion behaviour of MgZn 50:50 we can estimate the corrosion of Mg to be 10 times faster than Zn, which is in agreement with values of 2-20 times, found in literature. As an example, a tube of 2 mm outer diameter and 0.15 mm wall thickness immersed in Hank's buffer solution showed a corrosion rate of 0.028-0.037 mm per year compared to 0.61-0.73 mm per year for Mg.[114,136,138]

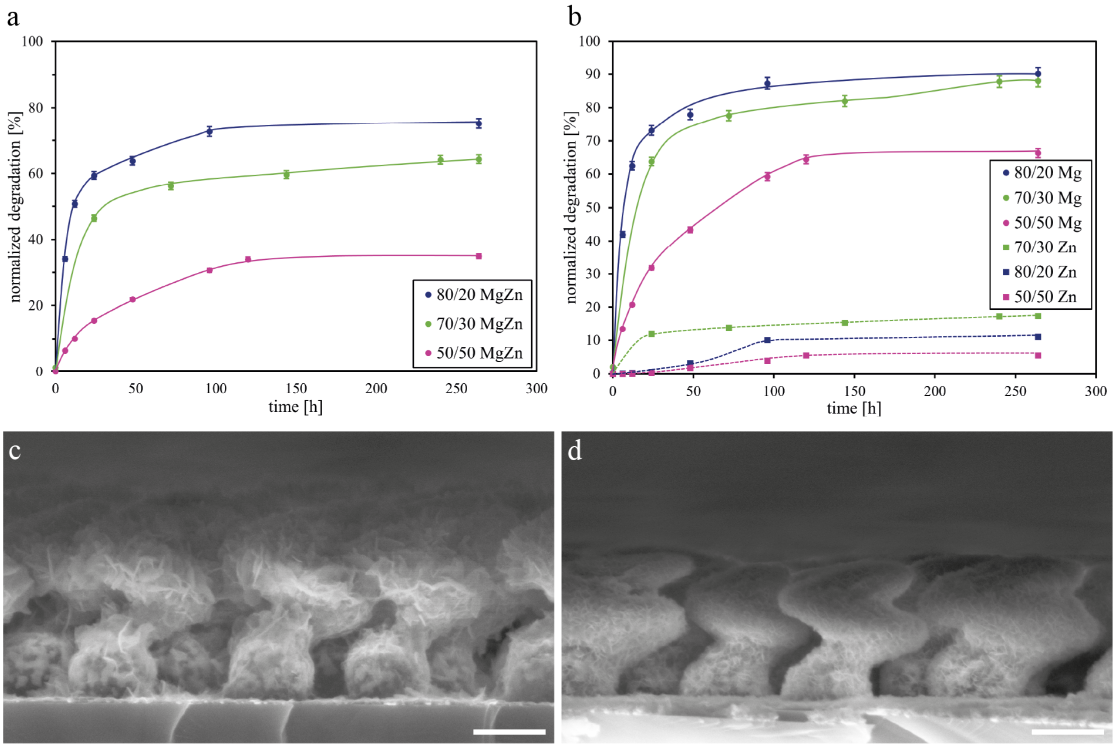

Figure 4.8: ICP-OES analysis of the degradation time series of MgZn propellers in DI water at 20 °C for different ratios of Mg to Zn. **a** Quantification of dissolved Mg and Zn ions, for each ratio, normalized to the total amount of Mg and Zn obtained when dissolving the entire sample. **b** Measurement of dissolved Mg and Zn ions over time, separated by ion type, and normalized to the total amount. SEM images of MgZn **c** 70:30 and **d** 80:20 samples on the substrate after 11 d in DI water. The lines only serve as guides to the eye. Scale bars are 500 nm. Figure taken from[129].

Since the corrosion behaviour in physiological media is expected to differ from degradation behaviour in DI water, the experiment was repeated over a period of three days in common cell culture medium, namely Dulbecco's Modified Eagle Medium (DMEM), for MgZn 70:30 and 80:20 ratios. The degradation progress, shown in figure 4.9 is different from the behaviour observed in DI water. The overall degradation rate in DMEM is similar, but the differences between different ratios is not as distinctive anymore. When comparing the individual ion contents in figure 4.9b the degradation rates for Mg and Zn were inverted, with now Zn dissolving faster than Mg. After one day almost no Zn remained in the structures and after three days all the original Zn content was dissolved.

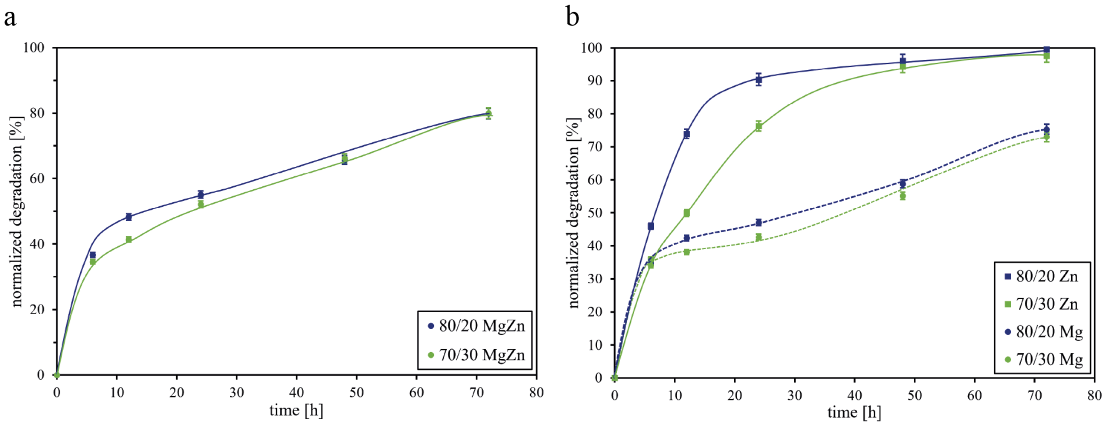

Figure 4.9: ICP-OES analysis of the degradation time series of MgZn propellers in DMEM at 20 °C for different ratios of Mg to Zn. **a** Quantification of dissolved Mg and Zn ions, for each ratio, normalized to the total amount of Mg and Zn obtained when dissolving the entire sample. The lines only serve as guides to the eye. Figure taken from[129].

This changed behaviour is most likely due to the presence of salts in DMEM. Especially chloride ions can react with the protective ZnO layer and form highly soluble ZnCl$_2$.[83] This proves that the corrosion behaviour of Mg and Zn are strongly dependent on the surrounding medium and need to be tested in each individual fluid they are used in.

4.3.3 Biocompatibility

To investigate the biocompatibility of our MgZn propellers during degradation, toxicity assays were performed by the Schnichels lab (Center of Opthalmology, University Eye Hospital Tübingen). Clinically relevant ocular cells, including the the human cell lines ARPE-19 (RPE cells) and MIO-M1 (Müller cells), as well as primary porcine RPE cells were treated, as they represent possible target sites, with high cell-to-propeller ratios of up to 1:20 for 48 h. An MTS-assay was performed to determine cell viability, crystal violet staining for cell density and apoptosis onset was investigated via caspase 3/7-assay. A decrease in cell viability and cell density or an increase in Caspase 3/7 activity indicates a negative impact on the cells. To account for fast degradation MgZn 80:20 propellers were used. The results are shown in figure 4.10, where the cell viability and density remained unchanged for all tested cells. For ARPE-19 and MIO-M1 cells the caspase 3/7 activity was slightly reduced after 48 h for higher propeller concentrations. In short, all assays confirmed a high biocompability in all tested cell lines over 48 h.

a Primary RPE cells

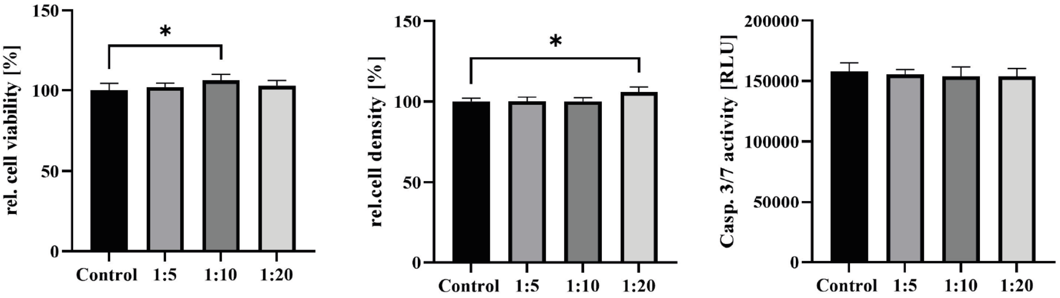

b ARPE-19 cells

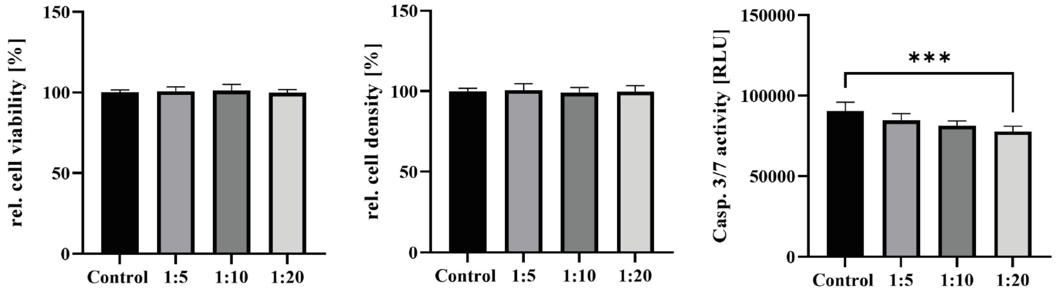

c MIO-M1 cells

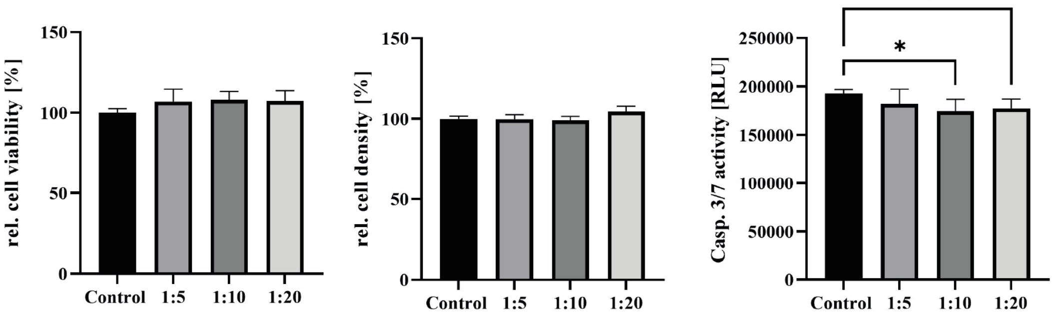

Figure 4.10: Incubation of ocular cells with MgZn 80:20 micropropellers in ratios of 1:5, 1:10, and 1:20 for 48 h. Bar graphs represent the mean values and standard error of mean, n = 8. The experiments were repeated three times with similar results. Statistical differences are indicated as follows: *$p < 0.05$, and ***$p < 0.001$ compared to control, according to one-way ANOVA. Figure taken from[129].

4.3.4 Cargo loading and release

In order to function as carriers for therapeutics the degradable microcarriers need to be temporarily loaded with cargo. This functionalization needs to be stable enough for a time window required to facilitate the transport. The surface of the propellers is oxidized when exposed to air and humidity, forming zinc and magnesium oxides and hydroxides,[146] all of which have very low solubility in water.[123] This effect was increased by air plasma treatment of the particles. This can be exploited to achieve an anchor point, addressable through condensation reactions with ethoxysilane groups. A silane-PEG(5k)-succinimidyl ester (SC) was used to create an attachment point for amine groups via amide bond formation. In this case the cargo molecules were specialized liposomes with integrated surface amino groups and fluorescent CY5 labels, provided by the lab of Prof. Dr. Avi Schroeder (Technion, Israel).

For the functionalization the propellers were air plasma treatment for 5 min at 100 W and 0.4 mbar on the substrate. The substrate was then immersed in a solution of silane-PEG-SC ($5\ \mathrm{mg} \cdot \mathrm{ml}^{-1}$) in a 1:1 ethanol to DI water mixture in a plastic container for at least 30 min. The substrate was rinsed with DI water, immersed in PBS and sonicated shortly to release the propellers. The liposomes were added at a ratio of $10^4 : 1$ and incubated for 2 h. Subsequent washing with PBS by gentle centrifugation (3 times, 3000 rcf, 3 min) removed the excess of liposomes.

The liposome size was measured to be 96 nm by DLS (Z-average) by my collaborators. The fluorescent labels of the liposomes are used for co-localization with the microcarriers. The successful decoration of the helical body with liposomes was demonstrated by enclosing a sample of freshly functionalized MgZn 70:30 microcarriers in a glass chamber, magnetic sedimentation and subsequent imaging of the bottom layer in brightfield and fluorescence channels. A representative overlay of both channels is shown in figure 4.11a, together with inserts showing zoomed-in parts for better visibility.

The sample was then incubated for 24 h and prepared and imaged in the same way as before, shown in figure 4.11b. The expectation of seeing less to no co-localization following the MgZn degradation, leading to liposome release, could be confirmed. After 24 h the fluorescent signal from the liposomes is distributed over the liquid volume in the chamber and not confined to the bottom layer. This is consistent with free floating liposomes in solution. Some liposomes are visible as red agglomerates of larger numbers. However, these show no co-localization with the microcarriers.

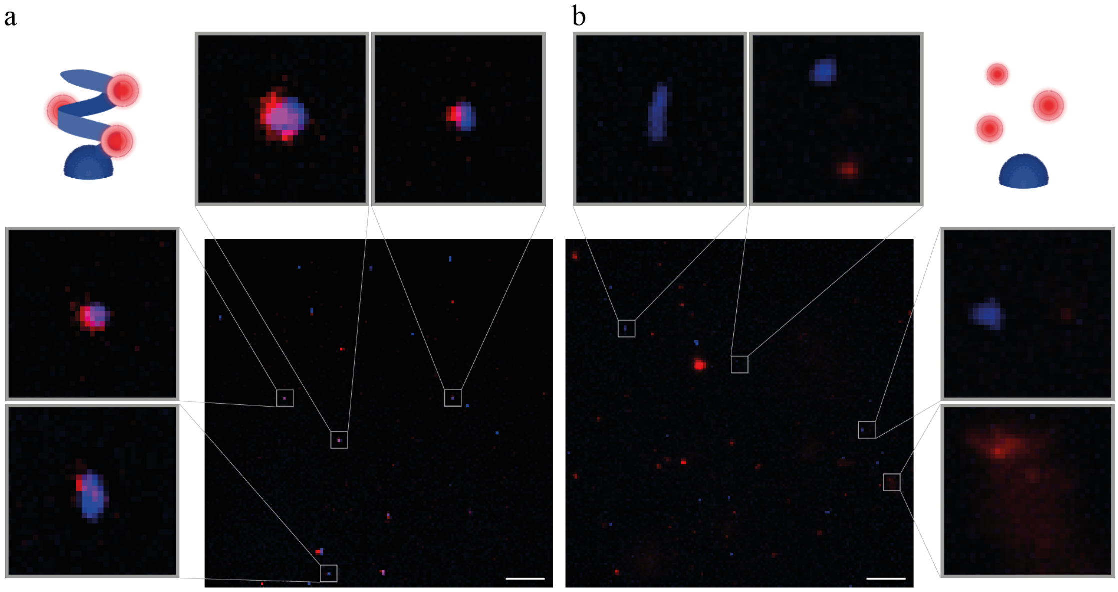

Figure 4.11: Inverted brightfield (blue) and fluorescence (red) image overlays with zoomed-in inserts of MgZn 70:30 micropropellers, imaged after **a** 0 h and **b** 24 h in PBS solution. Scale bars are 25 µm. Figure adapted from[129].

This finding was confirmed by preparing a control sample, prepared in the same way, but without use of silane-PEG-NHS. The resulting overlay image in figure 4.12a shows (almost) no liposomes present. This proves that unspecific, charge-based interactions are not enough to facilitate reliable functionalization.

In an attempt to quantify the liposome release the experiment was repeated for MgZn 80:20 and 70:30 samples. Images in both channels were taken after 0, 2, 6, and 24 h. The number of particles with and without liposomes ($n > 100$) at each time point was counted. The initial functionalization rate was 58 ± 10 % and 36 ± 9 % for MgZn 80:20 and 70:30 respectively. The liposome release is shown relative to the loading at 0 h in figure 4.12b. The MgZn ratio only slightly affects the liposome release rate in the observed range.

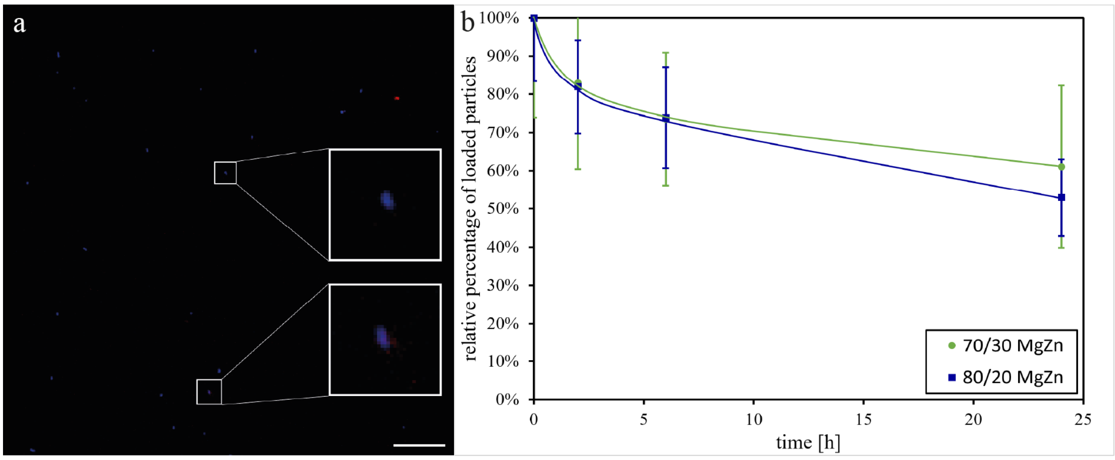

Figure 4.12: **a** Inverted brightfield (blue) and fluorescence (red) image overlay with zoomed-in inserts of MgZn 70:30 micropropellers, without silane-PEG-NHS for active functionalization, on a glass slide. Scale bar is 25 µm. **b** Observation of liposome functionalization over 24 h for MgZn 70:30 and 80:20 (n>100). Solid lines serve as guides to the eye. Figure adapted from[129].

4.3.5 Propulsion

The propulsion behavior of the helically shaped microswimmers, fabricated by GLAD, using FePt was investigated before.[107,121] However, this helix design made of degradable MgZn is different and might alter the propulsion capabilities, especially when loaded with liposomes. With a length of around 1 µm the propellers are large enough to be observed by light microscopy. Custom designed and in-house built 3-axis orthogonal coil pairs were fitted onto the microscope stage of an inverted fluorescence microscope, shown in figure 4.13. With this setup particles can be tracked using brightfield or fluorescence microscopy during actuation.

A sample of MgZn 70:30 microswimmers on a substrate was magnetized perpendicular to the swimming direction, using an electromagnet with a field strength of 1.8 T. The propellers were then dispersed in PBS by sonication for 20 s. In order to observe swimming behaviour without external flows, the swimmers were diluted to a low concentration of $\approx 10^4$ particles per µl and constrained in a chamber with a volume of 25 µl, using a gene frame (10 x 10 x 0.25 mm) and two cover slips. Too high concentrations caused the microswimmers to aggregate over time, which altered the shape and prevented directional movement. Coating the coverslips beforehand with bovine serum albumin prevented adhesion to the glass slides, but resulted in rolling behaviour on the glass surface. Special care was taken to observe swimming in free solution. To operate the coils, an in-house software was used that allows the precise input of voltages, through a 3-channel 10x voltage amplifier. Swimming direction, frequency, time and magnetic field strength can be set by the software. Calibration was performed using a magnetometer with a directional probe, placed in the centre of the chamber. Orientation along a positive axis direction and fitting experimental to theoretical values gave a correction function, dependent on applied voltage and frequency, for each coil pair.

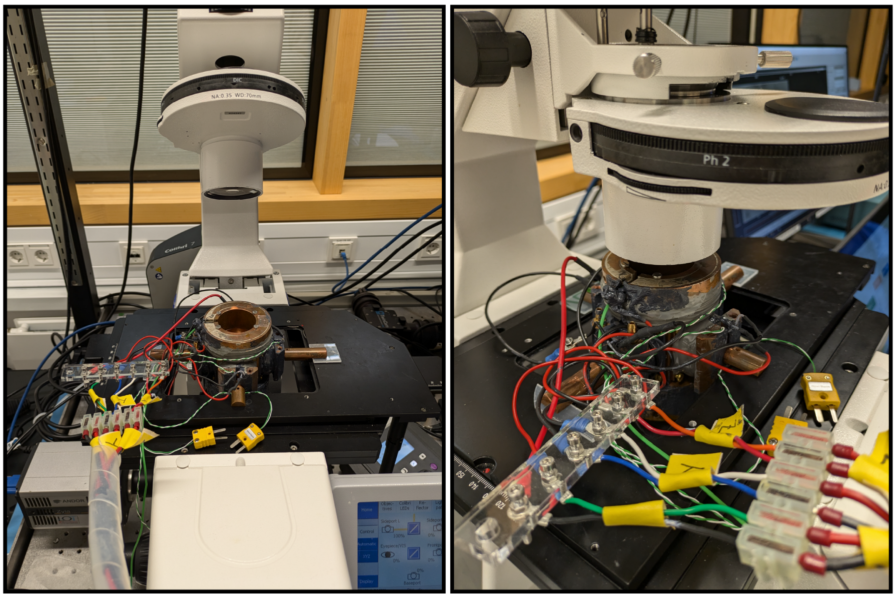

Figure 4.13: 3-axis orthogonal coil pairs inside an inverted fluorescence microscope.

Particle tracking analysis showed a microswimmer following a L-shaped trajectory with a speed of $\approx 10\ \mu\mathrm{m} \cdot \mathrm{s}^{-1}$ using 1 mT field at 100 Hz, which is comparable to conventional, non-degradable designs. After successful loading of helical micropropellers with fluorescent liposomes the propulsion capabilities were tested again. The procedure is similar, but additionally the fluorescent signal of the liposome cargo was tracked consecutively, while switching the light source and adding a suitable filter. Figure 4.14 shows the tracking analysis of propelled particles with liposome cargo in brightfield and fluorescence mode. Tracking analysis measured speeds of $\approx 8\ \mu\mathrm{m} \cdot \mathrm{s}^{-1}$, which is slightly slower than without cargo, but well within the expected range.

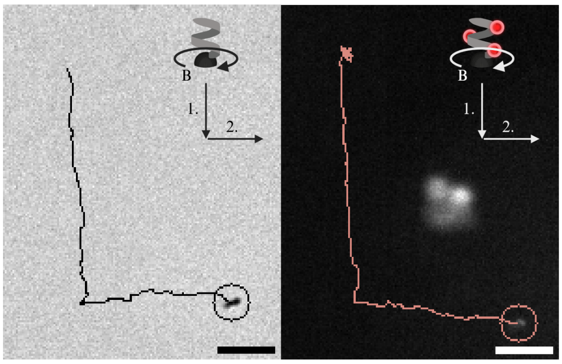

Figure 4.14: Particle tracking analysis of helical MgZn 70:30 microcarriers loaded with fluorescent liposomes on a predetermined L-shaped trajectory. Left: bright-field, right: fluorescent mode. Scale bars are 10 µm. Figure adapted from[129].

For the utilization in therapy, the velocity and steerability of the propellers need to persist over time. To see whether the assembled microcarriers with cargo could be actively propelled for longer times after incubation in an aqueous environment, the experiment was repeated after 28 h in PBS. Figure 4.15 shows propulsion along a manually directed L-shape, observed in fluorescence. While the fluorescence intensity was lower than before, suggesting that some liposomes had already detached from the carriers, the propulsion behavior showed similar speeds and characteristics. It is assumed that one day is long enough to functionalize the micropropellers and perform experiments in potential therapeutic applications.

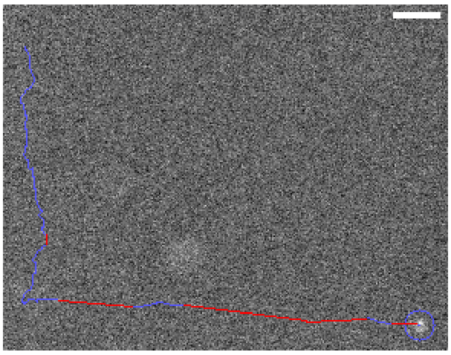

Figure 4.15: Particle tracking analysis of helical MgZn 70:30 microcarriers, loaded with fluorescent liposomes on a predetermined L-shaped trajectory. Scale bar is 10 µm. Figure taken from[129].

4.4 Summary

In this chapter the fabrication of degradable, magnetic, helical microstructures was demonstrated, using GLAD. The growth of structures made of Mg and Zn in ratios of 90:10, 80:20, 70:30, and 50:50 was precisely controllable. Macroscopically predicted corrosion behaviour of Mg and Zn was observed on the microscale, where it was shown that Mg corrodes roughly ten times faster than Zn in DI water. By altering the Mg and Zn content the degradation of the microstructures could be tuned from a few hours to months.

A 16 nm thin layer of biocompatible FePt in its $L1_0$ phase was incorporated into the helical body of the swimmer to enable propulsion through weak external magnetic fields. The measured magnetic moment of $7.4 \cdot 10^{-12}$ emu per propeller with a remanent magnetization of 886 $\text{emu} \cdot \text{cm}^{-3}$ and a coercivity of 1.8 T provides excellent hard magnetic properties, orders of magnitude higher than conventional magnetic materials. Using 3-axis orthogonal coil pairs the microswimmers could be propelled in water, following pre-determined paths, with speeds of $\approx 10\ \mu\text{m} \cdot \text{s}^{-1}$.

The biocompatibility of relatively fast degrading 80:20 MgZn microswimmers was tested on clinically relevant ocular cell lines and primary porcine cells over 48 h, where they showed no toxicity towards the cells, even in extremely high propeller to cell ratios of 20:1. This is of great importance for potential biomedical applications in treating retinal diseases. Towards this goal it could be shown that relevant transfection agents, like liposomes, could be linked through covalent bonds to the microcarriers. The oxidized surface of the microswimmer was decorated using ethoxy silanes with a succinimidyl ester functionality, which in turn forms a peptide bond with the specialized liposome surface. The decoration with liposomes had no significant impact on the propulsion capabilities in terms of speed and steerability. Controlled propulsion with liposomes was still possible after 28 h in water, providing enough time for any future transfection experiments in a clinical setting. The time-dependent degradation of the microswimmer was shown to result in the release of cargo over time, which completes its function as potential carrier systems for targeted drug delivery.

In contrast to previous delivery systems the removal of the microcarriers after delivery is not necessary, since they are almost entirely degradable in aqueous solutions. The shown fabrication and characterization of a degradable magnetic microswimmers system made out of Mg and Zn provides a significant step towards the use of an actively targeted delivery system in a relevant clinical setting. The investigated degradable microcarrier platform shows all the benefits of magnetic delivery systems, while avoiding long-term safety concerns of microparticles in the human body, especially since there are no retrieval strategies available yet for particles of that size. While the impact of a 16 nm biocompatible thin film of FePt is not yet studied in detail, this should allow an attempt at *ex vivo* and *in vivo* studies for the therapy of ocular diseases in larger animal models.

5 Nanomedicine for retinal diseases

5.1 Introduction

To understand the challenges encountered in retinal delivery it is of interest to examine the physiology and diseases of human and animal eyes in detail.

5.1.1 Retinal therapy

The most interesting targets for drug or gene delivery in the eye are photoreceptor cells, neurons, and the retinal pigment epithelium (RPE). These are found in the posterior segment of the eye in the neuroretina, behind a multitude of biological barriers. To circumvent most barriers, current treatment strategies are injections as close as possible to the retina. The two most common options are shown in figure 5.1 and discussed below.

5.1.2 Subretinal injection

Subretinal injection is a recently developed surgical technique performed by injecting a small volume of therapeutics in between the photoreceptor cells and the RPE. This difficult to apply surgical maneuver results in a partial retinal detachment and poses many potential complications, including permanent retina detachment or hole formations.[147] Several administration routes are being developed and tested in clinical trials, but the standard technique involves prior removal of the vitreous body (vitrectomy),[148] which has severe side effects, such as progression of cataract and retinal detachment, and post operative complications.[149] Additionally, the treated area is limited to the immediate surroundings of the injection site. Here, the limited diffusion of therapeutics is accredited to the barrier function of the retina, due to its dense structure.[150] Treatment is often used as a last resort, due to the high risks involved.

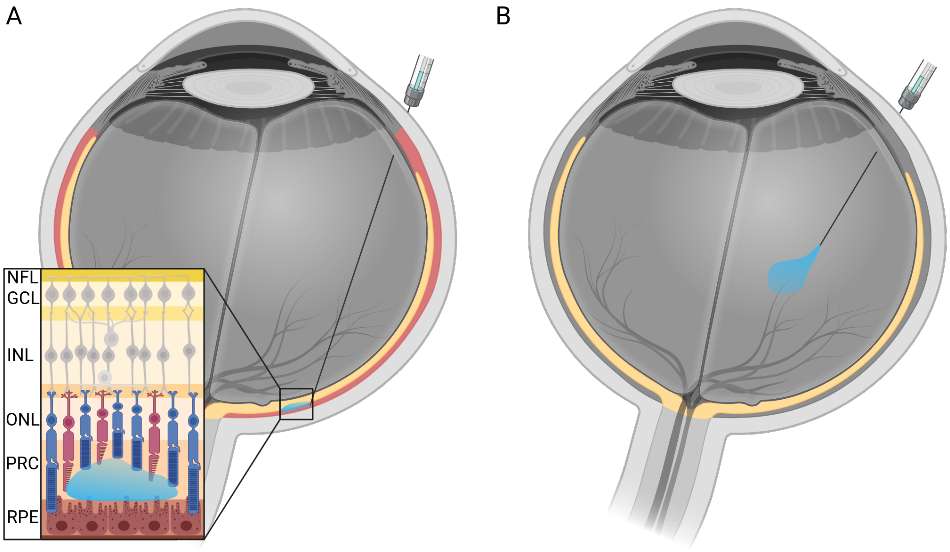

Figure 5.1: Schematic illustration of conventional treatment options for retinal diseases. **A** Subretinal injection of therapeutic containing fluid between the RPE layer and the photoreceptor cell (PRC) layer. **B** Intravitreal injection of the therapeutic into the vitreous body. Created with BioRender.com

5.1.3 Intravitreal injection

Injections into the vitreous body are much less invasive and cause less complications,[151] but have a significantly lower efficiency due to additional barriers between the injected therapeutic and the target cells in the retina. The most significant barriers are the vitreous humour and the inner limiting membrane, which are discussed below.

Vitreous humour

The first barrier after intravitreal injection is the vitreous body itself. The gel-like body with a volume of about 4.5 ml consist mostly of water and a three-dimensional network of collagen fibers and glycosaminoglycans (e.g. hyaluronic acid).[152] The pore size in porcine vitreous is estimated to be 500 nm,[153] in bovine vitreous 550 ± 50 nm.[154] Due to the presence of high amounts of negative charges, positively charged molecules get trapped inside, rendering all positively charged therapeutics ineffective.[155–157] Smaller nanoparticles have been shown to rapidly penetrate the bovine vitreous.[154] Diffusion studies in human vitreous with small fluorescein molecules indicate even higher mobility than for porcine vitreous, making the application in human eyes potentially easier.[152] The large volume of the vitreous poses the first challenge, since injected therapeutics are diluted drastically. Injection of large doses of drugs enhance the risk of triggering an immune response and are thus not an easy circumvention of that problem.[158] Additionally, depending on the injection site, particles have to diffuse over large distances to reach the retina, spreading over the entire vitreous volume.[159,160] Both these aspects could be addressed effectively by an active carrier system. A locally high concentration of therapeutics and genes could be carried directly to the retina, without triggering an immune response. The propulsion of magnetic, helical microswimmers through the porcine vitreous body was demonstrated by our group.[133] In order to overcome the mesh structure of the vitreous the propeller diameter had to be reduced to 500 nm and the surface was coated with perfluorocarbon coating for reduced adhesion. This is a promising approach to facilitate cargo delivery to the retina.

Inner limiting membrane

The second barrier for intravitreal injection is a basment membrane, called the inner limiting membrane (ILM), which separates the vitreous from the retina. For intravitreal injections it is considered the most significant biological barrier. Its thickness increases with age up to 4 µm in humans[161,162], and the main contents are collagen IV, laminin and glycosans.[47,48,163] Together they form a three dimensional mesh of significantly smaller pore size than the vitreous. A precise number is not known yet. Previous studies, mostly performed on rodents, suggest up to 350 nm, but this number strongly varies for different animal species.[164–166] Jackson *et al.* observed the diffusion of fluorescent dextrans of different molecular weights through fixed human retina explants in an Ussing chamber - an apparatus to study diffusion through membranes.[167] They found a size exclusion limit of 76 kDa (Stokes-Einstein radius of $\approx$ 6 nm), while noting that the fixation with paraformaldehyde results in a bias towards smaller pore sizes due to crosslinking. Cryosections of the studied tissues revealed that dextrans of 164 kDa (Stokes-Einstein radius of $\approx$ 7.3 nm) accumulated in the inner plexiform layer, which is posterior to the ganglion cell layer. *In vivo* experiments on cynomolgus monkeys with the commercial drug Bevacizumab (149 kDa, d$\approx$ 7 nm) showed penetration through all retinal layers after intravitreal injection.[168] Viral transduction attempts using adeno-associated viruses, whose capsid is only 22 nm in diameter, also reported very low efficiency in various animal models.[169–174] Non-viral transfection agents were engineered in that size range, by complexing a single DNA molecule with a pegylated CK30 peptide. These compacted DNA nanoparticles can carry larger gene vectors and exhibit sizes of 8 to 45 nm in diameter (minor diameter, as determined by electron microscopy), depending on the gene size and particle shape.[175] The ability of compacted DNA NP to transfect mice and primate retina was demonstrated, but often required subretinal injections to reach target cells in the posterior retina.[176–181] Nevertheless, compacted DNA nanoparticles offer the advantages of non-viral tranfection agents, while having similarly small dimensions than viral vectors, and are hence promising candidates.

Inner limiting membrane removal

A straightforward idea would be to attempt to remove the ILM. Unsurprisingly, the surgical or enzymatic removal of the ILM was shown to increase the transfection efficiency drastically.[169,172,173,182,183] However, surgical removal has to be preceded by a vitrectomy and is therefore unfavorable. Additionally, the surgical procedure is not easy to perform and requires specialized surgeons.

On the other hand, Dalkara *et al.* studied the use of non-specific proteases to degrade the ILM biologically. The treatment lead to a dramatic increase in transduction efficiency by adeno-associated viruses. Unfortunately, high doses were also deleterious to the underlying nerve fibers and ganglion cells. They concluded that the safety margin for intravitreal injection of protease might be too narrow to be used in patients.[169]

The use of micropropellers, functionalized with protease, might help solve this dilemma by reducing the effectively introduced enzyme amount and by localizing it. Guided delivery of an effective dosage might achieve the desired ILM degradation effect, without destroying the underlying retina.

5.1.4 The need for a better model system

The lack of accessibility to suitable model tissue resulted in most (biosafety) studies to be performed on rodents.[108,184] These, however, possess significantly different physiology and gained insights have limited transferability to different species. The current process of designing non-viral vectors for ocular drug delivery is very inefficient, due to a lack of standardized procedures.[185] This leads to a plethora of suggested specialized nanomedicines that fail at the clinical trial stage, because the research is performed on insufficient models that do not hold true when translating to the human eye. In order to progress fundamental research questions need to be answered first. For this reason a focus on appropriate animal models is paramount. The high cost, lack of accessibility and ethical burden of *in vivo* animal studies can be reduced by well-chosen *ex vivo* models. Closer-to-human and readily available are porcine[186] or bovine models.[184] Additionally, retina explant culture is a valuable tool for the study of drug permeability, since the explants can be oriented with the ILM side facing up or down to simulate different

injection routes.[150]
Similarly, Peynshaert *et al.* developed a vitreoretinal explant model for bovine retina, which leaves the vitreous attached. This is beneficial, since vitreous removal is known to disturb the ILM in small areas, leading to potentially biased results.[184] Using this bovine vitreoretinal model, PS nanoparticles of 40 nm size could moderately penetrate the ILM, while 100 nm and 200 nm particles did less so. Removal of the vitreous was shown to allow a comparatively higher intake of 100 nm particles. To display the effect of compromised ILM, they sought out damaged positions on the explant, where a massively increased penetration was observed locally. Unfortunately, due to biological variability, results fluctuate in between different explants and even within different regions on the same explant. Therefore, experimental studies require careful data analysis to produce reliable results.

5.1.5 Magnetic helical microswimmers

Magnetic nano- and microswimmers are promising delivery vehicles for the transport of therapeutics to the retina. They offer guided delivery through the vitreous, thus minimizing off-target side effects, and can overcome slow passive diffusion. Because their propulsion speed is in the order of 1-10 body lengths per second they can only operate in slow fluid flow environments, which can for example be found in the eye. Injections close to the retina are difficult to position. Hence the facilitation of the transport to the back of the eye is already an improvement to conventional techniques. In a proof-of-concept study by our group magnetic helical microswimmers were shown to actively traverse the vitreous body of the eye.[133] To achieve this the microswimmers had to have a filament thickness of maximum 500 nm, small enough to fit through the vitreous gel mesh structure, but big enough to allows strong propulsion and carrying capabilities. Smaller swimmer designs have more dominant rotational diffusion character and are not suitable for propulsion over long distances. Additionally, the surface was coated with a perfluorocarbon liquid that reduced adhesion. Future designs need to include a similar concept to avoid getting trapped inside the vitreous.

5.2 Motivation

This project investigates potential uses of active magnetic microswimmers for retinal therapy. The eye is an ideal environment for active delivery systems, because of its low immune response and the lack of strong fluid flows. Ideally, the transport and release of effective therapeutics to the retina is sufficient to improve or replace conventional surgical approaches, effectively reducing health risks and unwanted side effects, thus improving the patients' quality of life. To probe this, fundamental studies to better understand the penetration capabilities of micro- and nanoparticles into the retinal tissue are necessary. With this knowledge more directed progress in finding efficient drug delivery strategies can be achieved. Additionally, microswimmers could be used for more than the transport to the retina. Mechanical stress exerted locally might help overcome otherwise impermeable biological barriers. If that should not be enough, carrying additional components, such as enzymes, to help facilitate reliable retina penetration is possible, rendering this system a versatile all-round solution.

5.3 Results

Performing experiments on biological tissues, as delicate as the retina, is very complex and challenging. From reading the literature and talking to eye experts it has become clear that reducing the time from the point of death to the experimentation is crucial to preserve the sample physiology. Cooling during transport and handling is essential to slow down cellular degradation processes, which alter the samples' integrity. This imposes a time constraint on performed experiments. Additionally, the tissues need to be handled with extreme care and under physiological salt conditions. Any mechanical stress can lead to ruptures in the thin membranes and cell layers. The best practise we found is to always have the retina tissue lying on a support and otherwise never touch it. These restrictions result in a high susceptibility to errors. On top of that the biological variability makes every sample unique and experimental results have to be viewed critically to avoid misinterpretation. For these reasons the experimentation was partly performed in collaboration. My colleagues Lucie Motyčková and Dr. Mariana Alarcón Correa helped with the tissue preparations. Lucie Motyčková performed the cryosectioning work, while I performed sample staining and imaging with guidance from Dr. Dimitris Missirlis. Discussions, planning and analysis were performed together.

Eye dissection

The fresh porcine eyes were received from a local butcher, where they were kept at 4 °C after enucleation. The eyes were picked-up directly after and transported with cooling to the lab. The estimated time between the animals death and arrival at the lab was 4 h. Next, the remaining outer ocular tissue was removed and the eyes were disinfected in 70 % ethanol, then washed in sterile PBS. A bilateral cut was made by a scalpel and medical scissors above the *ora serrata*, around the iris. The anterior parts were removed and the vitreous body carefully separated, by tilting the eye cup and careful pulling with broad tweezers. This leaves the retina exposed for subsequent experiments.

5.3.1 Mechanical penetration

A straightforward approach to the delivery of therapeutics is the direct delivery via active particles. For this purpose LM fabricated magnetic helical microswimmers made out of SiO_2 with a FePt tail, similar to previous publications,[133] but more biocompatible and with a higher remnant magnetization. We did not use the MgZn microswimmer to reduce the complexity of the study at this stage, but MgZn swimmers can readily be substituted, if needed. In order to observe the propulsion against the ILM and potential penetration into the retina the experiment was performed under an inverted microscope. The 3-axis orthogonal coils were fitted to the microscope stage to enable propulsion in 3D. For better visibility the surface of the propeller was functionalized with Quantum dots@NH_2 (QDot ITK Amino 705) by a silane-PEG-NHS linker. The procedure is similar to the loading protocol described in section 4.3.4. For imaging, a thin sample was necessary to see trough the tissue. Using scissors the eye cup was cut into 3-4 segments after dissection. Each flap was punched by a medical punch (8 mm diameter), which was kept in place to remove the surrounding retina and then carefully removed. The flap was then transferred into a petri dish, filled with neurobasal medium. The interface of RPE to photoreceptor cells is the weakest link, where the retina detaches from the flap and started floating in the medium, where it could be picked up with a spatula spoon. The retina punch was then transferred gently placed inside a chamber, built out of glass cover slips and stacked gene frames. The propellers were magnetized orthogonal to the swimming direction and added on top of the ILM in retina medium. Retina medium is based on neurobasal medium with added N2 and B27 supplements, ciliary neurotrophic factor human (CNTF), Gentamycin and Penicillin/Streptomycin. The exact formulation can be found here.[187] After closing the chamber from the top the sandwich was then flipped upside down and placed inside the magnetic coils. Imaging from below was necessary because of the limited working distance of the 63x objective (NA 0.75) and to allow fluorescence imaging. The propulsion behaviour of the propellers were tested at the bottom of the chamber. Optimal actuation was achieved operating at 10 mT and 100 Hz. The propellers were then navigated upwards until they hit the medium to ILM interface. Once there, they could not swim higher up and started sliding sideways, because the ILM is undulating. until they accumulated in the locally highest plane, shown in figure 5.2.

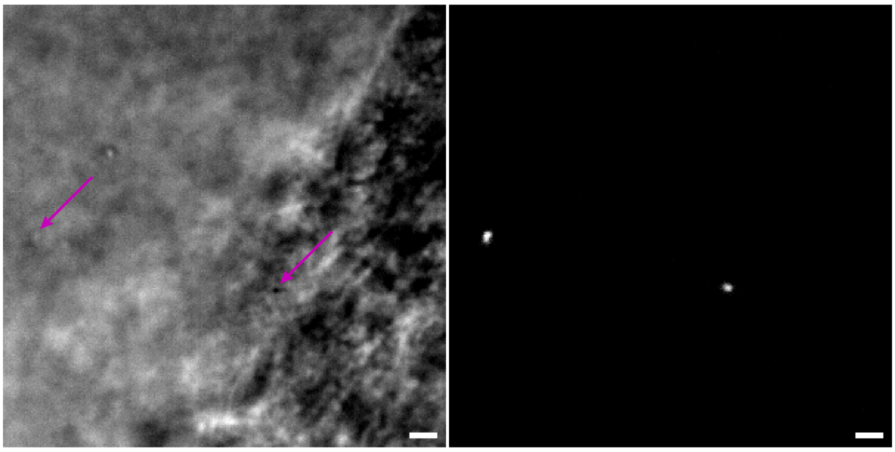

Figure 5.2: Brightfield and fluorescent images of SiO_2@QDot micropropellers at the ILM interface of an porcine retina explant with the ILM side facing down. The interface is not flat, due to the undulating nature of the retina. Scale bars are 5 µm.

The frequency range, in which the propellers can operate depends on the fluid viscosity around it. The viscosity inside the ILM or retina is unknown, but presumably higher than medium. A shift to higher viscosity will require different operating conditions. Further upwards propulsion while varying the frequency between 1 Hz and 100 Hz did not have an observable effect on the propeller penetration capabilities, which suggests the applied force was insufficient to penetrate the ILM. When the propulsion was stopped, the swimmers slowly sedimented towards the bottom of the chamber. We also repeated the experiment from the RPE side, by preparing the sample the other way around. Here, the particles immediately come in contact with RPE cells, without an additional membrane in between. The observed behaviour was indeed different, as the propellers got trapped in the photoreceptor cell layer interface, when propelling upwards. Reorientation or movement in plane was not possible, while being trapped. When the swimming direction was reversed the swimmers broke free again.

The maximum torque that can be applied here depends on the magnetic moment of the swimmer and the applied external magnetic field, according to equation 2.10. The magnetic moment of the swimmer is limited by the remnant magnetization of the used magnetic material and its incorporated volume. In this case the magnetic moment is already very high and can only be marginally increased by using more magnetic material, which is not desirable for later applications. The external magnetic field strength is limited by the coil that produces it. Most lab-scale coil designs reach their limit around 10 mT and a frequency of 100 Hz, while still being small enough to fit inside a microscope stage. Limiting factors are the thickness of the wire and number of turns per coil. These can not be scaled indefinitely, because the dimensions are restricted by the microscope and heating effects must be considered. The achievable torque has been optimised within reasonable constraints.

In order to get a theoretical estimation of the force F a single propeller can exert I compared it to the drag force it overcomes when swimming. This approximation has been made in our group before.[34] By estimating the shape of the propeller as an ellipsoid with the major and minor axes a and b ($a>b$), its Stokes' drag in free solution can be calculated as

$$F_{\text{ell},\infty} = 6\pi\eta b u f_{\text{ell},\infty} \tag{5.1}$$

with a correction factor $f_{\text{ell},\infty}$ and the swimmers' speed u.[188]

$$f_{\text{ell},\infty} = \left\{ \frac{3}{4}\sqrt{\zeta^2 - 1}\left[\left(\zeta^2 + 1\right)\operatorname{arcoth}(\zeta) - \zeta\right]\right\}^{-1} \tag{5.2}$$

$$\zeta = \frac{a}{\sqrt{a^2 - b^2}} = \frac{1}{\sqrt{1 - \frac{1}{A^2}}} \tag{5.3}$$

with the aspect ratio $A \equiv a/b$. Using the dimensions of a typical helical micropropeller as $a = 1.5$ µm and $b = 0.5$ µm results in an aspect ratio of $A = 3$. Using equation 5.2 for this swimmer gives a correction factor of $f_{\text{ell},\infty} \approx 1.4$. With this I can estimate the drag force acting on the microswimmer, swimming at a typical speed of $u = 10$ µm·s^{-1} in water ($\eta = 10^{-3}$ Pa s) using equation 5.1 to

$$F_{\text{ell},\infty} \approx 13 \text{ pN}$$

With this force a microswimmer would exert a pressure of around 100 N·m^{-2}. To put this number into context, atomic force microscopy (AFM) studies can be used to determine stress-strain curves of biological barriers. Candiello *et al.* performed AFM force measurements on the ILM of chicks, lying on a stiff substrate.[46] Loading force over indentation plots show no rupture of the membrane at 10 nN of loading force at an indentation depth of 50 nm. With their used AFM tip radius of 10 nm the exerted pressure calculates to $\approx 10^7$ N $\cdot$ m^{-2}. Somewhat related cell membrane and rehydrated lipid bilayer penetration force measurements were shown to require a force of 5-27 nN,[189] which resulted in pressures of $\approx 10^5 - 10^7\ \mathrm{N \cdot m^{-2}}$, depending on the used tip geometry and size. These numbers suggest that the exerted force by this microswimmer is orders of magnitude too low to penetrate the ILM and other biological membranes.

5.3.2 Retina penetration by nanoparticles

From the literature we know that particles of smaller size show higher permeability, but have low efficiencies due to their dependence on slow diffusion, dilution in the vitreous and dependence on local injections. Magnetic helical propellers could be used to transport smaller, nanosized particles to the retina, which can not propel themselves. However, since the exact size limit of particles, capable of ILM penetration, is unknown, determining it would immensely benefit the search for suitable non-viral vectors. From the few reliable studies the size limit can be estimated to be below 100 nm, likely even below 50 nm, if penetration by larger numbers is required. The research of my colleague Lucie Motyčková is focused on performing systematic studies to find the size limit of spherical particles, capable of ILM penetration.

Enzymatic ILM digestion

To complement this line of research, I investigated the possibility of increasing the ILM permeability through enzymatic degradation of its structural collagen fibers. To this extent, two different collagenases from *Clostridium histolyticum* were used to achieve proteolytic activity. Collagenases are proteases of the matrix metalloproteinase family, capable of collagen fibre cleavage in basement membranes.[190] Collagenase type IV (Cls IV, Merck) is capable of cleaving network-forming collagen IV chains[191,192], while collagenase type II (Cls II, Merck) is cleaving long collagen I fibrils. Both enzymes were blended by the manufacturer with clostripain, an arginin protease. Compared to the previously studied, unspecific protease blend Pronase E,[169] which catalyzes the cleavage of proteins down to single amino acids, the herein used collagenases are more specific, which should result in less off-target activity.

In order to observe the effect of enzyme digestion on the ILM permeability, fluorescent PS nanoparticles of 25 nm diameter (micromer-redF, carboxyl modified surface, micromod Partikeltechnologie) were applied to the retina. From our observations during shared preliminary experiments, we suspect that the addition of a particle dispersion on top of retina explants in culture does not prevent the particles from diffusing into the medium and around the explanted tissue. Diffusion of small particles into the retina from the torn off photoreceptor cell side should be more easily possible, since there is no biological barrier to prevent penetration into the damaged tissue. Performing penetration experiments, where particles can diffuse from both sides lead to biased results and confusion and should be avoided. The extraction of a larger section of retina is unfortunately not possible, due to the fragile nature of the tissue. Therefore, we developed an *ex vivo* retina-choroid-sclera model system. The model can be cut into larger sections and keeps the structural assembly of layers intact. The eye was prepared as described in section 5.3 and then cut in 2-3 pieces. Each piece was then pinned on a styrofoam plate with needles to keep the partial eye cups from collapsing, shown in figure 5.3. The cups were filled with physiological salt buffer solution (Hank's balanced salt solution, HBSS) to keep the tissue alive.

Figure 5.3: A retina-choroid-sclera explant pinned on a styrofoam square.

This model did prevent diffusion around the tissue, but could not be cultured for more than a few hours. Experiments with free enzymes in different amounts were performed to study the degradation process and show the effect of ILM degradation on the permeability of retina towards 25 nm PS particles. According to the manufacturer the enzyme activity was 125-250 Mandl-U per mg. Enzyme formulations of 0, 50 and 100 µg were applied over 1 h in HBSS with added Ca^{2+} at 37 °C. The Ca^{2+} ions are a necessary co-factor for collagenase. After washing with HBSS, the *ex vivo* retina-choroid-sclera model was incubated with 25 nm PS@COOH beads ($\approx 10^{13}$ particles) for 1 h at 37 °C. After incubation the retina was rinsed with HBSS to remove excess particles and the exposed area was excised, fixed with methanol and embedded in TissueTek O.C.T. medium (Sakura Finetek) in an aluminum mold. Homogeneous freezing was achieved by placing the mold on a raft, built out of aluminum, floating on liquid nitrogen. The frozen tissue was cut into 10 µm thick slices and transferred to adhesive glass slides (SuperFrost PLUS, Epredia). The cryosections were dried, washed with tris-buffered saline, stained with DAPI and imaged using a fluorescence microscope under consistent imaging conditions. 3-channel images were taken using a 10x air objective (NA 0.45) in brightfield with phase contrast and two fluorescence channels for DAPI and the red PS particles with suitable filters. The red fluorescence microscopy images were post-processed to differentiate the particle signal from the underlying autofluorescence of the tissue by subtracting an offset value, determined from a control sample. Figure 5.4A shows stitched together zoom-in images of phase contrast brightfield images and overlayed fluorescence channels. DAPI is displayed in gray, while the red fluorescence signal from the particles is shown as a gradient from yellow to blue with decreasing intensity, normalized to the image with the highest intensity (Cls II, 100 µg). Cell layers are labelled for orientation. The control sample shows a low concentration of particles on the ILM with no apparent penetration into the tissue. Rinsing the sample before imaging removed the bulk of particles. The enzyme treated samples show a significant higher amount of retained particles at the interface due to surface penetration into the ILM an underlying tissue. Cls II treated samples show a higher penetration depth of PS particles deep into the GCL, but also show damage to the surface layers, which appear to be disturbed. A higher enzyme dose increase the ILM permeability further with particles reaching the ONL, but also had increasing deleterious effects on the surface retina layers.

The region of degradation due to the enzymes in the higher dose reach down all the way to the INL, causing structural rearrangement and resulting in the dislocation of cell bodies. For Cls II the damage is more severe, with complete structural loss to the GCL, forming holes in the tissue, which can be seen by the increased thickness of the GCL.

When observing the control sample with a high magnification 63x oil objective (NA 1.4) in brightfield and fluorescence, shown in figure 5.4B, the PS particles do appear to penetrate the retina slightly. This level of detail was not possible to observe with a low magnification objective, which is hence unsuitable for a detailed analysis and can only be used to observe larger clusters of particles. The observed low penetration depth of only a few micrometers might be a result of the short incubation time of only 1 h, given they are diffusion dependent and therefore slow. To test this the experiment should be repeated with longer incubation times of 24 h or more. However, increasing the time also causes natural degradation due to the decaying tissue and so complicates such an analysis. Unfortunately this *ex vivo* retina-choroid-sclera model system is not suited for cell culture. Alternative model systems would have to be developed.

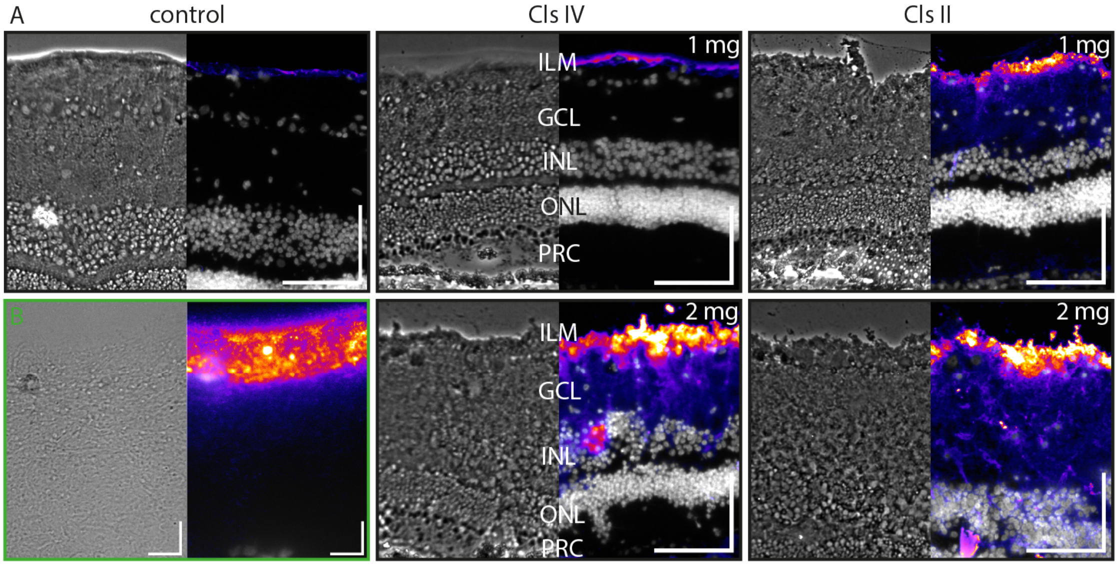

Figure 5.4: **A** Low magnification fluorescence microscopy image zoom-ins of an *ex vivo* porcine retina-choroid-sclera model after incubation with **a** 0 µg, **b** 50 µg, and **c** 100 µg of Cls II and IV, followed by incubation with 25 nm fluorescent PS@COOH beads. Each incubation period was performed for 1 h in HBSS with Ca^{2+} at 37 °C. Left: Phase contrast brightfield images. Right: Overlay of fluorescence channels, DAPI staining in grey and PS particles colored in a gradient from yellow to blue with decreasing intensity. Fluorescence has been offset using a negative control to remove autofluorescence and normalized to the highest fluorescence (Cls II, 100 µg). Retinal layers from top to bottom: ILM=inner limiting membrane, GCL=ganglion cell layer, INL=inner nuclear layer, ONL=outer nuclear layer, PRC=photoreceptor cells. Scale bars are 100 µm. **B** High magnification fluorescence microscopy image zoom-ins of the same position, shown in brightfield on the left and fluorescence on the right (same color code, with offset, not normalized) Scale bars are 10 µm.

Additionally, the enzyme concentration has to be adjusted to prevent damage to the underlying tissue, while still achieving higher ILM permeability. Cls IV seems to be milder and more specific and therefore a more promising candidate. Alternative enzyme blends without additional enzymes, like clostrapain, could also be tested to reduce unspecific activity. In order to allow a detailed observation of the ILM degradation, immunostaining against collagen would be insightful. Staining with rabbid anti-collagen IV antibodies was attempted, following the literature procedure, but did not show good localization to the ILM. The reason for this is still unknown and remains to be investigated.

High-resolution electron microscopy analysis

In collaboration with the research group of Prof. Dr. Rasmus Schröder (BioQuant, Heidelberg) the effects of enzyme degradation on the ILM and retina was investigated by high-resolution electron microscopy. Retina explants were treated with 40 µg of Cls II for 1 h at 37 °C in retina medium, then subjected to a fixation, dehydration and resin embedding procedure, followed by sectioning in an ultramicrotome (slive thickness of about 70 nm) and sequential imaging by Munisa Tabarova. Exemplary images are shown in figure 5.5.

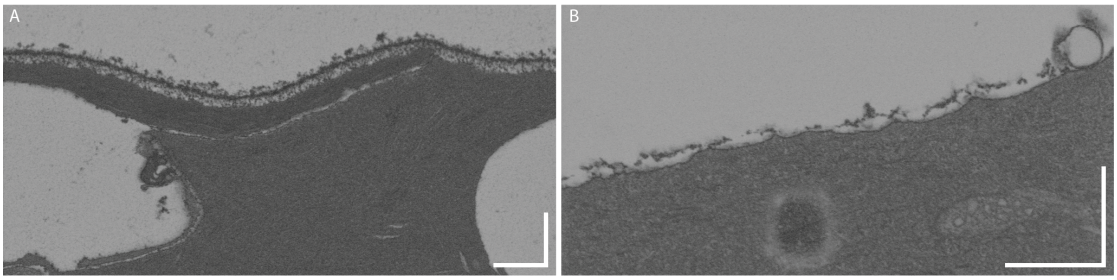

Figure 5.5: Electron microscopy images of fixed and resin embedded retina explant explant ultramicrotome sections, incubated with **A** 0 µg or **B** 40 µg Cls II in retina medium for 1 h at 37 °C. Scale bars are 500 nm. Provided by the lab of Prof. Dr. R. Schröder.

As shown in the electron microscopy images the ILM is entirely intact in the observed areas of the untreated retina explants. The ILM is visible as a $\approx$ 140 nm thick membrane with three layers, a more electron-dense core and more fibrous, transparent outside layers, on top of the Müller cell endfeet. This three alyer structure is also found in human fetal ILM.[193,194] The thickness measured in a dehydrated sample is always smaller than its hydrated natural form.[45] Incubation of the ILM with Cls II partially degraded the ILM structure and produced holes of around 50 nm diameter. In these images no damage to the underlying tissue could be observed, which might be due to the lower concentration used in this experiment. This is a promising results, as it shows that proteolytic activity does not necessarily need to cause deleterious effects, although a more extensive analysis is necessary to determine the best operating conditions.

Condensed DNA nanoparticles

Alternatively, the use and potential transport of a non-viral transfection agents was investigated. In order to find a suitable cargo molecule that could benefit from delivery via MgZn microcarriers, I survey the literature for the smallest possible non-viral gene delivery vectors available. The highest form of condensation is reported for nanoparticles formed around a single strand of DNA, complexed with oligopeptides CK_{30} with attached PEG (10 kDa) chain, first shown by Liu *et al.* to transfect postmitotic cells.[175] Since then these compacted DNA nanoparticles (DNA NPs) have also been successfully used to transfect ocular cells in mice[176–179,195–197] and non-human primates[180] by intravitreal and subretinal injections. The efficiency of these nanoparticles is likely due to their extremely small dimensions, depending on the used DNA size. Number-weighted DLS measurements show hydrodynamic diameters of 34, 78, and 100 nm for plasmid sizes of 2.89, 5.14, and 28 kb respectively.[175] Their surface charge is neutral, which allows them to diffuse freely in the vitreous body[154] and penetrate membranes, including the nuclear membrane.[175] Three years later it was shown through electron microscopy analysis that, depending on the counter ion, the DNA NPs assume different shapes. The use of trifluoroacetate (TFA) produces an ellipsoidal shape, while the use of acetate (Ac) results in long wires.[198] This is of interest, since an elongated shape features a minor and a major diameter, which might allow penetration of particles along a specific orientation. The minor diameters of such particles can be as low as 8 nm, which is significantly lower than their measured hydrodynamic radius. It would therefore be of interest to see if the transport and release of such small non-viral vectors with degradable magnetic microcarriers can improve their efficiency. To this extent I have fabricated DNA NPs with an eGFP plasmid (≈3 kb). The oligopeptides (Intavis Peptide Services, Tübingen) and the eGFP plasmid were provided by the Schnichels lab (Center of Opthalmology, University Eye Hospital Tübingen). The formation of condensed DNA nanoparticles was performed according to the literature[175,199] by step wise addition of CK30PEG(10k)@acetate to eGFP plasmid in a 2:1 charge ratio (3.1:1 w/w ratio) with vigorous mixing in between additions. Complexation for 30 min at 20 °C was followed by 3 washing steps, using Amicon Ultra 100 kDa centrifugal filters (Merck) to remove excess peptide. The DNA NPs were recovered in water and stored at 4 °C until use. I measured the hydrodynamic radius by DLS to 49±21 nm (average of six measurements, number-weighted), which is in agreement with the literature value of 60±6 nm.[199]

To test the transfection efficiency of DNA NPs towards ocular cells the Schnichels lab (Center of Opthalmology, University Eye Hospital Tübingen) performed transfection experiments on cultured porcine retina explants. The reporter gene luciferase, cloned into a plasmid, was complexed with CK30PEG(10k) for both counterions (TFA and Ac) and incubated for 48 h on top of retina explants. After successful transfection Luciferase enzyme activity emits green light as a readout, when adding its substrate luciferin. The fluorescence images captured after histological analysis, shown in figure 5.6, exhibit low autofluorescence at the ILM interface and in the photoreceptor cell layer for the control sample with naked plasmid. For the samples incubated with DNA NPs green fluorescence is recorded throughout all retinal layers. The localization is different for each DNA NP type. DNA NPs@TFA seems to have a higher permeability, but the cells in the INL and ONL are disturbed. This might be a result of the preparation procedure or a negative side effect of the DNA NPs and needs to be examined further. This experiment provides preliminary confirmation that intravitreal delivery is a promising delivery route for these particles.

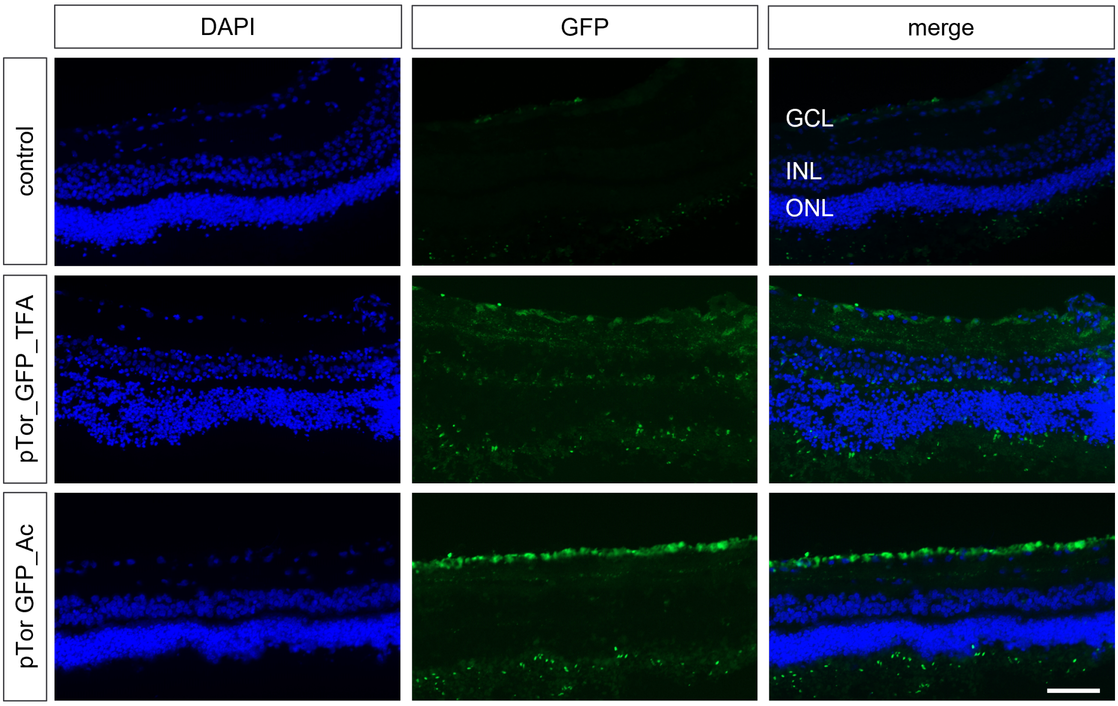

Figure 5.6: Histological analysis of transfection experiments on porcine retina explants over 48 h with DNA NPs with different counterions, complexed with a plasmid encoding for the reporter gene luciferase. Cells were stained with DAPI. Luciferase activity emits green light. Fluorescence channels are shown separately and as overlay. Scale bar is 100 µm. Provided by the lab of Dr. Sven Schnichels.

In order to load the DNA NPs onto MgZn microcarriers for future transport to the retina, I performed the same silane linking procedure, as shown previously in section 4.3.4. For fluorescent labelling of DNA NPs, propidium iodide solution in a final concentration of 1 µg·ml^{-1} was added and incubated for 5 min, before performing microscopy in a confined volume. Images were taken in quick succession in brightfield and fluorescence mode (cyan LED of 511/44 nm and 20 % intensity with long-pass filter of 555/25 nm). Fluorescence images were processed using imageJ, by applying a threshold that cuts off the background signal, measured on an unstained sample of MgZn@DNA NP propellers with identical imaging settings, and converted the images to binary form. Brightfield images were background subtracted (rolling ball radius: 3 pixels, sliding paraboloid enabled), inverted and also converted to a binary image using the threshold function. The resulting channels, shown in figure 5.7, were compared using an 'AND' filter, which yields a binary image with bright pixels, where both channels showed a signal. The fluorescently positive particles were counted (n=1297) and divided by the total particle count (n=7689) from the brightfield images, which yielded a particle functionalization ratio of 16.9±0.2 %.

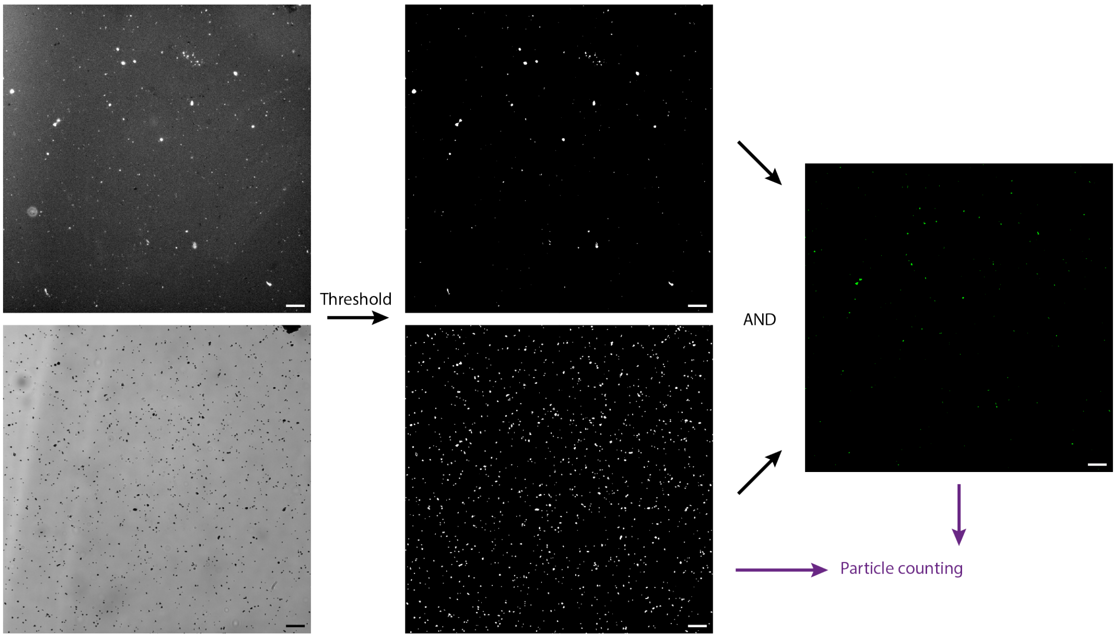

Figure 5.7: Particle functionalization analysis of MgZn@DNA NPs, imaged in brightfield and fluorescent mode. Brightfield images were background subtracted, then both channels were converted by a threshold algorithm into binary images and subjected to an 'AND' filter. The resulting image shows only the overlapping signal from both channels. Scale bars are 20 µm.

5.4 Summary

In this chapter the potential use of magnetically guided microcarriers for drug delivery to the retina was investigated. The key challenges have been identified as overcoming the barrier roles of vitreous body and ILM, which make the retinal tissue impermeable to many intravitreally injected viral and non-viral vectors alike. The penetration capabilities of nanoparticles are restricted to neutral and negative charges and are size-dependent, while a precise size cut-off is so far unknown. Studies have to be performed in a relevant animal model to allow translation of the results to human physiology. To this extent, pigs have been identified as a suitable model system, where these challenges were addressed in preliminary experiments.

Firstly, the mechanical penetration of the ILM was studied using magnetic helical microswimmers and a lab-scale three-axis coil system. The exerted force of a single microswimmer against the surface of the retina from the ILM side by propulsion was estimated to 100 $\mathrm{N \cdot m^{-2}}$ and shown to be insufficient to achieve penetration. Comparison with reported AFM force measurement studies revealed that the achieved pressure is likely orders of magnitude too low in this configuration.

Secondly, the use of enzymatic degradation of the ILM by proteases was investigated in an attempt to increase its permeability for nanoparticles. An *ex vivo* porcine retina-choroid-sclera model was developed to study the penetration of nanoparticles in a controlled manner. In a preliminary study, I showed that collagenases are promising candidates for ILM degradation. Application of free enzymes in different doses increased the penetration capabilities of 25 nm PS particles significantly. While the applied doses were too high and caused substantial damage to the underlying tissue, a lower dose in combination with more realistic incubation times should reduce unwanted off-target activity. This approach could be combined with degradable MgZn microswimmers, which should be capable of transporting enzymes in locally active quantities.

Thirdly, the transport of non-viral, gene-loaded vectors to the retina was identified as a promising strategy to overcome the limitations of intravitreal injection by active and guided transport. To this extent, a literature survey yielded compacted DNA nanoparticles as promising candidates. Their retina transfection capabilities are documented in the literature and were validated in an *ex vivo* retina model by our collaborators (Schnichels lab). I was able to show the binding of these nanoparticles onto degradable MgZn microcarriers for future targeted delivery experiments. While the initial loading rate was only around 17 %, the procedure can likely be optimised to at least 40 %, which is similar to the rate achieved for liposomes.

6 Conclusions and Outlook

This thesis examined different ways to achieve propulsion and carry molecular cargo in aqueous environments in the low Reynolds number regime. I specifically focused on using biological building blocks or inorganic materials that are degradable in biological environments to improve the biocompatibility of active nano- and microstructures. This directly addresses concerns towards the long-term safety such structures when used in the human body. Especially for small particles, where there are no retrieval strategies available yet, the biosafety is of upmost importance.

By combining catalytically active platinum nanoparticles with a biological scaffold, made out of DNA helices, an attempt was made to realize an active bio-hybrid structure. While an efficient coupling scheme could be developed, and activity could be shown, the shape of the structure did not exhibit significant active motion. The small size of the construct limited the size of the chemical gradient for self-propulsion and complicated the observation. However, the assembly procedure is flexible due to the versatility of DNA and can be applied to build larger systems that could exhibit interesting functionalities through catalytical activity.

Alternative to chemical propulsion the use of rotating magnetic fields is a promising strategy to achieve actively guided motion, especially over larger distances and in biological media. Helical microswimmers are an interesting design concept, whose main drawback is the need for inorganic materials for its fabrication and magnetic properties. To address this issue the fabrication of a degradable microswimmer was achieved by using magnesium and zinc as structural materials. Adjusting the magnesium to zinc ratio produces a flexible system that can be programmed to degrade in a time span ranging from hours to months. This provides enough time to perform delivery tasks in medical experiments, while at the same time allows the release of therapeutics over a designated time. The results presented in this thesis overcome a major limitation of magnetic delivery systems and should allow the progression towards biomedical application inside more realistic environments and clinical studies, which brings us another step closer to the envisioned 'nanosurgeon'.[200]

Figure 6.1: Envisioned micro-submarine carrying a surgeon for targeted nanomedicine

The eye poses an ideal target organ for the use of degradable magnetic microcarriers, because it promises potential improvement over the currently employed, risky and inefficient surgical techniques. These shortcomings mean that gene therapy is currently limited in the eye and only under major surgical procedures. In contrast to desirable micro- and nanoparticle based preventive therapies, which would drastically increase the prospect of success and the patients quality of life. To achieve this goal, the herein reported progress in a degradable delivery system can be used to address the key challenges faced in ocular therapy. While the transport of magnetic helical microswimmers through the vitreous body has been shown before, the identification and loading of an efficient therapeutic agent still had to be demonstrated. Here I confirmed the fabrication and showed the loading of compacted DNA nanoparticles as promising candidates onto degradable microcarriers.
Outside of the eye, potential applications for magnetic microcarriers can be found inside other fluid containing organs, such as the bladder or stomach, as long as the fluid flow is reasonably low. Progress towards the capability to traverse fast flowing environments or compact tissues would require optimisation and improvement of the propulsion mechanism. If the target site imposes no size restriction, potentially larger designs can be fabricated that might be capable of exhibiting stronger forces and faster swimming speeds. The combination of magnetic and other propulsion strategies, for example ultrasound, might offer capabilities not achievable with either method alone.

Acknowledgements

My deepest gratitude goes to Prof. Dr. Peer Fischer for his endless support, patience and uplifting fascination with and dedication to science. I can't remember a day when he didn't find time for his students, even for late night owls like me. A true inspiration to all of us, both scientifically and as a person. The infamous year-end rewind presentations, late night political talks and last-minute presentation sessions will always be fond memories.
I would also like to express my sincere gratitude to my colleague and close friend Dr. Mariana Alarcón Correa, who took it upon herself to supervise and guide me throughout my entire PhD. Thank you for always keeping a door open for me. I am not sure where my health would be without our venting sessions and shared critical analysis of the - not always just scientific - world.
To the love of my life, Emily Seibert, I owe a debt of gratitude that is hard to put into words. You expand my world, help me push my limits and fill my life with joy and purpose. I have no idea where I would be without you and I intent to never find out.
To my parents, who made it possible for me to study and write this thesis, I am eternally grateful for your endless support, even if the paths I choose don't always make sense to you. I am who I am because of you and I thank you for that every day.
I also want to thank Dr. Holger Seibert, who is a constant source of inspiration and who I look up to in life. Thank you for showing me a side of the world I never knew and encouraging me to reach higher than I ever dreamed possible. I will always treasure our culinary adventures, ski vacations and sailing escapades.
Additional thanks goes to Nico Segreto and Maximilian Gairing, for introducing me to the world of metal music and all the wonders it holds. The many hours of pure joy and distraction from the stressful aspects of my work I owe to you - with hopefully many more to come.
A special thanks goes to my brother, Michael Peter, who never stopped believing in me. It helped more than you will ever know.
I would like to thank Prof. Dr. Christine Selhuber-Unkel, Prof. Dr. Eva Blasco and Prof. Dr. Rasmus Schröder for agreeing to evaluate this work.

To all my colleagues and friends, unfortunately too many to mention directly, but important all the same: Thank you for providing an always interesting, stimulating and friendly environment at work and outside of it. I have learned a lot and it was a pleasure to work alongside all of you. I have certainly learned a lot about different cultures and people and it helped me grow. A special mention to the closest people around me: Lucie Motyčková, Dr. Vincent Mauricio Kadiri, Dr. Jan-Philipp Günther, Ruben Renkert, Sai Nikhilesh Murty Kottapalli, Dr. Dimitris Missirlis, Dr. Oscar Demeulenaere, Dr. Ellen Rumley, Naomi Tashiro and Målin Schmidt.

I want to specifically highlight Rahul Goyal for his tireless work on the magnetic coils and the selfless support in late night propulsion experiments.

Additionally, I want to thank Julian Martus and his family for providing me with much needed coffee breaks, discussions over dinner and a place to sleep in the initial stages of my move to Heidelberg.

I also want to thank Jutta Heß for her support and advice.

Bibliography

(1) Elgeti, J.; Winkler, R. G.; Gompper, G. *Reports on Progress in Physics* **2015**, *78*, 056601.

(2) Howard, J.; Hudspeth, A. J.; Vale, R. D. *Nature* **1989**, *342*, 154–158.

(3) Mehta, A. D.; Rock, R. S.; Rief, M.; Spudich, J. A.; Mooseker, M. S.; Cheney, R. E. *Nature* **1999**, *400*, 590–593.

(4) Chen, J.-X.; Chen, Y.-G.; Kapral, R. *Advanced Science* **2018**, *5*, 1800028.

(5) Howse, J. R.; Jones, R. A. L.; Ryan, A. J.; Gough, T.; Vafabakhsh, R.; Golestanian, R. *Physical Review Letters* **2007**, *99*, 048102.

(6) Ke, H.; Ye, S.; Carroll, R. L.; Showalter, K. *The Journal of Physical Chemistry A* **2010**, *114*, 5462–5467.

(7) Ebbens, S. J.; Howse, J. R. *Langmuir* **2011**, *27*, 12293–12296.

(8) *E. coli in Motion*; Berg, H. C., Ed.; Biological and Medical Physics, Biomedical Engineering; Springer: New York, NY, 2004.

(9) Tinkle, S.; McNeil, S. E.; Mühlebach, S.; Bawa, R.; Borchard, G.; Barenholz, Y. (; Tamarkin, L.; Desai, N. *Annals of the New York Academy of Sciences* **2014**, *1313*, 35–56.

(10) Hanany, M.; Rivolta, C.; Sharon, D. *Proceedings of the National Academy of Sciences of the United States of America* **2020**, *117*, 2710–2716.

(11) Wong, W. L.; Su, X.; Li, X.; Cheung, C. M. G.; Klein, R.; Cheng, C.-Y.; Wong, T. Y. *The Lancet Global Health* **2014**, *2*, e106–e116.

(12) Yau, J. W. et al. *Diabetes Care* **2012**, *35*, 556–564.

(13) Gilbert, C.; Foster, A. *Bulletin of the World Health Organization* **2001**, *79*, 227–232.

(14) Yorston, David *Community Eye Health* **2003**, *16*, 19.

(15) Fusco, S.; Ullrich, F.; Pokki, J.; Chatzipirpiridis, G.; Özkale, B.; Sivaraman, K. M.; Ergeneman, O.; Pané, S.; Nelson, B. J. *Expert Opinion on Drug Delivery* **2014**, *11*, 1815–1826.

(16) Seeman, N. C. *Journal of Theoretical Biology* **1982**, *99*, 237–247.

(17) Rothemund, P. W. K. *Nature* **2006**, *440*, 297–302.

(18) Douglas, S. M.; Dietz, H.; Liedl, T.; Högberg, B.; Graf, F.; Shih, W. M. *Nature* **2009**, *459*, 414–418.

(19) Watson, J. D.; Crick, F. H. C. *Nature* **1953**, *171*, 737–738.

(20) CaDNAno `http://cadnano.org/welcome` (accessed 09/24/2024).

(21) Einstein, A. *Annalen der Physik* **1905**, *vol. 4, t. 17*.

(22) Von Smoluchowski, M. **1906**, DOI: `10.1002/andp.19063261405`.

(23) Sutherland, W. *The London, Edinburgh, and Dublin Philosophical Magazine and Journal of Science* **1905**, *9*, 781–785.

(24) Costigliola, L.; Heyes, D. M.; Schrøder, T. B.; Dyre, J. C. *The Journal of Chemical Physics* **2019**, *150*, 021101.

(25) Einstein, A. *Annalen der Physik* **1906**, *324*, 371–381.

(26) Kapral, R. *The Journal of Chemical Physics* **2013**, *138*, 020901.

(27) Purcell, E. M. *American Journal of Physics* **1977**, *45*, 3–11.

(28) Trombley, C. I.; Ekiel-Jeżewska, M. L. In *Flowing Matter*, Toschi, F., Sega, M., Eds.; Springer International Publishing: Cham, 2019, pp 35–50.

(29) Golestanian, R.; Liverpool, T. B.; Ajdari, A. *Physical Review Letters* **2005**, *94*, 220801.

(30) Anderson, J. *Annual Review of Fluid Mechanics* **1989**, *21*, 61–99.

(31) Ebbens, S.; Tu, M.-H.; Howse, J. R.; Golestanian, R. *Physical Review E* **2012**, *85*, 020401.

(32) In *E. coli in Motion*, Berg, H. C., Ed.; Springer: New York, NY, 2004, pp 105–120.

(33) Peyer, K. E.; Zhang, L.; Nelson, B. J. *Nanoscale* **2013**, *5*, 1259–1272.

(34) Ghosh, A.; Fischer, P. *Nano Letters* **2009**, *9*, 2243–2245.

(35) Hawkeye, M. M.; Taschuk, M. T.; Brett, M. J., *Glancing Angle Deposition of Thin Films: Engineering the Nanoscale*, 2014.

(36) Sauerbrey, G. *Zeitschrift für Physik* **1959**, *155*, 206–222.

(37) Powell, A.; Minson, P.; Trapaga, G.; Pal, U. *Metallurgical and Materials Transactions A* **2001**, *32*, 1959–1966.

(38) Tait, R. N.; Smy, T.; Brett, M. J. *Thin Solid Films* **1993**, *226*, 196–201.

(39) Robbie, K.; Sit, J. C.; Brett, M. J. *Journal of Vacuum Science & Technology B: Microelectronics and Nanometer Structures Processing, Measurement, and Phenomena* **1998**, *16*, 1115–1122.

(40) London, A.; Benhar, I.; Schwartz, M. *Nature Reviews Neurology* **2013**, *9*, 44–53.

(41) Kolb, Helga; Nelson, Ralph; Fernandez, Eduardo; Jones, Bryan The Organization of the Retina and Visual System `https://webvision.med.utah.edu/` (accessed 10/03/2024).

(42) Cholkar, K.; Dasari, S. R.; Pal, D.; Mitra, A. K. In *Ocular Transporters and Receptors*, Mitra, A. K., Ed.; Woodhead Publishing Series in Biomedicine; Woodhead Publishing: 2013, pp 1–36.

(43) Olsen, T. W.; Edelhauser, H. F.; Lim, J. I.; Geroski, D. H. *Investigative Ophthalmology & Visual Science* **1995**, *36*, 1893–1903.

(44) Miao, H.; Wu, B.-D.; Tao, Y.; Li, X.-X. *Acta Ophthalmologica* **2013**, *91*, e1–e6.

(45) Peynshaert, K.; Devoldere, J.; Minnaert, A.-K.; De Smedt, S. C.; Remaut, K. *Current Eye Research* **2019**, *44*, 465–475.

(46) Candiello, J.; Balasubramani, M.; Schreiber, E. M.; Cole, G. J.; Mayer, U.; Halfter, W.; Lin, H. *The FEBS Journal* **2007**, *274*, 2897–2908.

(47) Martin, G. R.; Timpl, R.; Kühn, K. In *Advances in Protein Chemistry*, Anfinsen, C. B., Edsall, J. T., Richards, F. M., Eisenberg, D. S., Eds.; Academic Press: 1988; Vol. 39, pp 1–50.

(48) Candiello, J.; Cole, G. J.; Halfter, W. *Matrix Biology* **2010**, *29*, 402–410.

(49) Guduric-Fuchs, J.; Ringland, L. J.; Gu, P.; Dellett, M.; Archer, D. B.; Cogliati, T. *Molecular Vision* **2009**, *15*, 1915–1928.

(50) Sanchez, I.; Martin, R.; Ussa, F.; Fernandez-Bueno, I. *Graefe's Archive for Clinical and Experimental Ophthalmology* **2011**, *249*, 475–482.

(51) Choi, K.-E.; Anh, V. T. Q.; Oh, J.-H.; Yun, C.; Kim, S.-W. *Translational Vision Science & Technology* **2021**, *10*, 3.

(52) McMenamin, P. G.; Steptoe, R. J. *Journal of Anatomy* **1991**, *178*, 65–77.

(53) Olsen, T. W.; Sanderson, S.; Feng, X.; Hubbard, W. C. *Investigative Ophthalmology & Visual Science* **2002**, *43*, 2529–2532.

(54) Ruiz-Ederra, J.; García, M.; Hicks, D.; Vecino, E. *Molecular Vision* **2004**, *10*, 83–92.

(55) Garcá, M.; Ruiz-Ederra, J.; Hernández-Barbáchano, H.; Vecino, E. *Journal of Comparative Neurology* **2005**, *486*, 361–372.

(56) Chandler; Smith; Samuelson; Mackay *Veterinary Ophthalmology* **1999**, *2*, 179–184.

(57) De Schaepdrijver, L.; Simoens, P.; Pollet, L.; Lauwers, H.; De Laey, J.-J. *Experimental Eye Research* **1992**, *54*, 975–985.

(58) Kiel, J. W. In *The Ocular Circulation*; Morgan & Claypool Life Sciences: 2010.

(59) Simoens, P.; De Schaepdrijver, L.; Lauwers, H. *Experimental Eye Research* **1992**, *54*, 965–973.

(60) De Schaepdrijver, L.; Lauwers, H.; Simoens, P.; Geest, J. P. d. *Anatomia, Histologia, Embryologia* **1990**, *19*, 222–235.

(61) Warfvinge, K.; Kiilgaard, J. F.; Klassen, H.; Zamiri, P.; Scherfig, E.; Streilein, W.; Prause, J. U.; Young, M. J. *Cell Transplantation* **2006**, *15*, 603–612.

(62) Mathieu, F.; Liao, S.; Kopatsch, J.; Wang, T.; Mao, C.; Seeman, N. C. *Nano Letters* **2005**, *5*, 661–665.

(63) Alarcón-Correa, M.; Kilwing, L.; Peter, F.; Liedl, T.; Fischer, P. *ChemPhysChem* **2023**, *24*, e202300294.

(64) Melzer, M. S. *Biochimica et Biophysica Acta (BBA) - Nucleic Acids and Protein Synthesis* **1967**, *142*, 538–541.

(65) Rhaese, H.-J.; Freese, E. *Biochimica et Biophysica Acta (BBA) - Nucleic Acids and Protein Synthesis* **1968**, *155*, 476–490.

(66) Massie, H. R.; Samis, H. V.; Baird, M. B. *Biochimica et Biophysica Acta (BBA) - Nucleic Acids and Protein Synthesis* **1972**, *272*, 539–548.

(67) Imlay, J. A.; Chin, S. M.; Linn, S. *Science* **1988**, *240*, 640–642.

(68) Mouret, J. .-.; Polverelli, M.; Sarrazini, F.; Cadet, J. *Chemico-Biological Interactions* **1991**, *77*, 187–201.

(69) Derjaguin, B. V.; Churaev, N. V.; Muller, V. M. In *Surface Forces*, Derjaguin, B. V., Churaev, N. V., Muller, V. M., Eds.; Springer US: Boston, MA, 1987, pp 293–310.

(70) Kuzyk, A.; Schreiber, R.; Fan, Z.; Pardatscher, G.; Roller, E.-M.; Högele, A.; Simmel, F. C.; Govorov, A. O.; Liedl, T. *Nature* **2012**, *483*, 311–314.

(71) Fu, X.; Wang, Y.; Wu, N.; Gui, L.; Tang, Y. *Journal of Colloid and Interface Science* **2001**, *243*, 326–330.

(72) Tu, W.; Takai, K.; Fukui, K.-i.; Miyazaki, A.; Enoki, T. *The Journal of Physical Chemistry B* **2003**, *107*, 10134–10140.

(73) Pensa, E.; Cortés, E.; Corthey, G.; Carro, P.; Vericat, C.; Fonticelli, M. H.; Benítez, G.; Rubert, A. A.; Salvarezza, R. C. *Accounts of Chemical Research* **2012**, *45*, 1183–1192.

(74) Chen, G. *Computational and Theoretical Chemistry* **2021**, *1195*, 113094.

(75) Dablemont, C.; Lang, P.; Mangeney, C.; Piquemal, J.-Y.; Petkov, V.; Herbst, F.; Viau, G. *Langmuir* **2008**, *24*, 5832–5841.

(76) Gür, F. N.; Schwarz, F. W.; Ye, J.; Diez, S.; Schmidt, T. L. *ACS Nano* **2016**, *10*, 5374–5382.

(77) Bhatt, N.; Huang, P.-J. J.; Dave, N.; Liu, J. *Langmuir* **2011**, *27*, 6132–6137.

(78) Borzenkov, M.; Chirico, G.; D'Alfonso, L.; Sironi, L.; Collini, M.; Cabrini, E.; Dacarro, G.; Milanese, C.; Pallavicini, P.; Taglietti, A.; Bernhard, C.; Denat, F. *Langmuir* **2015**, *31*, 8081–8091.

(79) Aye, T. T.; Low, T. Y.; Sze, S. K. *Analytical Chemistry* **2005**, *77*, 5814–5822.

(80) Dasog, M.; Scott, R. W. J. *Langmuir* **2007**, *23*, 3381–3387.

(81) Sbalzarini, I. F.; Koumoutsakos, P. *Journal of Structural Biology* **2005**, *151*, 182–195.

(82) Gregory, D. A.; Ebbens, S. J. *Langmuir* **2018**, *34*, Publisher: American Chemical Society, 4307–4313.

(83) Dutta, S.; Noh, S.; Gual, R. S.; Chen, X.; Pané, S.; Nelson, B. J.; Choi, H. *Nano-Micro Letters* **2023**, *16*, 41.

(84) Villa, K.; Pumera, M. *Chemical Society Reviews* **2019**, *48*, 4966–4978.

(85) Wang, W.; Castro, L. A.; Hoyos, M.; Mallouk, T. E. *ACS Nano* **2012**, *6*, 6122–6132.

(86) Xu, T.; Gao, W.; Xu, L.-P.; Zhang, X.; Wang, S. *Advanced Materials* **2017**, *29*, 1603250.

(87) Schenck, J. F. *Journal of Magnetic Resonance Imaging* **2000**, *12*, 2–19.

(88) Schamel, D.; Mark, A. G.; Gibbs, J. G.; Miksch, C.; Morozov, K. I.; Leshansky, A. M.; Fischer, P. *ACS Nano* **2014**, *8*, 8794–8801.

(89) Wang, X.; Qin, X.-H.; Hu, C.; Terzopoulou, A.; Chen, X.-Z.; Huang, T.-Y.; Maniura-Weber, K.; Pané, S.; Nelson, B. J. *Advanced Functional Materials* **2018**, *28*, 1804107.

(90) Ceylan, H.; Yasa, I. C.; Yasa, O.; Tabak, A. F.; Giltinan, J.; Sitti, M. *ACS Nano* **2019**, *13*, 3353–3362.

(91) Chattopadhyay, S.; Dash, S. K.; Tripathy, S.; Das, B.; Mandal, D.; Pramanik, P.; Roy, S. *Chemico-Biological Interactions* **2015**, *226*, 58–71.

(92) Wu, Y.; Kong, L. *Environmental Geochemistry and Health* **2020**, *42*, 2277–2286.

(93) Lewinski, N.; Colvin, V.; Drezek, R. *Small* **2008**, *4*, 26–49.

(94) Mahmoudi, M.; Hofmann, H.; Rothen-Rutishauser, B.; Petri-Fink, A. *Chemical Reviews* **2012**, *112*, 2323–2338.

(95) Arias, L. S.; Pessan, J. P.; Vieira, A. P. M.; Lima, T. M. T. d.; Delbem, A. C. B.; Monteiro, D. R. *Antibiotics* **2018**, *7*, 46.

(96) Malhotra, N.; Lee, J.-S.; Liman, R. A. D.; Ruallo, J. M. S.; Villaflores, O. B.; Ger, T.-R.; Hsiao, C.-D. *Molecules* **2020**, *25*, 3159.

(97) Singh, N.; Jenkins, G. J.; Asadi, R.; Doak, S. H. *Nano Reviews* **2010**, *1*, 5358.

(98) Son, K.; Ryu, G.; Jeong, H.-H.; Fink, L.; Merz, M.; Nagel, P.; Schuppler, S.; Richter, G.; Goering, E.; Schütz, G. *Small* **2019**, *15*, 1902353.

(99) Shi, Y.; Lin, M.; Jiang, X.; Liang, S. *Journal of Nanomaterials* **2015**, *2015*, e467873.

(100) Lérida-Viso, A.; Estepa-Fernández, A.; García-Fernández, A.; Martí-Centelles, V.; Martínez-Máñez, R. *Advanced Drug Delivery Reviews* **2023**, *201*, 115049.

(101) Ramachandran, R. V.; Barman, A.; Modak, P.; Bhat, R.; Ghosh, A.; Saini, D. K. *Biomaterials Advances* **2022**, *140*, 213048.

(102) Chen, Q.; Wang, N.; Zhu, M.; Lu, J.; Zhong, H.; Xue, X.; Guo, S.; Li, M.; Wei, X.; Tao, Y.; Yin, H. *Redox Biology* **2018**, *15*, 266–276.

(103) Higbee-Dempsey, E. M.; Amirshaghaghi, A.; Case, M. J.; Bouché, M.; Kim, J.; Cormode, D. P.; Tsourkas, A. *Journal of the American Chemical Society* **2020**, *142*, 7783–7794.

(104) Yan, X.; Zhou, Q.; Vincent, M.; Deng, Y.; Yu, J.; Xu, J.; Xu, T.; Tang, T.; Bian, L.; Wang, Y.-X. J.; Kostarelos, K.; Zhang, L. *Science Robotics* **2017**, *2*, eaaq1155.

(105) Noh, S.; Jeon, S.; Kim, E.; Oh, U.; Park, D.; Park, S. H.; Kim, S. W.; Pané, S.; Nelson, B. J.; Kim, J.-y.; Choi, H. *Small* **2022**, *18*, 2107888.

(106) Ussia, M.; Urso, M.; Kratochvilova, M.; Navratil, J.; Balvan, J.; Mayorga-Martinez, C. C.; Vyskocil, J.; Masarik, M.; Pumera, M. *Small* **2023**, *19*, 2208259.

(107) Kadiri, V. M.; Günther, J.-P.; Kottapalli, S. N.; Goyal, R.; Peter, F.; Alarcón-Correa, M.; Son, K.; Barad, H.-N.; Börsch, M.; Fischer, P. *The European Physical Journal E* **2021**, *44*, 74.

(108) Hosseinpour, S.; Walsh, L. J.; Xu, C. *Journal of Materials Chemistry B* **2020**, *8*, 9863–9876.

(109) Kabir, H.; Munir, K.; Wen, C.; Li, Y. *Bioactive Materials* **2021**, *6*, 836–879.

(110) Prasadh, S.; Raguraman, S.; Wong, R.; Gupta, M. *Metals* **2022**, *12*, 999.

(111) Brar, H. S.; Platt, M. O.; Sarntinoranont, M.; Martin, P. I.; Manuel, M. V. *JOM* **2009**, *61*, 31–34.

(112) Bowen, P. K.; Shearier, E. R.; Zhao, S.; Guillory II, R. J.; Zhao, F.; Goldman, J.; Drelich, J. W. *Advanced Healthcare Materials* **2016**, *5*, 1121–1140.

(113) Venezuela, J. J. D.; Johnston, S.; Dargusch, M. S. *Advanced Healthcare Materials* **2019**, *8*, 1900408.

(114) Liu, X.; Sun, J.; Yang, Y.; Pu, Z.; Zheng, Y. *Materials Letters* **2015**, *161*, 53–56.

(115) Seitz, J.-M.; Wulf, E.; Freytag, P.; Bormann, D.; Bach, F.-W. *Advanced Engineering Materials* **2010**, *12*, 1099–1105.

(116) Martinez, D. C.; Dobkowska, A.; Marek, R.; Ćwieka, H.; Jaroszewicz, J.; Płociński, T.; Donik, Č.; Helmholz, H.; Luthringer-Feyerabend, B.; Zeller-Plumhoff, B.; Willumeit-Römer, R.; Święszkowski, W. *Bioactive Materials* **2023**, *28*, 132–154.

(117) Wang, C.; Yu, Z.; Cui, Y.; Zhang, Y.; Yu, S.; Qu, G.; Gong, H. *Journal of Materials Science & Technology* **2016**, *32*, 925–929.

(118) Müller, W. D.; Nascimento, M. L.; Zeddies, M.; Córsico, M.; Gassa, L. M.; Mele, M. A. F. L. d. *Materials Research* **2007**, *10*, 5–10.

(119) Liu, C.; Xin, Y.; Tian, X.; Chu, P. K. *Journal of Materials Research* **2007**, *22*, 1806–1814.

(120) Lévesque, J.; Hermawan, H.; Dubé, D.; Mantovani, D. *Acta Biomaterialia* **2008**, *4*, 284–295.

(121) Kadiri, V. M.; Bussi, C.; Holle, A. W.; Son, K.; Kwon, H.; Schütz, G.; Gutierrez, M. G.; Fischer, P. *Advanced Materials* **2020**, *32*, 2001114.

(122) Kurt J. Lesker Company `https://de.lesker.com/newweb/deposition_materials/materialdepositionchart.cfm?pgid=0#z` (accessed 10/09/2024).

(123) GESTIS Stoffdatenbank, Gefahrstoffinformationssystem der Deutschen Gesetzlichen Unfallversicherung `https://gestis.dguv.de/` (accessed 11/12/2023).

(124) Amaral, L. F.; Oliveira, I. R.; Salomão, R.; Frollini, E.; Pandolfelli, V. C. *Ceramics International* **2010**, *36*, 1047–1054.

(125) Xu, Z.; Eduok, U.; Szpunar, J. *Surface and Coatings Technology* **2019**, *357*, 691–697.

(126) Cimatu, K. A.; Mahurin, S. M.; Meyer, K. A.; Shaw, R. *The Journal of Physical Chemistry C* **2012**, *116*, 10405–10414.

(127) Kadiri, Vincent Mauricio Active Biohybrid Nanostructures For Biomedical Applications, Ph.D. Thesis, Universität Stuttgart, 2021.

(128) Celestin, M.; Krishnan, S.; Bhansali, S.; Stefanakos, E.; Goswami, D. Y. *Nano Research* **2014**, *7*, 589–625.

(129) Peter, F.; Kadiri, V. M.; Goyal, R.; Hurst, J.; Schnichels, S.; Avital, A.; Sela, M.; Mora-Raimundo, P.; Schroeder, A.; Alarcón-Correa, M.; Fischer, P. *Advanced Functional Materials* **2024**, *34*, 2314265.

(130) Walker, D.; Kübler, M.; Morozov, K. I.; Fischer, P.; Leshansky, A. M. *Nano Letters* **2015**, *15*, 4412–4416.

(131) Yu, M.; Ohguchi, H.; Zambano, A.; Takeuchi, I.; Liu, J. P.; Josell, D.; Bendersky, L. A. *Materials Science and Engineering: B* **2007**, *142*, 139–143.

(132) Chang, H.-C.; Wang, L.-C. A Simple Proof of Thue's Theorem on Circle Packing, 2010.

(133) Wu, Z.; Troll, J.; Jeong, H.-H.; Wei, Q.; Stang, M.; Ziemssen, F.; Wang, Z.; Dong, M.; Schnichels, S.; Qiu, T.; Fischer, P. *Science Advances* **2018**, *4*, eaat4388.

(134) Gonzalez, J.; Hou, R. Q.; Nidadavolu, E. P. S.; Willumeit-Römer, R.; Feyerabend, F. *Bioactive Materials* **2018**, *3*, 174–185.

(135) Zheng, Y. F.; Gu, X. N.; Witte, F. *Materials Science and Engineering: R: Reports* **2014**, *77*, 1–34.

(136) Liu, L.; Gebresellasie, K.; Collins, B.; Zhang, H.; Xu, Z.; Sankar, J.; Lee, Y.-C.; Yun, Y. *Applied Sciences* **2018**, *8*, 1459.

(137) Chen, Y.; Zhang, W.; Maitz, M. F.; Chen, M.; Zhang, H.; Mao, J.; Zhao, Y.; Huang, N.; Wan, G. *Corrosion Science* **2016**, *111*, 541–555.

(138) Cheng, J.; Liu, B.; Wu, Y. H.; Zheng, Y. F. *Journal of Materials Science & Technology* **2013**, *29*, 619–627.

(139) Törne, K.; Larsson, M.; Norlin, A.; Weissenrieder, J. *Journal of Biomedical Materials Research Part B: Applied Biomaterials* **2016**, *104*, 1141–1151.

(140) Shang, T.; Wang, K.; Zhang, L.; Zhou, L.; Liu, L.; Liu, C.; Zhang, H.; Li, X.; Zhao, Y.; Wang, J. *Journal of Science: Advanced Materials and Devices* **2023**, 100590.

(141) Grün, N. G.; Holweg, P.; Tangl, S.; Eichler, J.; Berger, L.; van den Beucken, J. J. J. P.; Löffler, J. F.; Klestil, T.; Weinberg, A. M. *Acta Biomaterialia* **2018**, *78*, 378–386.

(142) Meng, Y.; Liu, L.; Zhang, D.; Dong, C.; Yan, Y.; Volinsky, A. A.; Wang, L.-N. *Bioactive Materials* **2019**, *4*, 87–96.

(143) Chen, D.; He, Y.; Tao, H.; Zhang, Y.; Jiang, Y.; Zhang, X.; Zhang, S. *International Journal of Molecular Medicine* **2011**, *28*, 343–348.

(144) Zberg, B.; Uggowitzer, P. J.; Löffler, J. F. *Nature Materials* **2009**, *8*, 887–891.

(145) Cihova, M.; Martinelli, E.; Schmutz, P.; Myrissa, A.; Schäublin, R.; Weinberg, A. M.; Uggowitzer, P. J.; Löffler, J. F. *Acta Biomaterialia* **2019**, *100*, 398–414.

(146) Trino, L. D.; Dias, L. F. G.; Albano, L. G. S.; Bronze-Uhle, E. S.; Rangel, E. C.; Graeff, C. F. O.; Lisboa-Filho, P. N. *Ceramics International* **2018**, *44*, 4000–4008.

(147) Irigoyen, C.; Amenabar Alonso, A.; Sanchez-Molina, J.; Rodríguez-Hidalgo, M.; Lara-López, A.; Ruiz-Ederra, J. *Journal of Clinical Medicine* **2022**, *11*, 4717.

(148) Tripepi, D.; Jalil, A.; Ally, N.; Buzzi, M.; Moussa, G.; Rothschild, P.-R.; Rossi, T.; Ferrara, M.; Romano, M. R. *International Journal of Molecular Sciences* **2023**, *24*, 10535.

(149) Recchia, F. M.; Scott, I. U.; Brown, G. C.; Brown, M. M.; Ho, A. C.; Ip, M. S. *Ophthalmology* **2010**, *117*, 1851–1857.

(150) Peynshaert, K.; Devoldere, J.; De Smedt, S. C.; Remaut, K. *Advanced Drug Delivery Reviews* **2018**, *126*, 44–57.

(151) Ghasemi Falavarjani, K.; Nguyen, Q. D. *Eye* **2013**, *27*, 787–794.

(152) Shafaie, S.; Hutter, V.; Brown, M. B.; Cook, M. T.; Chau, D. Y. S. *International Journal of Pharmaceutics* **2018**, *550*, 207–215.

(153) Qiu, T.; Schamel, D.; Mark, A. G.; Fischer, P. In *2014 IEEE International Conference on Robotics and Automation (ICRA)*, 2014 IEEE International Conference on Robotics and Automation (ICRA), 2014, pp 3801–3806.

(154) Xu, Q.; Boylan, N. J.; Suk, J. S.; Wang, Y.-Y.; Nance, E. A.; Yang, J.-C.; McDonnell, P. J.; Cone, R. A.; Duh, E. J.; Hanes, J. *Journal of Controlled Release* **2013**, *167*, 76–84.

(155) Pitkänen, L.; Ruponen, M.; Nieminen, J.; Urtti, A. *Pharmaceutical Research* **2003**, *20*, 576–583.

(156) Martens, T. F.; Vercauteren, D.; Forier, K.; Deschout, H.; Remaut, K.; Paesen, R.; Ameloot, M.; Engbersen, J. F.; Demeester, J.; De Smedt, S. C.; Braeckmans, K. *Nanomedicine* **2013**, *8*, 1955–1968.

(157) Kim, H.; Robinson, S. B.; Csaky, K. G. *Pharmaceutical Research* **2009**, *26*, 329–337.

(158) Reichel, F. F.; Peters, T.; Wilhelm, B.; Biel, M.; Ueffing, M.; Wissinger, B.; Bartz-Schmidt, K. U.; Klein, R.; Michalakis, S.; Fischer, M. D.; for the RD-CURE Consortium *Investigative Ophthalmology & Visual Science* **2018**, *59*, 1910–1915.

(159) Friedrich, S.; Cheng, Y.-L.; Saville, B. *Current Eye Research* **1997**, *16*, 663–669.

(160) Ross, M.; Ofri, R. *Neural Regeneration Research* **2021**, *16*, 1751–1759.

(161) Henrich, P. B.; Monnier, C. A.; Halfter, W.; Haritoglou, C.; Strauss, R. W.; Lim, R. Y. H.; Loparic, M. *Investigative Ophthalmology & Visual Science* **2012**, *53*, 2561–2570.

(162) Halfter, W.; Oertle, P.; Monnier, C. A.; Camenzind, L.; Reyes-Lua, M.; Hu, H.; Candiello, J.; Labilloy, A.; Balasubramani, M.; Henrich, P. B.; Plodinec, M. *The FEBS Journal* **2015**, *282*, 4466–4479.

(163) Halfter, W.; Dong, S.; Dong, A.; Eller, A. W.; Nischt, R. *Eye* **2008**, *22*, 1207–1213.

(164) Koo, H.; Moon, H.; Han, H.; Na, J. H.; Huh, M. S.; Park, J. H.; Woo, S. J.; Park, K. H.; Chan Kwon, I.; Kim, K.; Kim, H. *Biomaterials* **2012**, *33*, 3485–3493.

(165) Sakurai, E.; Ozeki, H.; Kunou, N.; Ogura, Y. *Ophthalmic Research* **2000**, *33*, 31–36.

(166) Bourges, J.-L.; Gautier, S. E.; Delie, F.; Bejjani, R. A.; Jeanny, J.-C.; Gurny, R.; BenEzra, D.; Behar-Cohen, F. F. *Investigative Ophthalmology & Visual Science* **2003**, *44*, 3562–3569.

(167) Jackson, T. L.; Antcliff, R. J.; Hillenkamp, J.; Marshall, J. *Investigative Ophthalmology & Visual Science* **2003**, *44*, 2141–2146.

(168) Heiduschka, P.; Fietz, H.; Hofmeister, S.; Schultheiss, S.; Mack, A. F.; Peters, S.; Ziemssen, F.; Niggemann, B.; Julien, S.; Bartz-Schmidt, K. U.; Schraermeyer, U.; and The Tübingen Bevacizumab Study Group *Investigative Ophthalmology & Visual Science* **2007**, *48*, 2814–2823.

(169) Dalkara, D.; Kolstad, K. D.; Caporale, N.; Visel, M.; Klimczak, R. R.; Schaffer, D. V.; Flannery, J. G. *Molecular Therapy* **2009**, *17*, 2096–2102.

(170) Yin, L.; Greenberg, K.; Hunter, J. J.; Dalkara, D.; Kolstad, K. D.; Masella, B. D.; Wolfe, R.; Visel, M.; Stone, D.; Libby, R. T.; DiLoreto Jr, D.; Schaffer, D.; Flannery, J.; Williams, D. R.; Merigan, W. H. *Investigative Ophthalmology & Visual Science* **2011**, *52*, 2775–2783.

(171) Cehajic-Kapetanovic, J.; Milosavljevic, N.; Bedford, R. A.; Lucas, R. J.; Bishop, P. N. *Molecular Therapy Methods & Clinical Development* **2018**, *9*, 192–202.

(172) Takahashi, K.; Igarashi, T.; Miyake, K.; Kobayashi, M.; Yaguchi, C.; Iijima, O.; Yamazaki, Y.; Katakai, Y.; Miyake, N.; Kameya, S.; Shimada, T.; Takahashi, H.; Okada, T. *Molecular Therapy* **2017**, *25*, 296–302.

(173) Teo, K. Y. C.; Lee, S. Y.; Barathi, A. V.; Tun, S. B. B.; Tan, L.; Constable, I. J. *Investigative Ophthalmology & Visual Science* **2018**, *59*, 3574–3583.

(174) Gonçalves, M. A. *Virology Journal* **2005**, *2*, 43.

(175) Liu, G.; Li, D.; Pasumarthy, M. K.; Kowalczyk, T. H.; Gedeon, C. R.; Hyatt, S. L.; Payne, J. M.; Miller, T. J.; Brunovskis, P.; Fink, T. L.; Muhammad, O.; Moen, R. C.; Hanson, R. W.; Cooper, M. J. *Journal of Biological Chemistry* **2003**, *278*, 32578–32586.

(176) Farjo, R.; Skaggs, J.; Quiambao, A. B.; Cooper, M. J.; Naash, M. I. *PLOS ONE* **2006**, *1*, e38.

(177) Cai, X.; Conley, S. M.; Nash, Z.; Fliesler, S. J.; Cooper, M. J.; Naash, M. I. *The FASEB Journal* **2010**, *24*, 1178–1191.

(178) Han, Z.; Conley, S. M.; Makkia, R. S.; Cooper, M. J.; Naash, M. I. *The Journal of Clinical Investigation* **2012**, *122*, 3221–3226.

(179) Han, Z.; Banworth, M. J.; Makkia, R.; Conley, S. M.; Al-Ubaidi, M. R.; Cooper, M. J.; Naash, M. I. *The FASEB Journal* **2015**, *29*, 2535–2544.

(180) Kelley, R. A.; Conley, S. M.; Makkia, R.; Watson, J. N.; Han, Z.; Cooper, M. J.; Naash, M. I. *International Journal of Nanomedicine* **2018**, *13*, 1361–1379.

(181) Zheng, M.; Mitra, R. N.; Weiss, E. R.; Han, Z. *Molecular Therapy* **2020**, *28*, 523–535.

(182) Kolstad, K. D.; Dalkara, D.; Guerin, K.; Visel, M.; Hoffmann, N.; Schaffer, D. V.; Flannery, J. G. *Human Gene Therapy* **2010**, *21*, 571–578.

(183) Vacca, O.; Darche, M.; Schaffer, D. V.; Flannery, J. G.; Sahel, J.-A.; Rendon, A.; Dalkara, D. *Glia* **2014**, *62*, 468–476.

(184) Peynshaert, K.; Devoldere, J.; Forster, V.; Picaud, S.; Vanhove, C.; De Smedt, S. C.; Remaut, K. *Drug Delivery* **2017**, *24*, 1384–1394.

(185) Peynshaert, K.; Devoldere, J.; De Smedt, S.; Remaut, K. *Expert Opinion on Drug Delivery* **2023**, *20*, 259–271.

(186) Schnichels, S.; Paquet-Durand, F.; Löscher, M.; Tsai, T.; Hurst, J.; Joachim, S. C.; Klettner, A. *Progress in Retinal and Eye Research* **2021**, *81*, 100880.

(187) Fietz, A.; Hurst, J.; Joachim, S. C.; Schnichels, S. *STAR Protocols* **2023**, *4*, 102443.

(188) Verrelli, D. I. *International Journal of Multiphase Flow* **2014**, *65*, 138–142.

(189) Angle, M. R.; Wang, A.; Thomas, A.; Schaefer, A. T.; Melosh, N. A. *Biophysical Journal* **2014**, *107*, 2091–2100.

(190) Krane, S. M. *Amino Acids* **2008**, *35*, 703–710.

(191) Huhtala, P.; Chow, L. T.; Tryggvason, K. *Journal of Biological Chemistry* **1990**, *265*, 11077–11082.

(192) Gordon, M. K.; Hahn, R. A. *Cell and Tissue Research* **2010**, *339*, 247–257.

(193) Heegaard, S. *Acta ophthalmologica Scandinavica Supplement* **1997**, 1–31.

(194) Halfter, W.; Sebag, J.; Cunningham, E. T. In *Vitreous: in Health and Disease*, Sebag, J., Ed.; Springer: New York, NY, 2014, pp 165–191.

(195) Cai, X.; Nash, Z.; Conley, S. M.; Fliesler, S. J.; Cooper, M. J.; Naash, M. I. *PLOS ONE* **2009**, *4*, e5290.

(196) Han, Z.; Conley, S. M.; Makkia, R.; Guo, J.; Cooper, M. J.; Naash, M. I. *PLOS ONE* **2012**, *7*, e52189.

(197) Zulliger, R.; Watson, J. N.; Al-Ubaidi, M. R.; Padegimas, L.; Sesenoglu-Laird, O.; Cooper, M. J.; Naash, M. I. In *Retinal Degenerative Diseases*, ed. by Ash, J. D.; Anderson, R. E.; LaVail, M. M.; Bowes Rickman, C.; Hollyfield, J. G.; Grimm, C., Springer International Publishing: Cham, 2018, pp 109–115.

(198) Fink, T. L.; Klepcyk, P. J.; Oette, S. M.; Gedeon, C. R.; Hyatt, S. L.; Kowalczyk, T. H.; Moen, R. C.; Cooper, M. J. *Gene Therapy* **2006**, *13*, 1048–1051.

(199) Kim, A. J.; Boylan, N. J.; Suk, J. S.; Lai, S. K.; Hanes, J. *Journal of Controlled Release* **2012**, *158*, 102–107.

(200) Feynman, R. P. *Engineering and Science* **1960**, *23*, 22–36.